

INVESTIGATION OF ELECTROMAGNETIC
WAVE PROPAGATION IN DOUBLE NEGATIVE
MATERIALS

SAFFET GÖKÇEN ŞEN

JULY 2008

INVESTIGATION OF ELECTROMAGNETIC WAVE PROPAGATION IN
DOUBLE NEGATIVE MATERIALS

A THESIS SUBMITTED TO
THE GRADUATE SCHOOL OF NATURAL AND APPLIED SCIENCES
OF
MIDDLE EAST TECHNICAL UNIVERSITY

BY

SAFFET GÖKÇEN ŞEN

IN PARTIAL FULFILLMENT OF THE REQUIREMENTS
FOR
THE DEGREE OF DOCTOR OF PHILOSOPHY
IN
ELECTRICAL ENGINEERING

JULY 2008

Approval of the thesis:

**INVESTIGATION OF ELECTROMAGNETIC WAVE PROPAGATION
IN DOUBLE NEGATIVE MATERIALS**

submitted by **SAFFET GÖKÇEN ŞEN** in partial fulfillment of the requirements for the degree of **Doctor of Philosophy in Electrical and Electronics Engineering Department, Middle East Technical University** by,

Prof. Dr. Canan Özgen
Dean, Graduate School of **Natural and Applied Sciences** _____

Prof. Dr. İsmet Erkmek
Head of Department, **Electr. and Electronics Eng.** _____

Prof. Dr. Mustafa Kuzuoğlu
Supervisor, **Electr. and Electronics Eng. Dept., METU** _____

Examining Committee Members:

Prof. Dr. Gönül Turhan Sayan
Electr. and Electronics Eng. Dept., METU _____

Prof. Dr. Mustafa Kuzuoğlu
Electr. and Electronics Eng. Dept., METU _____

Prof. Dr. Gülbin Dural
Electr. and Electronics Eng. Dept., METU _____

Assoc. Prof. Dr. Özlem Aydın Çivi
Electr. and Electronics Eng. Dept., METU _____

Assoc. Prof. Dr. Vakur B. Ertürk
Electr. and Electronics Eng. Dept., Bilkent Uni. _____

Date: 25.07.2008

I hereby declare that all information in this document has been obtained and presented in accordance with academic rules and ethical conduct. I also declare that, as required by these rules and conduct, I have fully cited and referenced all material and results that are not original to this work.

Name, Last Name: Saffet Gökçen Şen

Signature:

ABSTRACT

INVESTIGATION OF ELECTROMAGNETIC WAVE PROPAGATION IN DOUBLE NEGATIVE MATERIALS

Şen, Saffet Gökçen

Ph.D., Department of Electrical and Electronics Engineering

Supervisor: Prof. Dr. Mustafa Kuzuoğlu

July 2008, 138 pages

This thesis analyzes some aspects of electromagnetic wave propagation in double negative materials. Double negative materials have negative refractive indices. They are backward-wave materials. Plane waves undergo negative refraction at interfaces between double positive and double negative media. Causality principle implies these properties. High frequency plane wave scattering from a double negative infinitely long cylinder has been analyzed by using modified Watson transform, geometrical optics and Mie series. Mie series results and the modified Watson transform results have been found to be in good agreement. Hence, the physical mechanism of the scattering has been revealed.

Keywords: Double Negative Material, Negative Refraction, Causality, Modified Watson Transform, Geometrical Optics

ÖZ

ÇİFT NEGATİF MATERYALLERDE ELEKTROMANYETİK DALGALARIN YAYILIMININ İNCELENMESİ

Şen, Saffet Gökçen

Doktora, Elektrik ve Elektronik Mühendisliği Bölümü

Tez Yöneticisi: Prof.Dr.Mustafa Kuzuoğlu

Temmuz 2008, 138 sayfa

Bu tez, elektromanyetik dalgaların çift negative materyallerdeki yayılımının bazı kısımlarını analiz eder. Çift negatif materyaller negatif kırılma indisine sahiptirler. Backward-wave materyallerdir. Düzlemsel dalgalar, çift pozitif ve çift negatif ortamların arasındaki arayüzlerde negatif kırılmaya uğrarlar. Causality prensibi bu özellikleri gerektirir. Modifiye edilmiş Watson dönüşümü, geometrik optik ve Mie serisi kullanılarak, çift negatif sonsuz uzunluktaki silindirden yüksek frekans düzlemsel dalga saçılımı analiz edildi. Mie serisi sonuçları ve modifiye edilmiş Watson dönüşümü sonuçlarının iyi uym içinde oldukları bulundu. Böylece, saçılmanın fiziksel mekanizması ortaya çıkarıldı.

Anahtar kelimeler: Çift Negatif Materyal, Negatif Kırılma, Causality, Modifiye Edilmiş Watson Dönüşümü, Geometrik Optik

To My Family

ACKNOWLEDGMENTS

I wish to express my deepest gratitude to my supervisor Prof. Dr. Mustafa Kuzuođlu for his guidance, advice, criticism, encouragements and insight throughout the research.

I would like to thank Prof. Dr. Gönül Turhan Sayan and Assoc. Prof. Dr. Vakur B. Ertürk for their suggestions and comments during dissertation committees.

I would also like to thank Prof. Dr. Gülbin Dural and Assoc. Prof. Dr. Özlem Aydın Çivi for their suggestions and comments during the dissertation defense meeting.

TABLE OF CONTENTS

ABSTRACT.....	iv
ÖZ.....	v
DEDICATION.....	vi
ACKNOWLEDGMENTS.....	vii
TABLE OF CONTENTS.....	viii
CHAPTER	
1. INTRODUCTION.....	1
2. BASIC PROPERTIES OF DOUBLE NEGATIVE METAMATERIALS.....	8
2.1 The Negative Refractive Index.....	8
2.2 The Backward Wave Property.....	10
2.3 The Negative Refraction at a Planar Interface	12
3. TIME DOMAIN ANALYSIS OF RF PULSE PROPAGATION IN A DOUBLE NEGATIVE METAMATERIAL.....	16
3.1 The Modeling of the DNG Medium.....	16
3.2 The Formulation of the RF Pulse.....	27
3.3 The Formulation of the Propagation of the RF Pulse.....	32

4. HIGH FREQUENCY PLANE WAVE SCATTERING BY AN INFINITELY LONG DOUBLE NEGATIVE CYLINDER.....	40
4.1 The problem Description.....	40
4.2 Mie Series Solution.....	41
4.3 The Modified Watson Transform.....	47
4.4 The Debye Expansion.....	51
4.5 The First Term of the Debye Expansion....	58
4.6 The Second Term of the Debye Expansion	75
5. NUMERICAL RESULTS.....	93
5.1 The Geometrical Shadow Region of the Double Positive Cylinder Corresponding to the First Term of the Debye Series.....	93
5.2 The Geometrically Lit Region of the Double Positive Cylinder Corresponding to the First Term of the Debye Series.....	98
5.3 The Geometrical Shadow Region of the Double Positive Cylinder Corresponding to The Second Term of the Debye Series....	103
5.4 The Geometrically Lit Region of the Double Positive Cylinder Corresponding to the Second Term of the Debye Series.....	109
5.5 The Geometrical Shadow Region of the Double Negative Cylinder Corresponding to the First Term of the Debye Series.....	114
5.6 The Geometrically Lit Region of the Double Negative Cylinder Corresponding to the First Term of the Debye Series.....	119

5.7 The Geometrically Lit Region of the Double Negative Cylinder Corresponding to The Second Term of the Debye Series....	123
5.8 The Geometrical Shadow Region of the Double Negative Cylinder Corresponding to The Second Term of the Debye Series....	128
6. CONCLUSION.....	133
REFERENCES.....	135
CURRICULUM VITAE.....	138

CHAPTER 1

INTRODUCTION

In 1968, Veselago suggested a theoretical electromagnetic material in his article [1] and examined the properties of this material which has a negative permittivity and a negative permeability. The practical implementation of this theoretical suggestion is double negative or left-handed metamaterials. The reason for the name double negative is the fact that both of the permittivity and the permeability are negative. As shown in the article of Veselago, the coordinate system formed by the electric field intensity vector, the magnetic field intensity vector and the propagation vector of a monochromatic plane wave is a left-handed coordinate system. Hence, another naming convention for double negative metamaterials is the left-handed metamaterials. Veselago presents the unusual properties of the materials as having a negative refractive index, the opposite directions of the phase velocity vector and the power propagation vector, the reverse Doppler effect, and the negative refraction at an interface between a right-handed medium and a left-handed medium. In addition, a left-handed material must be dispersive.

In the studies made for the realization of the double negative metamaterials, the articles [2] and [3] are often referred. In [2], several structures including the split ring resonator (SRR) are proposed to build a material having an effective permeability under microwave radiation. The dependence of the effective permeability on the geometrical parameters of the structures and frequency is given. In [3], a method for forming a plasmon effect in the GHz frequency ranges by lowering the effective plasma frequency is given. Using a structure made of thin wires of a particular separation, an effective permittivity and an effective plasma frequency are obtained at GHz ranges for the structure. [2]

and [3] are the fundamental articles for the SRR and thin-wire realizations of left-handed metamaterials.

In [4], the construction of a left-handed metamaterial and the numerical and the experimental verification of the left-handedness are reported. The building blocks of the left-handed structures are split ring resonators (SRR) and thin wires. In [5], a slab of a left-handed metamaterial is reported to focus all Fourier components of a 2D image. The realization of such super-lenses is reported to be possible in the microwave range. Simulations of a version of the lens operating at the frequency of visible light in the form of a slab of silver are reported. The first experimental verification of the negative refraction is claimed in [6]. A prism made of SRRs and thin wires are claimed to refract the incident beam negatively in the microwave range. However, the negative refraction experiments are claimed to be wrong by [7] and [8]. In [7], it is indicated that experiments on metallic left-handed materials to verify the existence of the negative refraction are questionable. At the experiments' microwave frequencies, the material behaves as a metal and the waves under observation become inhomogeneous. In [8], it is indicated that the negative refraction of the phase is possible but the negative refraction of the signal is impossible due to causality requirements and the finite signal speed. The positive group refraction and the negative phase refraction cause the formation of an inhomogeneous wave and this distortion prevents the healthy information transfer across two media. It is claimed in [8] that negative refraction is impossible for all kinds of waves. [9] claims that the analysis in [5] has some errors in it and the negative refraction by a left-handed metamaterial slab is impossible. [10] examines left-handed metamaterials especially from the aspect of causality. In left-handed metamaterials, the causality principle implies a negative refractive index. Narrowband and wideband pulses are propagated in a dispersive left-handed medium using finite difference time domain (FDTD) method in order to exhibit the negative phase velocity and the agreement between the negative phase velocity and the causality principle. It is shown that

the perfect lens made of a slab of a left-handed metamaterial is impossible for realistic metamaterials. [11] also reports FDTD simulation results to show that the causality principle requires the left-handed material to be dispersive. It is also shown that the wave propagation properties in a left-handed medium, negative refractive index and the causality are all in agreement.

After a brief chronological survey of the literature on left-handed metamaterials, the articles which are referred the most in the literature on left-handed metamaterials are reviewed.

The first realization of metamaterials was first made by using SRRs and thin wires. Another popular way of realization was given almost at the same time in [12], [13] and [14]. In the article [15] about this realization, the positions of L and C are simply interchanged in the L-C distributed network representation of homogeneous dielectrics to obtain simultaneously negative material parameters. The circuit and full-wave field simulations illustrating negative refraction and focusing are presented. The first experimental verification of near-field focusing of an incident cylindrical wave is demonstrated. In [16], the experimental data, numerical simulations and analytical transfer-matrix calculations for a two-dimensionally isotropic left-handed metamaterial at X-band microwave frequencies show that it is appropriate to consider LHM as a homogeneous material with frequency dispersive material parameters. Hence, the concept of LHM is simplified. In [17], the transmission at a boundary between a right-handed medium and a left-handed medium is studied. Two types of signals are used. One of the signals is a Gaussian pulse and the other is made of two discrete spectra. For both of the signals, negative refraction is observed as a result of the calculations. In [18], the basic electromagnetic properties of left-handed metamaterials are reviewed. These properties are verified by finite-element method full-wave analysis using rectangular waveguide structures loaded by an LHM. The negative phase velocity, positive intrinsic impedance and the negative angle of refraction at an interface with a right-handed medium are experimentally verified.

There are some studies on the scattering properties of cylinders and spheres made of left-handed metamaterials. The extinction spectra of a sphere with negative permittivity and permeability are examined in [19]. It is determined that when both of the permittivity and the permeability of the dispersive sphere become negative, radiation can penetrate into the sphere. However, if either of the permittivity or the permeability (but not both) is negative, then the radiation cannot penetrate into the sphere. The scattering properties of a cylinder made of a left-handed material are subject of the article [20]. The scattering width of the infinite-length cylinder is calculated in terms of the Mie scattering coefficients. The maximum values of the scattering width are obtained at the resonances of the Mie scattering coefficients. These resonances occur in the frequency region where the cylinder behaves as a left-handed material. The electric field intensity distributions inside an infinite-length cylinder or a sphere are calculated for both right-handed and left-handed cases under the illumination of a plane wave in [21]. For the left-handed case and high-frequency operation, it is shown that the intensity focuses on the axis through the center closer to the side of the illumination. This observation is in agreement with the negative refraction of the incident plane wave.

There are also practical applications of left-handed metamaterials. In [22], an electrically small antenna is covered with a double negative shell to increase the power radiated and to decrease the reactance of the antenna. The DNG shell is used as a matching network to the free space. This antenna configuration is theoretically studied assuming a non-dispersive DNG shell. A left-handed metamaterial layer is inserted between two single-mode waveguides in [23]. By the help of this LHM layer, the coupling length of the single-mode waveguides is significantly reduced. The reflection loss is reduced by tapering the ends of the LHM layer. Another advantage of this new directional coupler is omitting the need for bent waveguides.

The scattering of a high frequency plane wave from an infinitely long double positive and an infinitely long double negative cylinder is analyzed using the

Debye expansion with the Modified Watson transformation in this thesis work. The Debye expansion was first introduced by Debye in 1908 in his work on a dielectric cylinder in [24]. The Debye expansion brings a physical insight into the Mie series expansion of the scattered field. At high frequency, the incident plane wave can be considered as a collection of incident rays. If the incident rays are traced, then it can be observed that the incident rays are first reflected by the scatterer, and then the incident rays are transmitted into the scatterer. The transmitted ray is partly reflected by the inside surface of the scatterer and is transmitted to the outside of the scatterer. The ray reflected from inside of the scatterer continues with this infinite chain of reflections and transmissions. When the Debye expansion is applied to the Mie coefficients, this series of reflection and transmissions is revealed. In [25], the high frequency scattering by a dielectric cylinder or a sphere is calculated in terms of the radar cross section applying the Debye expansion to the Mie series coefficients and applying the Watson transformation to each term of the Debye expansion. This thesis work is similar to another work that is performed in [26]. The high-frequency scattering due to a dielectric cylinder is calculated by applying the Debye expansion to the Mie series coefficients and applying the Watson transformation to the Debye expansion terms in [26]. This thesis work takes [27] and [28] as the starting points. In [27], the high-frequency scalar scattering from an impenetrable sphere illuminated by a plane wave is studied using the Modified Watson transformation. In [28], the high-frequency scalar scattering from a penetrable sphere illuminated by a plane wave is analyzed using the Debye expansion and the Modified Watson transformation. The method in [28] considers the scattering as a series of surface interactions between the sphere and the rays of the incident high frequency plane wave. Each surface interaction is interpreted as a scattering problem similar to the one in [27].

The double negative metamaterials have some new properties when they are compared to the materials with positive relative permeabilities and positive relative permittivities. Some of these properties are the negative refractive

index property, the backward wave property and the negative refraction property. In the second chapter, these properties are introduced and they are proven to exist. It is also shown that the causality principle implies the refractive index of a double negative material to be negative. In the proof of this fact, the idea has been taken from the reference [10]. However, the proof is a little different from the reference [10]. The third chapter is devoted to the time domain analysis of the propagation of an rf pulse in a double negative medium. The analysis in this chapter uses the time domain pulse model and the double negative medium model given in the reference [10]. The way of exhibiting the backward wave property of the medium is taken from the reference [11]. However, the method of making the pulse propagate in the medium is different from the method (FDTD) in the references [10] and [11]. The backward wave property of the double negative medium is shown to agree with the causality principle using the simulation results. The fourth chapter deals with the high frequency analysis of the plane wave scattering from a double positive infinitely long cylinder and from a double negative infinitely long cylinder. The analysis using the modified Watson transform and the Debye series expansion given in the reference [28] for the scalar scattering from a penetrable sphere is adapted to the electromagnetic scattering from the infinitely long cylinder. The physical interpretation given in [28] for the Debye series expansion is adapted to the scattering problem. The first and the second terms of the Debye series are examined. The field formation in the geometrical shadow and the geometrically lit regions of the first and second terms are explained by giving the physical insight into the scattering. In the fifth chapter, the theoretical results are proven to be true for both of the double positive and the double negative infinitely long cylinder. The proof of the theoretical results is made by comparing the Debye series terms with the corresponding field integrals in the corresponding geometrical shadow and the geometrically lit regions. The computations are made using Mathematica. In the sixth chapter,

the conclusions derived from the work and the possible future studies are presented.

CHAPTER 2

BASIC PROPERTIES OF DOUBLE NEGATIVE METAMATERIALS

A double negative medium (DNG) is a medium with a negative permittivity denoted by ε and a negative permeability denoted by μ . A double negative medium has several important properties. These are having a negative refractive index, the backward wave property, the negative refraction at a planar interface. In this chapter, these basic properties of double negative metamaterials are presented and they are shown to exist.

2.1 The Negative Refractive Index

The following analysis uses the idea presented in [10] for the proof of the negative refractive index property. Throughout the analysis, the time harmonic dependence of $e^{j\omega t}$ is assumed. Another assumption is that the double negative medium is temporally dispersive and passive. Let the complex permeability and the complex permittivity be given as follows:

$$\varepsilon(\omega) = \varepsilon_R(\omega) - j\varepsilon_I(\omega) \tag{1}$$

$$\mu(\omega) = \mu_R(\omega) - j\mu_I(\omega) \tag{2}$$

The causality condition for the DNG medium, i.e. the medium does not give any response before a disturbance is applied, is satisfied if $\varepsilon(\omega)$ and $\mu(\omega)$ are analytic in the lower half of the complex ω -plane. The following results can be shown to be true for a temporally dispersive medium:

$$\lim_{|\omega| \rightarrow \infty} |\omega[\varepsilon(\omega) - \varepsilon_0]| = 0 \text{ for } \text{Im}\{\omega\} < 0 \tag{3}$$

$$\lim_{|\omega| \rightarrow \infty} |\omega[\mu(\omega) - \mu_0]| = 0 \text{ for } \text{Im}\{\omega\} < 0 \quad (4)$$

Since the medium is passive, the imaginary parts of the permeability and the permittivity are negative. Due to the medium's being double negative, the real parts of the permeability and the permittivity are also negative. Hence, the permittivity and the permeability are in the third quadrant of the complex plane and have the following mathematical forms:

$$\varepsilon(\omega) = |\varepsilon(\omega)| \exp[j\angle\varepsilon(\omega)] \text{ for } \pi < \angle\varepsilon(\omega) < \frac{3\pi}{2} \quad (5)$$

$$\mu(\omega) = |\mu(\omega)| \exp[j\angle\mu(\omega)] \text{ for } \pi < \angle\mu(\omega) < \frac{3\pi}{2} \quad (6)$$

The square roots of the permittivity and the permeability functions are given by

$$\sqrt{\varepsilon(\omega)} = |\varepsilon(\omega)|^{\frac{1}{2}} \exp\left[j\frac{\angle\varepsilon(\omega)}{2} + jm\pi\right] \text{ for } m = 0 \text{ and } m = 1 \quad (7)$$

$$\sqrt{\mu(\omega)} = |\mu(\omega)|^{\frac{1}{2}} \exp\left[j\frac{\angle\mu(\omega)}{2} + jq\pi\right] \text{ for } q = 0 \text{ and } q = 1 \quad (8)$$

Using the information given in the equation (3), it is written that

$$\lim_{|\omega| \rightarrow \infty} \sqrt{\varepsilon(\omega)} = \sqrt{\varepsilon_0} \quad (9)$$

For the equation (9) to hold, m in the equation (7) must be chosen as 1. If m is chosen as 0, then

$$\lim_{|\omega| \rightarrow \infty} \sqrt{\varepsilon(\omega)} = -\sqrt{\varepsilon_0} \quad (10)$$

which is in contradiction with (3) and (9). Hence, the value for m in the computation of the square root of the permittivity function is determined from the calculation of

$$\lim_{|\omega| \rightarrow \infty} \sqrt{\varepsilon(\omega)}$$

Since $\sqrt{\varepsilon(\omega)}$ is a factor determining the refractive index of a real life material, it is required to be an analytical function of ω . The analyticity requires m to be the same over the whole range of ω . Using the same reasoning, a similar result is found for $\mu(\omega)$. The value of q in (8) must be equal to 1.

Then, the refractive index n of a DNG material is calculated as

$$n(\omega) = \sqrt{\varepsilon(\omega)}\sqrt{\mu(\omega)} \exp \left\{ j \left[\frac{\varkappa\varepsilon(\omega) + \varkappa\mu(\omega)}{2} \right] \right\} \quad (11)$$

where

$$\pi < \varkappa n(\omega) = \frac{\varkappa\varepsilon(\omega) + \varkappa\mu(\omega)}{2} < \frac{3\pi}{2} \quad (12)$$

For the time harmonic dependence of $e^{j\omega t}$, $n(\omega)$ has a negative real part and a negative imaginary part. If the time harmonic dependence were $e^{-j\omega t}$, $n(\omega)$ would have a negative real part and a positive imaginary part.

2.2 The Backward Wave Property

One of the important properties of a DNG material is the backward wave property. A DNG material is a backward wave material because the direction of the phase velocity of the wave and the direction of the power flow are opposite to each other. Let the material be double negative, passive and temporally dispersive.

It is assumed an x-polarized plane wave propagates along z-axis in the material. The time harmonic dependence is $e^{j\omega t}$. Then, the following equations can be written as

$$\vec{E} = \hat{a}_x e^{-jkz} \quad (13)$$

$$\vec{H} = \hat{a}_y \left(\frac{k}{\omega\mu} \right) e^{-jkz} \quad (14)$$

where

$$k = k_0 n \quad (15)$$

$$n = \sqrt{\varepsilon(\omega)} \sqrt{\mu(\omega)} \quad (16)$$

$$\varepsilon(\omega) = |\varepsilon(\omega)| \exp[j\alpha\varepsilon(\omega)] \text{ for } \pi < \alpha\varepsilon(\omega) < \frac{3\pi}{2} \quad (17)$$

$$\mu(\omega) = |\mu(\omega)| \exp[j\alpha\mu(\omega)] \text{ for } \pi < \alpha\mu(\omega) < \frac{3\pi}{2} \quad (18)$$

The complex Poynting vector of the electromagnetic field can be written as

$$\vec{P} = \vec{E} \times \vec{H}^* = \hat{a}_z \frac{k_0 [n(\omega)]^*}{\omega |\mu(\omega)| e^{-j\alpha\mu(\omega)}} \exp\{2k_0 \text{Im}[n(\omega)]z\} \quad (19)$$

The average Poynting vector corresponding to the complex Poynting vector is given by

$$\vec{P}_{av} = \frac{1}{2} \text{Re}\{\vec{P}\} = \hat{a}_z \frac{1}{2} \left(\frac{|\varepsilon|}{|\mu|} \right)^{\frac{1}{2}} \left(\frac{k_0}{\omega} \right) e^{2k_0 \text{Im}[n(\omega)]z} \text{Re} \left\{ e^{j \left[\frac{\alpha\varepsilon(\omega)}{2} - \frac{\alpha\mu(\omega)}{2} \right]} \right\} \quad (20)$$

where

$$-\frac{\pi}{4} < \left[\frac{\alpha\varepsilon(\omega)}{2} - \frac{\alpha\mu(\omega)}{2} \right] < \frac{\pi}{4}$$

The direction of the average Poynting vector gives the direction of the power flow and the direction of the real part of the wave number vector gives the

direction of the phase velocity vector. Hence, the inner product of \vec{P}_{av} with $Re\{\vec{k}\}$ indicates if there is the backward wave property as indicated in [30].

$$\begin{aligned} & \vec{P}_{av} \cdot Re\{\vec{k}\} \\ & = \\ & \underbrace{\frac{1}{2} |\varepsilon(\omega)| \left(\frac{k_0^2}{\omega}\right) e^{2k_0 Im[n(\omega)]z}}_{+} \underbrace{Re\left\{e^{j\left[\frac{\Re\varepsilon(\omega)}{2} - \frac{\Re\mu(\omega)}{2}\right]}\right\}}_{+} \underbrace{Re\left\{e^{j\left[\frac{\Re\varepsilon(\omega)}{2} + \frac{\Re\mu(\omega)}{2}\right]}\right\}}_{-} \end{aligned} \quad (21)$$

Hence,

$$\vec{P}_{av} \cdot Re\{\vec{k}\} < 0 \quad (22)$$

which means that there is the backward wave property. A DNG material is a backward wave material.

2.3 The Negative Refraction at a Planar Interface

Assume that the x-z plane is divided into two halves by a plane interface at $z = 0$. A plane wave propagating in the free space ($z < 0$) is obliquely incident on the interface with a perpendicular polarization. To the right of the plane interface ($z > 0$), there is a DNG medium. The problem geometry is given in the Figure 1.

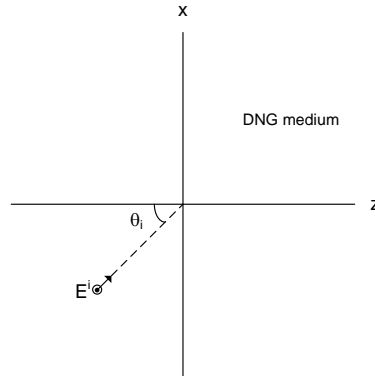


Figure 1 The problem geometry

Using the time harmonic dependence of $e^{j\omega t}$, the incident electromagnetic field is given by the following:

$$\vec{E}^i = \hat{a}_y e^{-jk_0 \hat{a}_{n_i} \cdot \vec{r}} \quad (23)$$

$$\vec{H}^i = \frac{1}{Z_0} (-\hat{a}_x \cos \theta_i + \hat{a}_z \sin \theta_i) e^{-jk_0 \hat{a}_{n_i} \cdot \vec{r}} \quad (24)$$

where

$$\hat{a}_{n_i} = \hat{a}_x \sin \theta_i + \hat{a}_z \cos \theta_i \quad (25)$$

is the propagation direction of the incident wave, θ_i is the incidence angle, and Z_0 is the intrinsic impedance of the free space.

The reflected electromagnetic field is written as follows:

$$\vec{E}^r = \hat{a}_y R e^{-jk_0 \hat{a}_{n_r} \cdot \vec{r}} \quad (26)$$

$$\vec{H}^r = \left(\frac{R}{Z_0} \right) (\hat{a}_x \cos \theta_r + \hat{a}_z \sin \theta_r) e^{-jk_0 \hat{a}_{n_r} \cdot \vec{r}} \quad (27)$$

where

$$\begin{aligned} \hat{a}_{n_r} &= \hat{a}_x \sin \theta_r - \hat{a}_z \cos \theta_r \\ R &= \frac{\left(\frac{1}{Z_0} \cos \theta_i - \frac{1}{Z} \cos \theta_t \right)}{\left(\frac{1}{Z_0} \cos \theta_r + \frac{1}{Z} \cos \theta_t \right)} \\ Z &= \sqrt{\frac{|\mu_r|}{|\epsilon_r|}} \end{aligned} \quad (28)$$

\hat{a}_{n_r} is the propagation direction of the reflected wave, θ_r is the reflection angle, θ_t is the refraction angle, R is the reflection coefficient, and Z is the intrinsic

impedance of the DNG medium with relative permittivity ϵ_r and relative permeability μ_r .

The electromagnetic field transmitted to the DNG medium is given by

$$\vec{E}^t = \hat{a}_y T e^{-jn k_0 \hat{a}_{n_t} \cdot \vec{r}} \quad (29)$$

$$\vec{H}^t = \frac{T}{Z} (-\hat{a}_x \cos \theta_t + \hat{a}_z \sin \theta_t) e^{-jn k_0 \hat{a}_{n_t} \cdot \vec{r}} \quad (30)$$

where

$$\begin{aligned} \hat{a}_{n_t} &= \hat{a}_x \sin \theta_t + \hat{a}_z \cos \theta_t \\ T &= 1 + R \end{aligned} \quad (31)$$

\hat{a}_{n_t} is the propagation direction of the transmitted wave, T is the transmission coefficient, n is the refractive index of the DNG medium.

In order to find the reflected and the transmitted waves, the continuity of the tangential components of the total electric field intensities at the interface is satisfied. The continuity requirement is met also for the tangential components of the total magnetic field intensities at the interface. To satisfy the continuity requirement, the phase matching condition must first be written at the interface. The phase matching condition at the interface is as follows:

$$k_0 \sin \theta_i = k_0 \sin \theta_r = -|n| k_0 \sin \theta_t \quad (32)$$

The phase matching condition implies that

$$\theta_i = \theta_r \quad (33)$$

$$\sin \theta_i = -|n| \sin \theta_t \quad (34)$$

Then, the reflection angle is the same as the usual case. However, the refraction angle is the negative of the usual case. This means that the transmitted wave is

negatively refracted. It stays at the same side of the normal as the incident wave. The negative refraction is shown in the Figure 2.

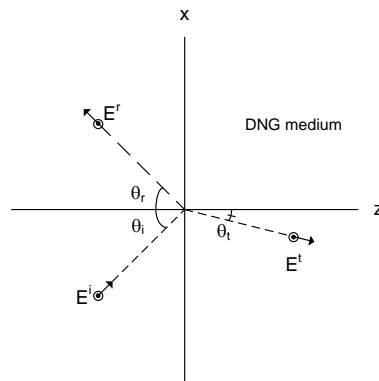


Figure 2 The negative refraction at the plane interface

CHAPTER 3

TIME DOMAIN ANALYSIS OF RF PULSE PROPAGATION IN A DOUBLE NEGATIVE METAMATERIAL

In this chapter, the propagation of an rf pulse in a DNG medium is to be demonstrated in the time domain. The DNG medium is modeled by a Lorentz medium model. The permittivity and the permeability are functions of the angular frequency ω . The observation of the pulse at very close time instants demonstrates the double-negativeness of the medium. On the other hand, the distant time observations exhibits the fact that double-negativeness does not violate the causality principle.

3.1 The Modeling of the DNG Medium

The DNG medium is temporally dispersive with some dielectric loss. The mathematical forms of the permittivity and permeability are described as functions of the angular frequency ω . They are given as follows:

$$\varepsilon(\omega) = \varepsilon_0 \left[1 - \frac{\omega_{pe}^2}{(\omega + j\Gamma_{e1})(\omega + j\Gamma_{e2})} \right] \quad (35)$$

$$\mu(\omega) = \mu_0 \left[1 - \frac{\omega_{pm}^2}{(\omega + j\Gamma_{m1})(\omega + j\Gamma_{m2})} \right] \quad (36)$$

ω_{pe}, ω_{pm} : Angular plasma frequencies

$\Gamma_{e1}, \Gamma_{e2}, \Gamma_{m1}, \Gamma_{m2}$: Negative damping coefficients

The angular plasma frequencies and the negative damping coefficients can be adjusted to obtain a medium of desired properties changing with angular frequency. As an example, the real parts of the relative permeability and the

relative permittivity of a DNG medium becomes -1 at the frequency 30 GHz with the following angular plasma frequencies and the negative damping coefficients:

$$\begin{aligned}\Gamma_{e1} &= -1 \times 10^8 \text{ rad/s} & \Gamma_{m1} &= -1 \times 10^8 \text{ rad/s} \\ \Gamma_{e2} &= -1 \times 10^8 \text{ rad/s} & \Gamma_{m2} &= -1 \times 10^8 \text{ rad/s} \\ \omega_{pe} &= 2.6650 \times 10^{11} \text{ rad/s} & \omega_{pm} &= 2.6650 \times 10^{11} \text{ rad/s}\end{aligned}$$

The values given in the above are taken from [10]. For this medium, the real part of the relative permittivity is shown in the following figures:

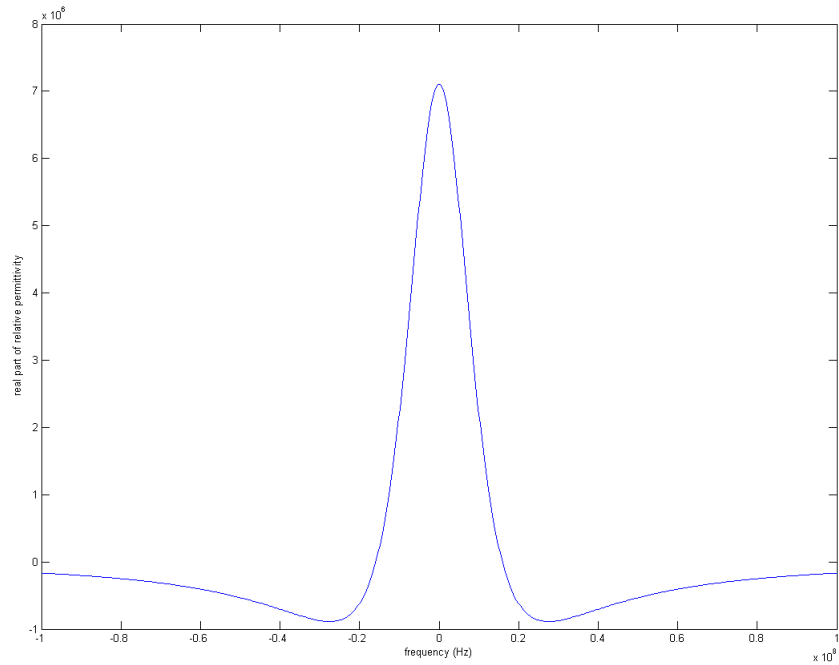


Figure 3 The real part of the relative permittivity. The frequency axis is from -100 MHz to 100 MHz. The maximum value of the real part of the relative permittivity axis is 8×10^6 .

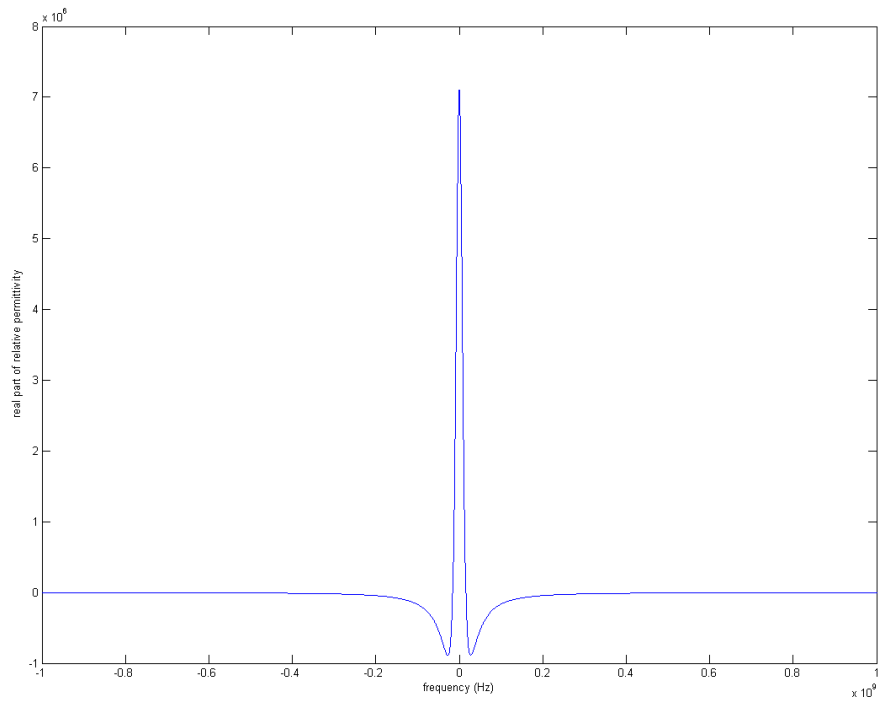


Figure 4 The real part of the relative permittivity. The frequency axis is from -1 GHz to 1 GHz. The maximum value of the real part of the relative permittivity axis is 8×10^6 .

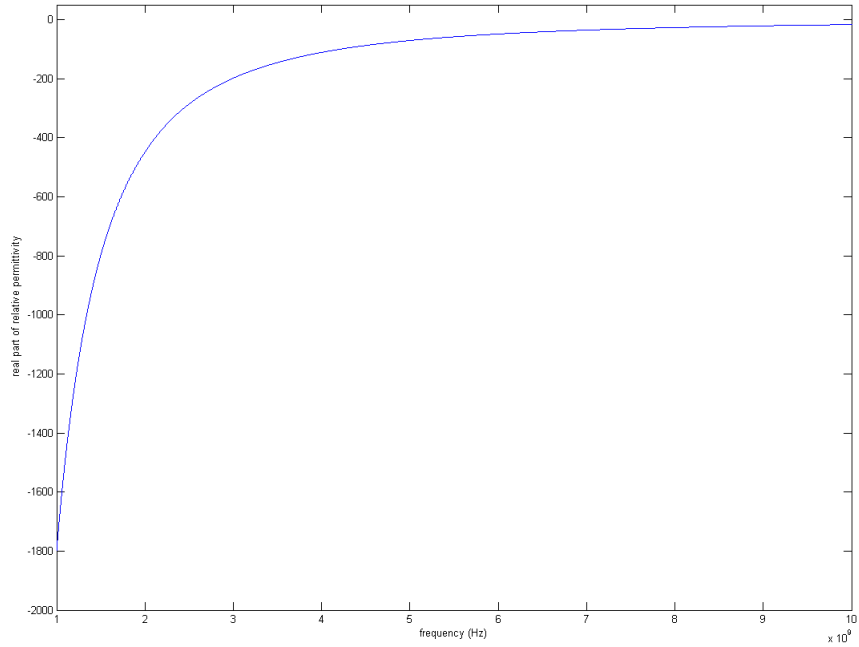


Figure 5 The real part of the relative permittivity. The frequency axis is from 1 GHz to 10 GHz.

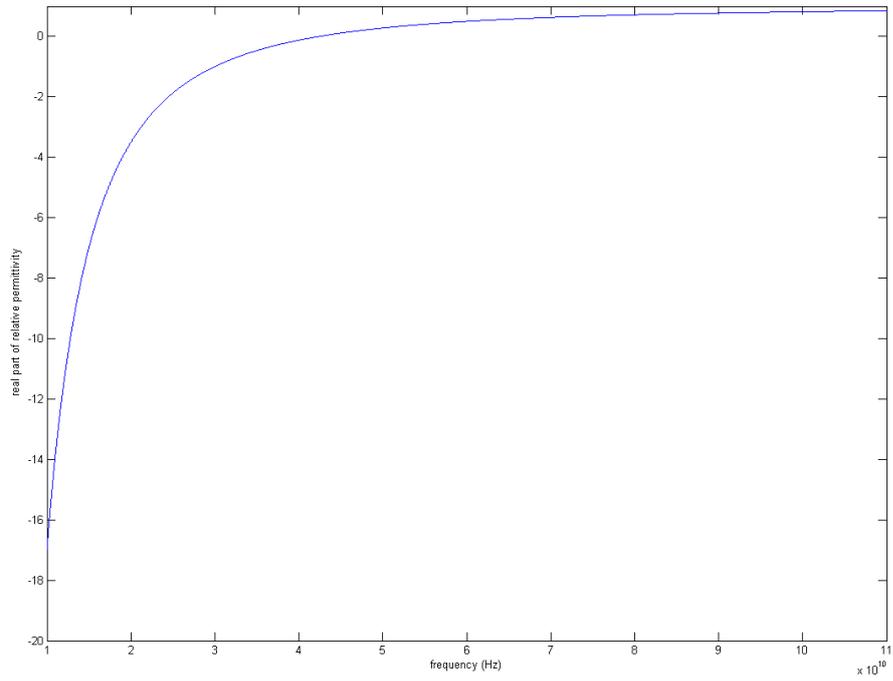


Figure 6 The real part of the relative permittivity. The frequency axis is from 10 GHz to 110 GHz.

The imaginary part of the relative permittivity is shown in the following figures:

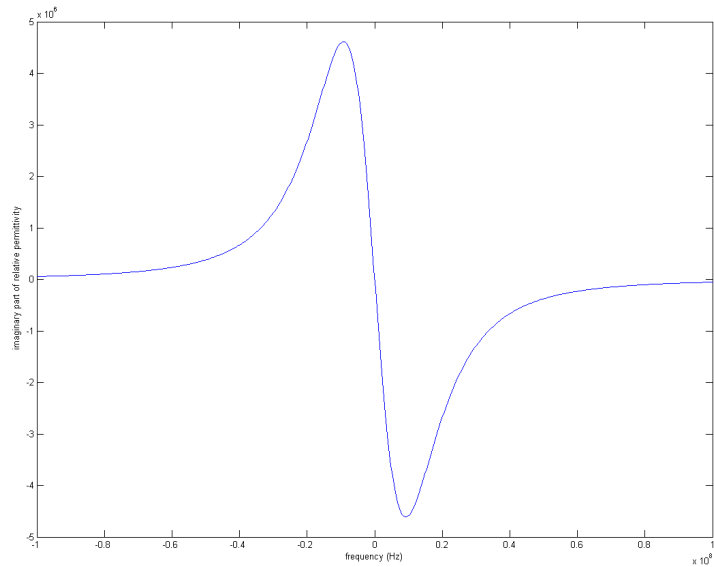


Figure 7 The imaginary part of the relative permittivity. The frequency axis is from -100 MHz to 100 MHz. The maximum value of the imaginary part of the relative permittivity axis is 5×10^6 .

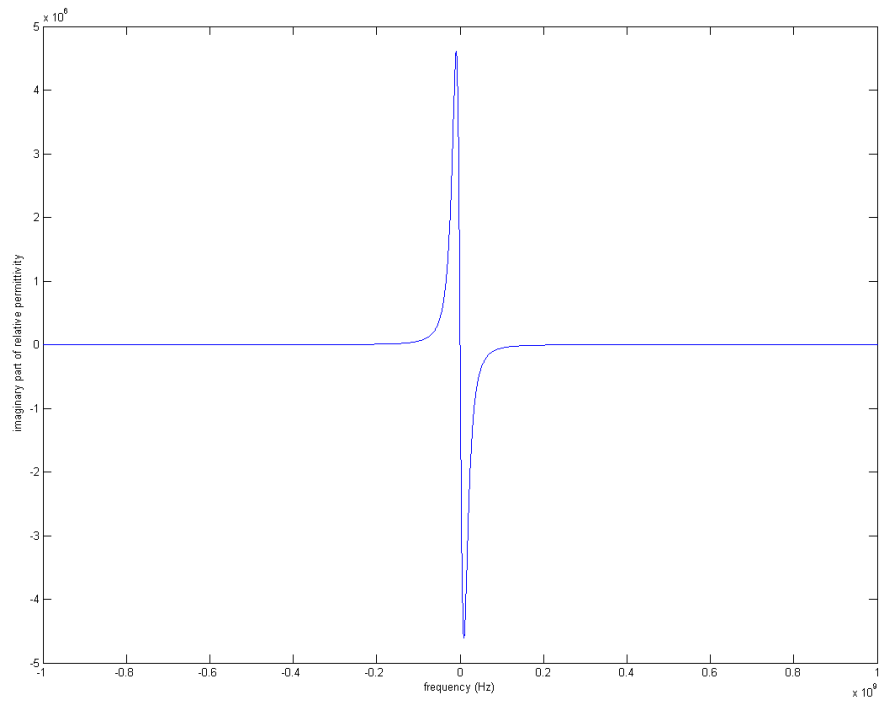


Figure 8 The imaginary part of the relative permittivity. The frequency axis is from -1 GHz to 1 GHz. The maximum value of the imaginary part of the relative permittivity axis is 5×10^6 .

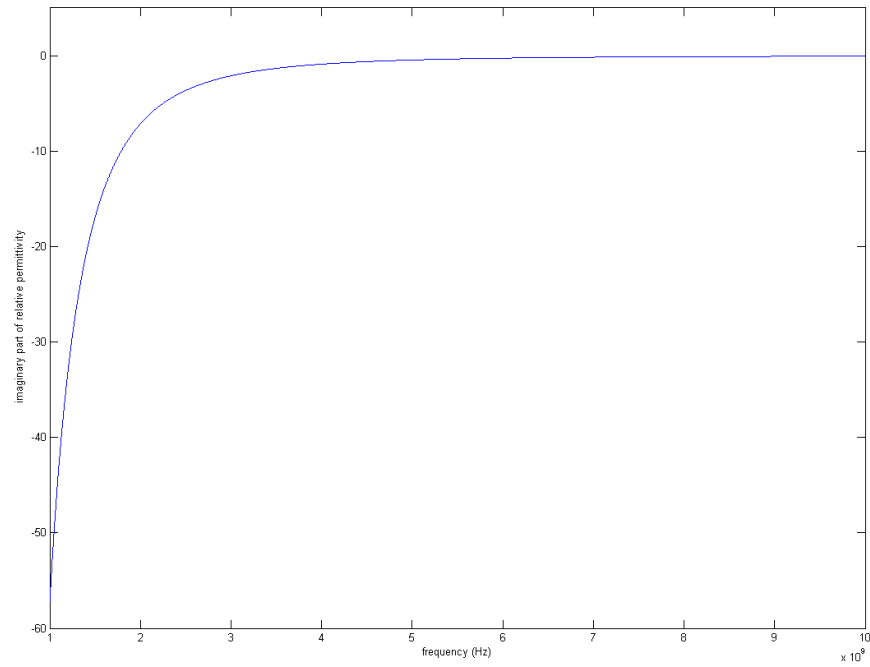


Figure 9 The imaginary part of the relative permittivity. The frequency axis is from 1 GHz to 10 GHz.

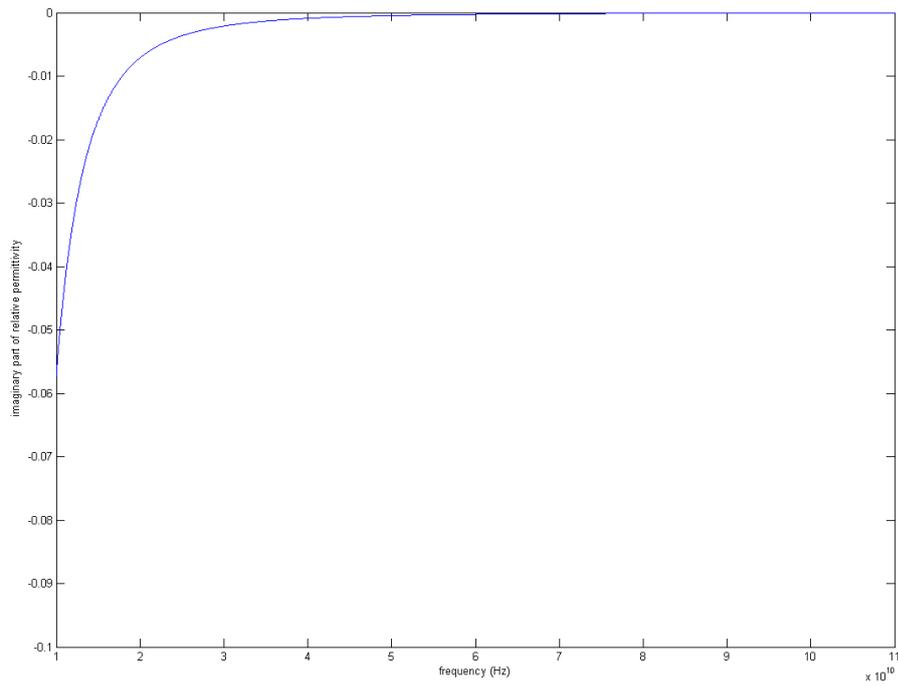


Figure 10 The imaginary part of the relative permittivity. The frequency axis is from 10 GHz to 110 GHz.

The relative permeability of the medium is the same as the relative permittivity of the medium. The refractive index of the medium is shown in the following figures:

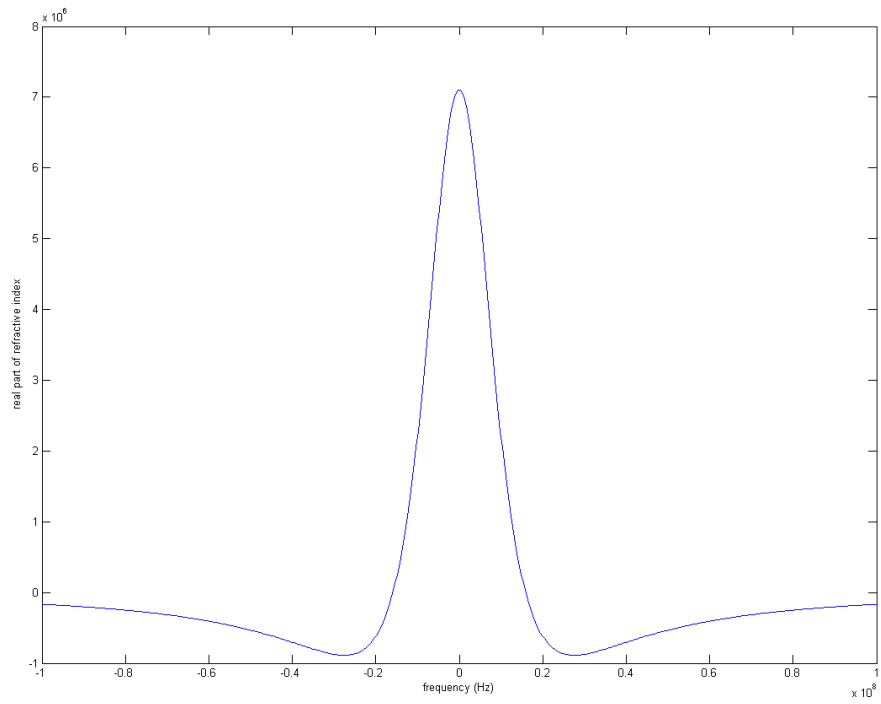


Figure 11 The real part of the refractive index. The frequency axis is from -100 MHz to 100 MHz. The maximum value of the real part of the refractive index axis is 8×10^6 .

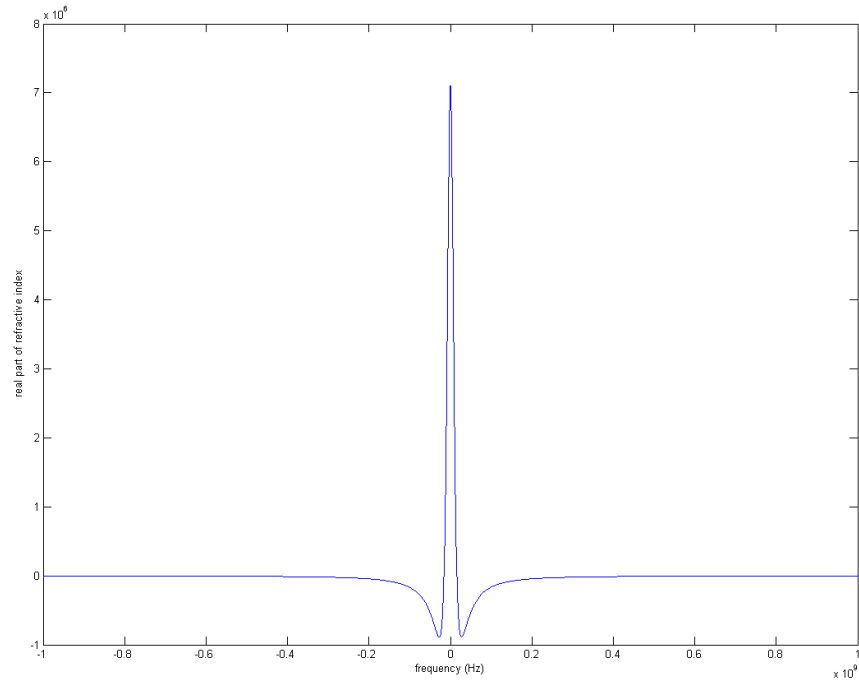


Figure 12 The real part of the refractive index. The frequency axis is from -1 GHz to 1 GHz. The maximum value of the real part of the refractive index axis is 8×10^6 .

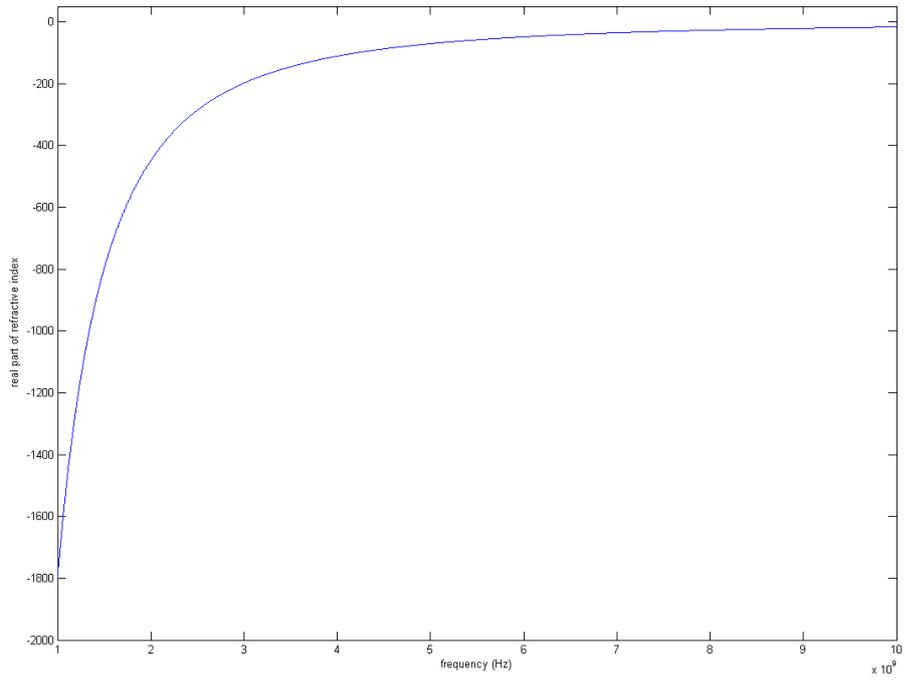


Figure 13 The real part of the refractive index. The frequency axis is from 1 GHz to 10 GHz.

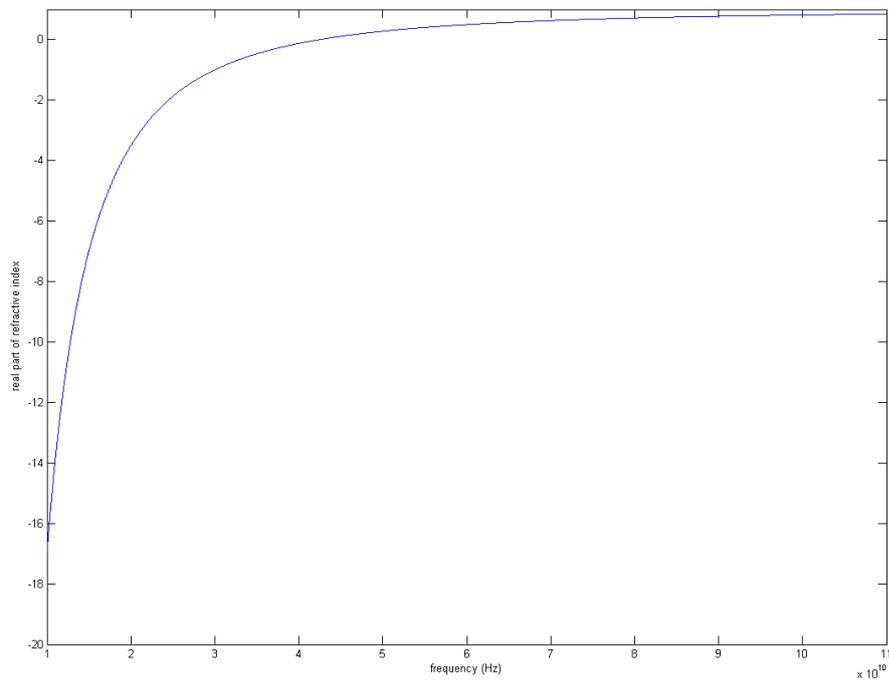


Figure 14 The real part of the refractive index. The frequency axis is from 10 GHz to 110 GHz.

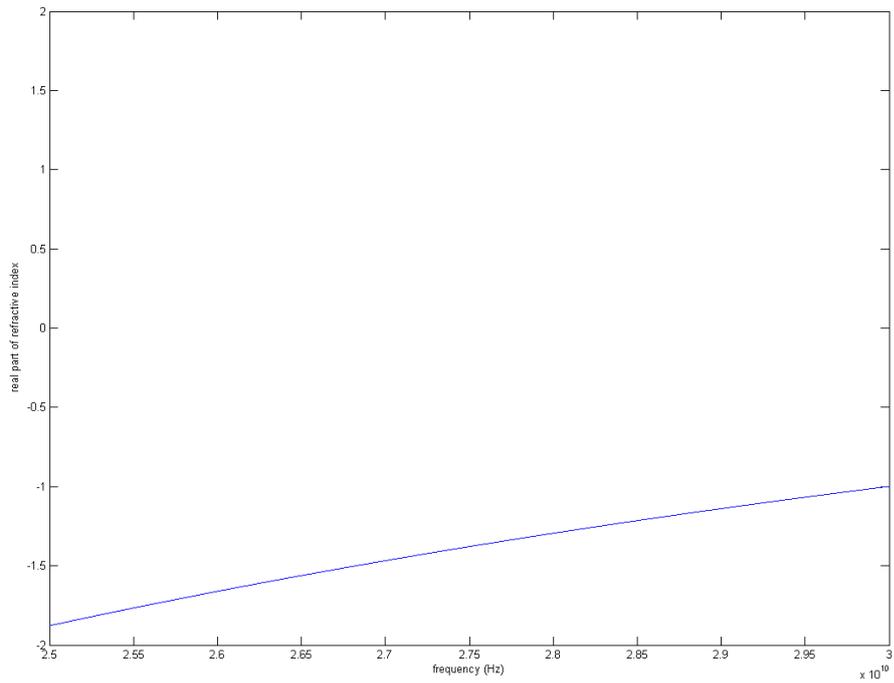


Figure 15 The real part of the refractive index. The frequency axis is from 25 GHz to 30 GHz. The real part becomes -1 at 30 GHz.

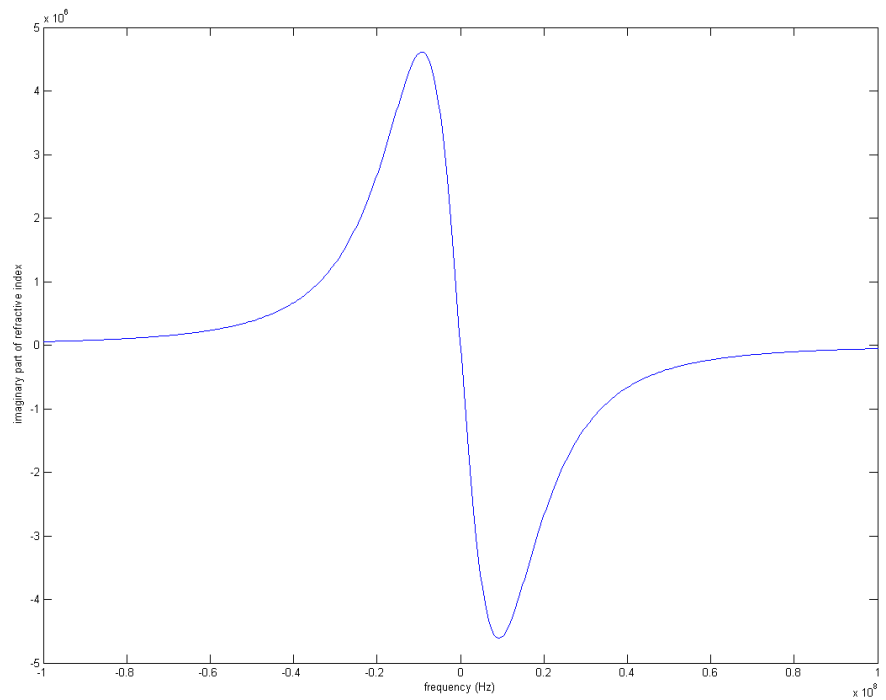


Figure 16 The imaginary part of the refractive index. The frequency axis is from -100 MHz to 100 MHz. The maximum value of the imaginary part of the refractive index axis is 5×10^6 .

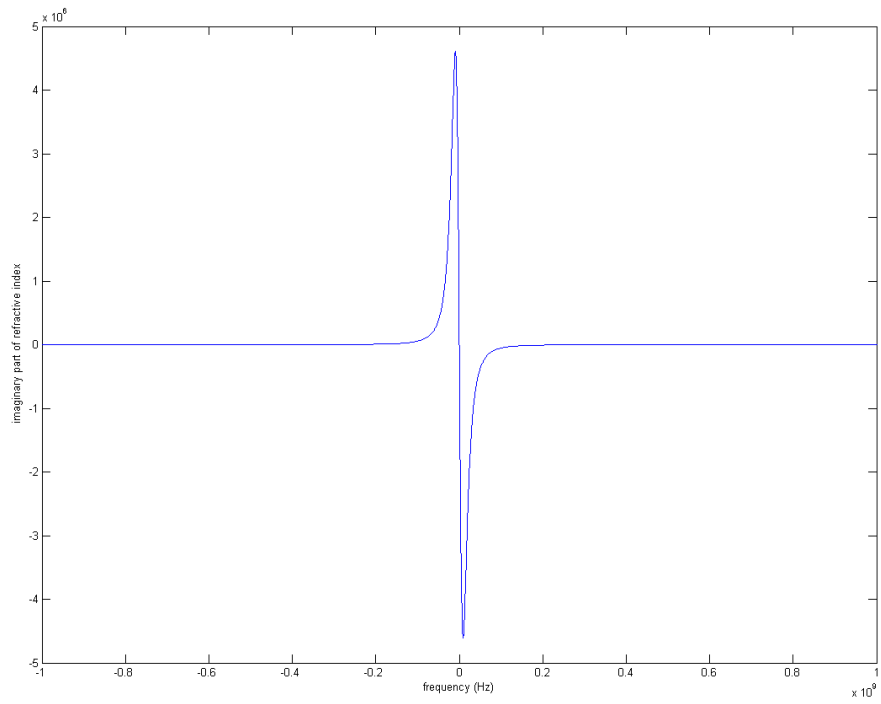


Figure 17 The imaginary part of the refractive index. The frequency axis is from -1 GHz to 1 GHz. The maximum value of the imaginary part of the refractive index axis is 5×10^6 .

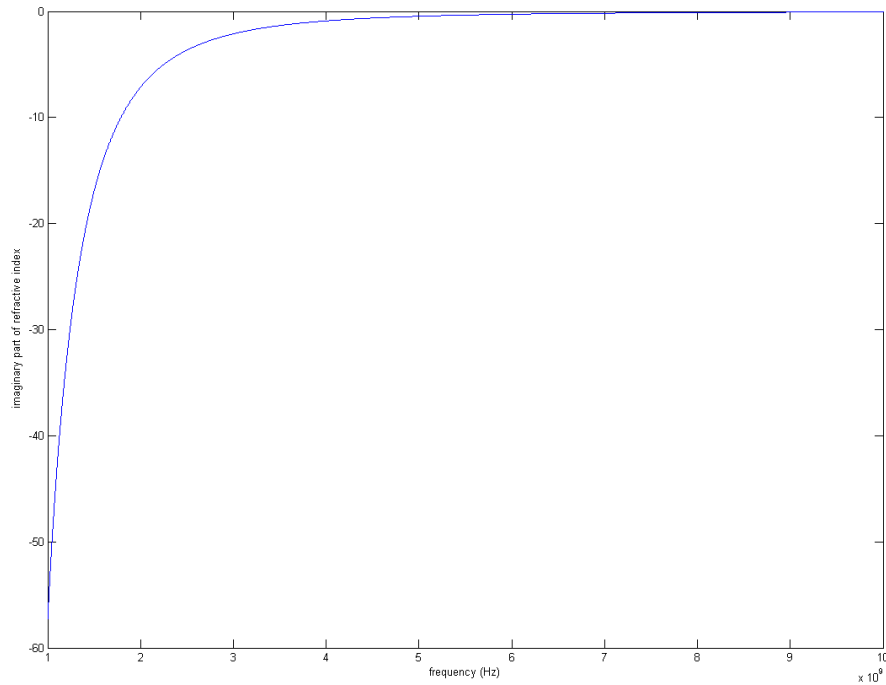


Figure 18 The imaginary part of the refractive index. The frequency axis is from 1 GHz to 10 GHz.

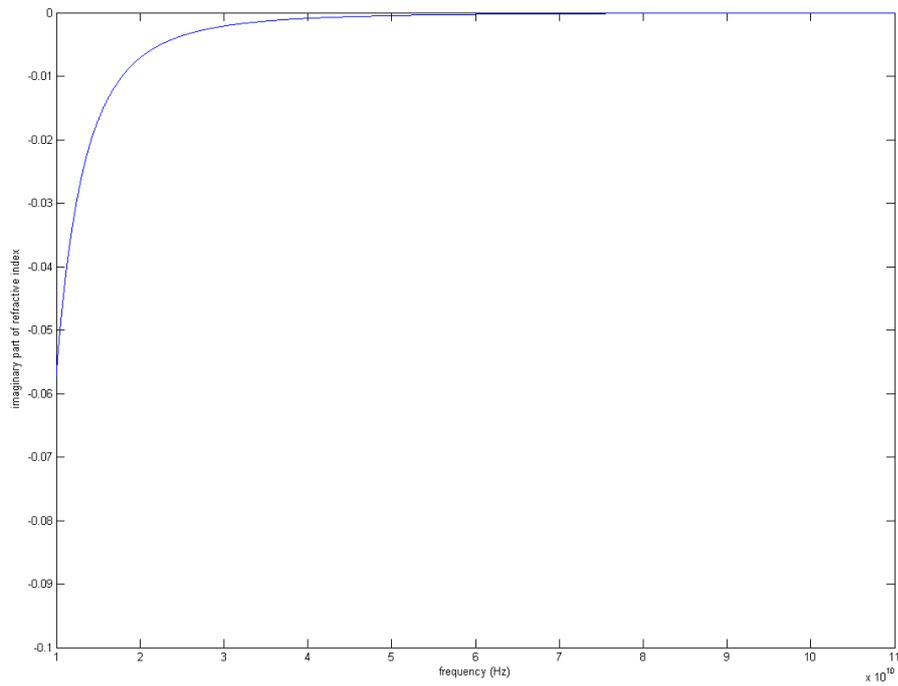


Figure 19 The imaginary part of the refractive index. The frequency axis is from 10 GHz to 110 GHz.

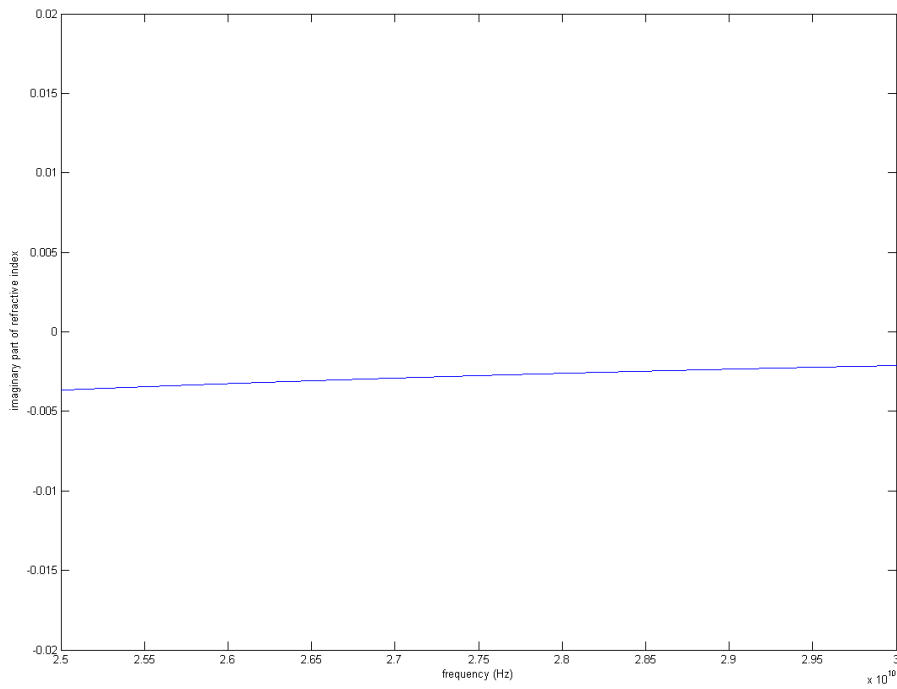


Figure 20 The imaginary part of the refractive index. The frequency axis is from 25 GHz to 30 GHz.

3.2 The Formulation of the RF Pulse

The rf pulse consists of a carrier signal and a modulating signal. The mathematical form of the rf pulse is taken from [10]. The carrier signal is a sinusoidal of the angular frequency ω_0 . The modulating signal is composed of adjustable turn-on and turn-off portions. The turn-on and turn-off portions of the modulating signal are used to control the frequency content of the rf pulse. The turn-on portion is used to control the speed at which the rf pulse starts and reaches its steady state. On the other hand, the turn-off portion controls the speed at which the rf pulse turns off. The higher the turn-on or turn-off speeds are, the bigger the amount of the high frequency content of the signal is.

The modulating signal is given as follows:

$$g_{on}(t) = 10x_{on}^3 - 15x_{on}^4 + 6x_{on}^5 \quad (37)$$

$$g_{off}(t) = 1 - (10x_{off}^3 - 15x_{off}^4 + 6x_{off}^5) \quad (38)$$

$$x_{on}(t) = 1 - \frac{(mT_p - t)}{mT_p} \quad (39)$$

$$x_{off}(t) = \frac{[t - (m + s)T_p]}{mT_p} \quad (40)$$

where T_p is the fundamental period of the carrier sinusoid. m gives the length of the turn-on interval and the length of the turn-off interval in terms of the fundamental period of the carrier signal. s gives the length of the steady-state portion in terms of the fundamental period of the carrier sinusoid. That's the mean, the turn-on and the turn-off intervals last for m times the fundamental period of the carrier sinusoid, and the steady-state portion of the rf pulse lasts for s times the fundamental period of the carrier sinusoid.

After the definitions made in the previous paragraphs, the rf pulse is formulated as follows:

$$f(t) = \begin{cases} g_{on}(t) \sin(\omega_0 t) & \text{for } 0 \leq t \leq mT_p \\ \sin(\omega_0 t) & \text{for } mT_p \leq t \leq (m+s)T_p \\ g_{off}(t) \sin(\omega_0 t) & \text{for } (m+s)T_p \leq t \leq (m+s+m)T_p \\ 0 & \text{for } (m+s+m)T_p \leq t \end{cases} \quad (41)$$

For an rf pulse obtained by modulating a carrier sinusoid of the fundamental period of 33.3 picoseconds with a modulating signal of $m = 1$ and $s = 15$, the following time domain waveform and the frequency domain waveform in the Figures 21, 22 and 23 are obtained:

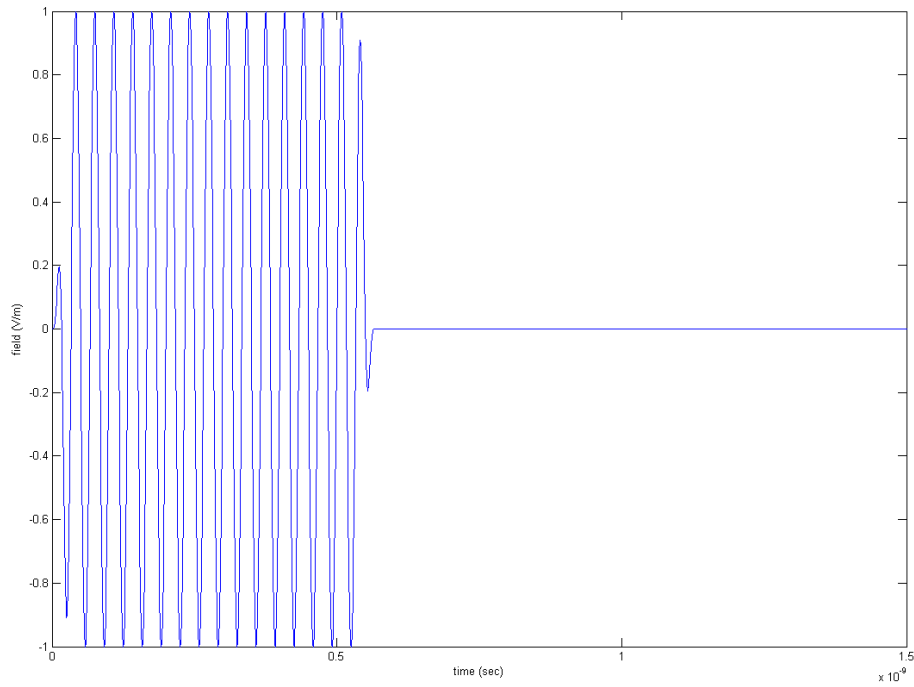


Figure 21 The rf pulse in the time domain for $m=1$, $s=15$, $T_p=33.3$ ps

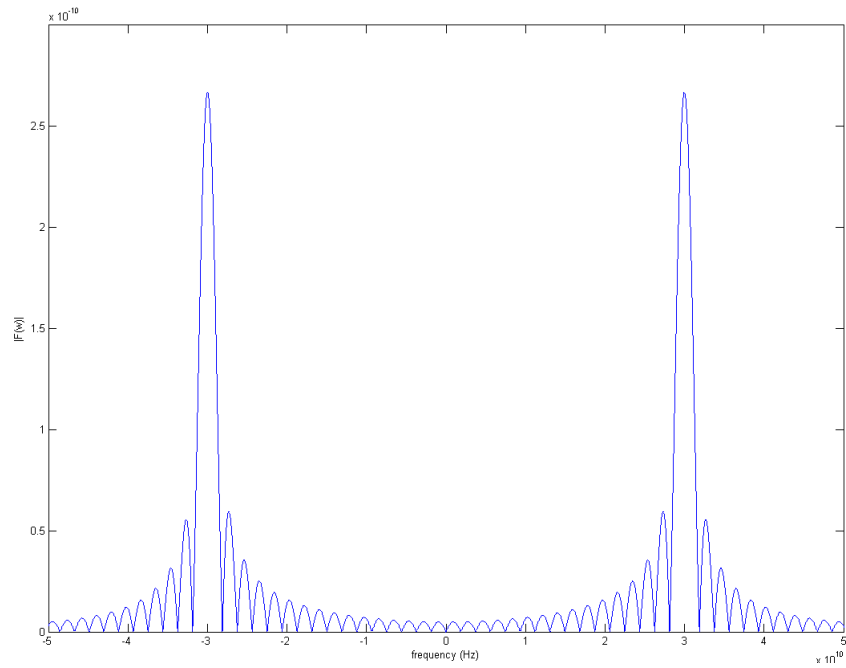


Figure 22 The rf pulse in the frequency domain $m=1$, $s=15$, $T_p=33.3$ ps. The frequency axis is from -50 GHz to 50 GHz.

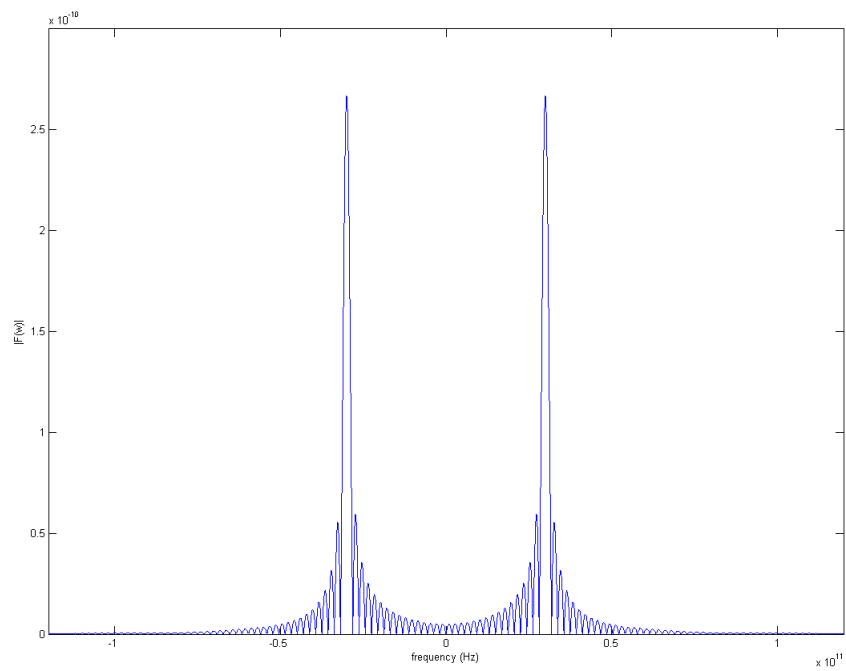


Figure 23 The rf pulse in the frequency domain $m=1$, $s=15$, $T_p=33.3$ ps. The frequency axis is from -120 GHz to 120 GHz.

Another example for the rf pulse is the one obtained by modulating a carrier sinusoid of the fundamental period of 33.3 picoseconds with a modulating signal of $m=10$ and $s=15$. The time domain waveform and the frequency domain waveform are given in the Figures 24, 25 and 26:

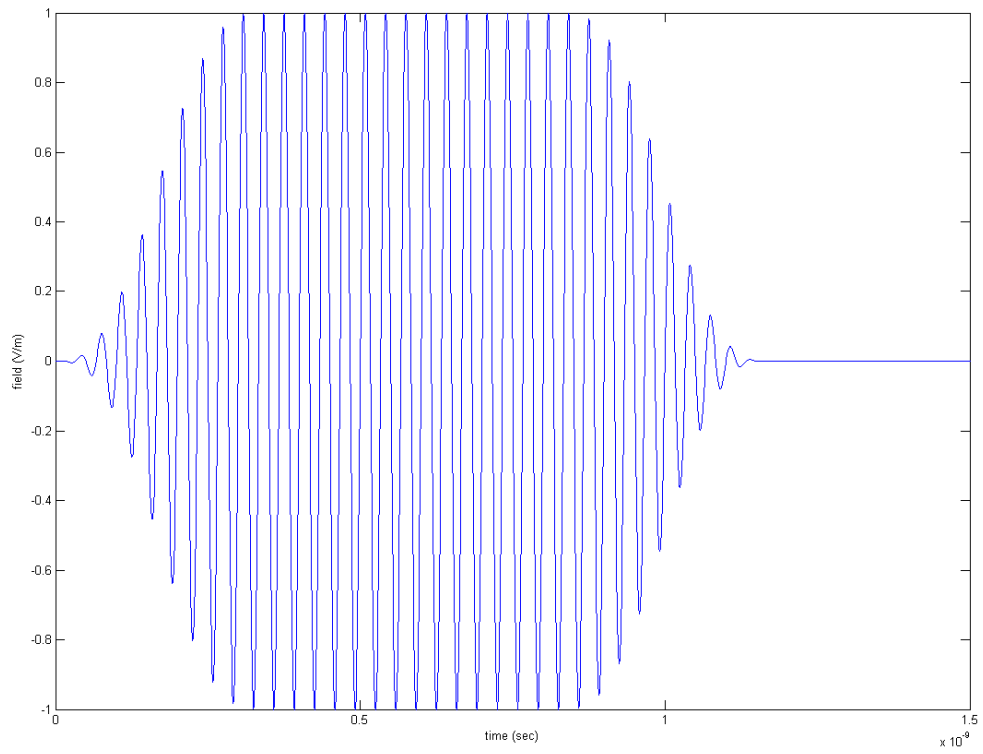


Figure 24 The rf pulse in the time domain for $m=10$, $s=15$, $T_p=33.3$ ps

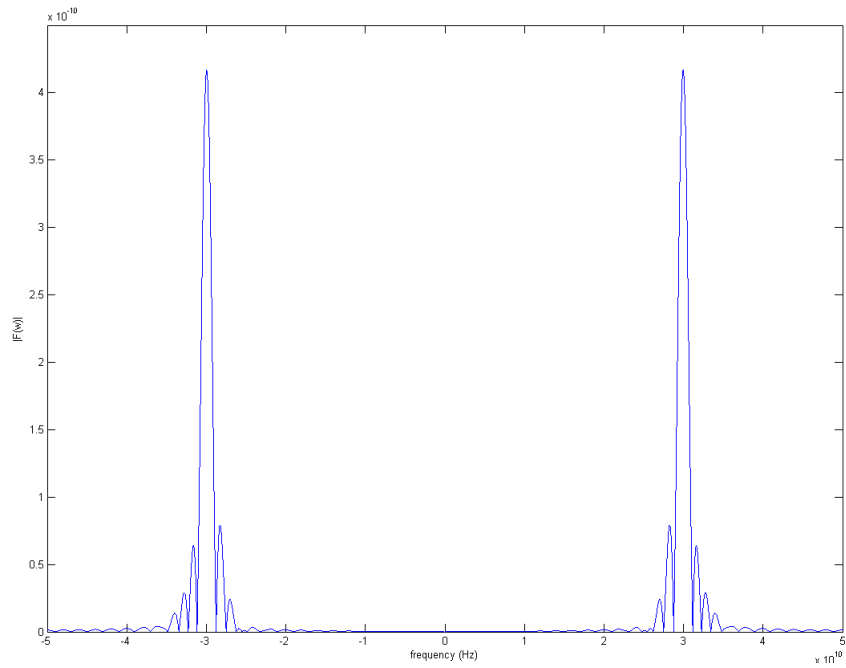


Figure 25 The rf pulse in the frequency domain $m=10$, $s=15$, $T_p=33.3$ ps. The frequency axis is from -50 GHz to 50 GHz.

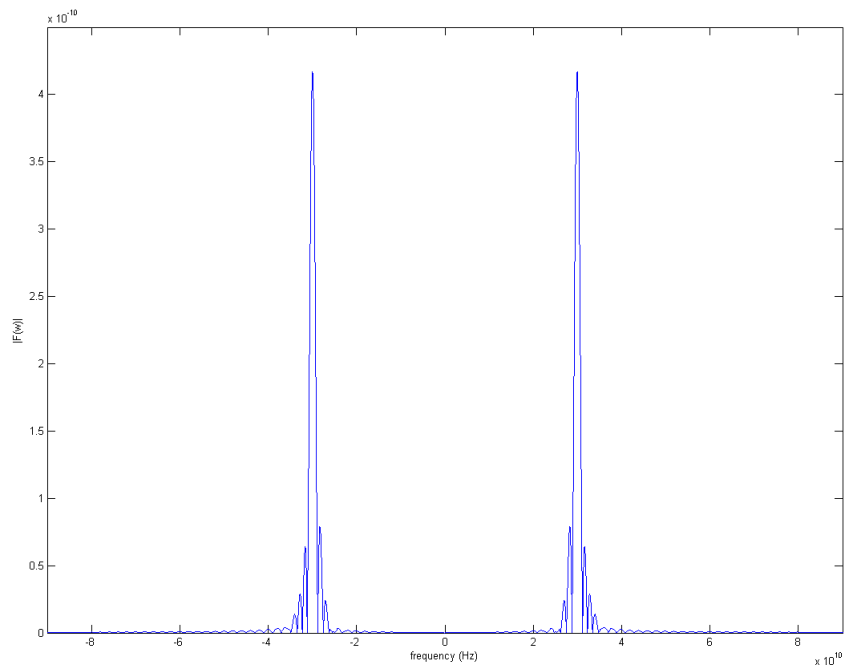


Figure 26 The rf pulse in the frequency domain $m=10$, $s=15$, $T_p=33.3$ ps. The frequency axis is from -90 GHz to 90 GHz.

If the continuous time Fourier transforms are compared, it can be easily seen that the frequency content of the first pulse is larger than that of the second pulse. This is due to the reason that the turn-on and turn-off portions of the first pulse are shorter than those of the second pulse.

3.3 The Formulation of the Propagation of the RF Pulse

The rf pulse is not a monochromatic signal. That is the mean, it is not composed of a single frequency. It has a span of frequencies as shown by its frequency domain representation. Using the continuous time Fourier transform, the rf pulse can be described as an integral sum of monochromatic complex exponentials. Each of these complex exponentials travels through the dispersive DNG medium with its own phase speed $v_{phase}(\omega)$ given by

$$v_{phase}(\omega) = \frac{c}{n(\omega)} \quad (42)$$

where c is the speed of light and $n(\omega)$ is the refractive index of the DNG medium at the specific angular frequency of ω . Hence, every monochromatic signal propagates with a different phase speed. The DNG medium behaves as a filter which shapes the rf pulse as the pulse propagates through the medium.

If the medium were not dispersive, then the phase speed would be a constant v_{phase} independent of the angular frequency ω . Assuming that $f(t)$ stands for the rf pulse, after propagating a distance of z_0 in the positive z direction, the pulse would be described by $f\left(t - \frac{z_0}{v_{phase}}\right)$. The continuous time Fourier transform pair for the rf pulse is defined as

$$F(\omega) = \mathcal{F}\{f(t)\} = \int_{-\infty}^{\infty} f(t)e^{-j\omega t} dt \quad (43)$$

$$f(t) = \frac{1}{2\pi} \int_{-\infty}^{\infty} F(\omega) e^{j\omega t} d\omega \quad (44)$$

Then, the propagating pulse can be expressed in terms of a continuous time Fourier integral using the time-shifting property of the transform as follows:

$$f\left(t - \frac{z_0}{v_{phase}}\right) = \frac{1}{2\pi} \int_{-\infty}^{\infty} \left[F(\omega) e^{-j\omega \frac{z_0}{v_{phase}}} \right] e^{j\omega t} d\omega \quad (45)$$

The effect of the dispersive medium to the continuous time Fourier transform of the rf signal as it propagates through the medium will be multiplying $F(\omega)$ by $e^{-j\omega \frac{z_0}{v_{phase}(\omega)}}$. This effect is dependent on ω and may distort the shape of the rf signal. Then, the propagating signal can be expressed as follows:

$$g(t) = \frac{1}{2\pi} \int_{-\infty}^{\infty} \left[F(\omega) e^{-j\omega \frac{z_0}{v_{phase}(\omega)}} \right] e^{j\omega t} d\omega \quad (46)$$

where $g(t)$ denotes the propagating signal.

The inverse Fourier transform operation in equation (46) is carried out using MATLAB. First, the continuous Fourier transform of the rf pulse, i.e. $F(\omega)$, is computed. Then, it is multiplied by $e^{-j\omega \frac{z_0}{v_{phase}(\omega)}}$. The inverse Fourier transform of the product is taken to obtain the propagating rf pulse in the time domain. In this observation, the reference for the observation point or the observation time is to be thought with respect to the same rf pulse propagating in a non-dispersive medium.

For an rf pulse obtained by modulating a carrier sinusoid of the fundamental period of 33.3 picoseconds with a modulating signal of $m = 1$ and $s = 15$, the propagating waveform is obtained for the observation points of $z_1 = 1.5 \text{ cm}$ and $z_2 = 1.6 \text{ cm}$ as shown in the Figure 27.

In the Figure 28, the steady-state portions of the propagating wave at close observation points reveal the double negativeness of the medium. The steady-state portion is at 30 GHz and feels the double negativeness property of the dispersive medium at this frequency with $\text{Re}\{n\} = -1$. The steady-state portion propagates to the right, i.e. the power propagation direction of the steady-state portion is towards right. The power propagation direction of the steady-state portion is the same as the propagation direction of the rf pulse. The continuous curve ($z_2 = 1.6 \text{ cm}$) is seen to be to the left of the dotted curve ($z_1 = 1.5 \text{ cm}$) despite the power propagation direction. This is due to the negative phase velocity of the steady-state portion of the pulse. It can be seen simultaneously on the same figure that the power propagation direction is opposite to the phase velocity direction in a double negative medium. The portions where the continuous waveform is to the right of the dotted waveform correspond to the spectral regions where the medium behaves as a double negative medium. The method for the determination of the double negativeness of the medium has been taken from [11].

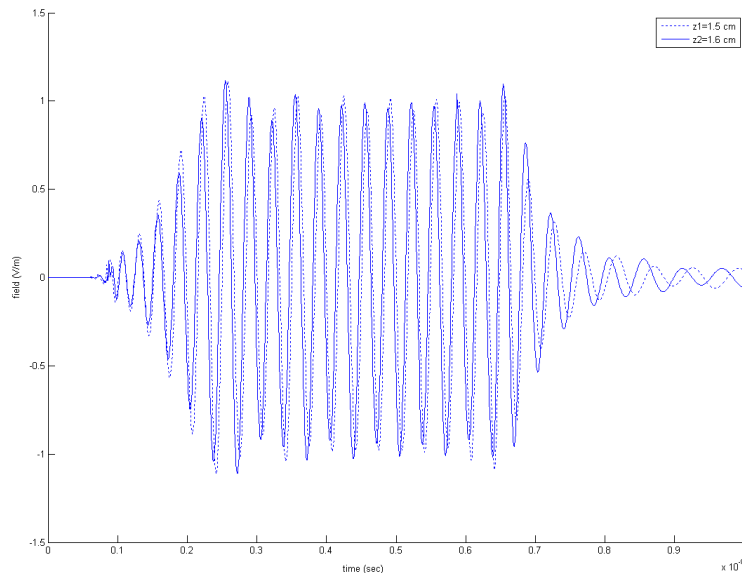


Figure 27 The propagating waveform observed at $z_1 = 1.5 \text{ cm}$ and $z_2 = 1.6 \text{ cm}$

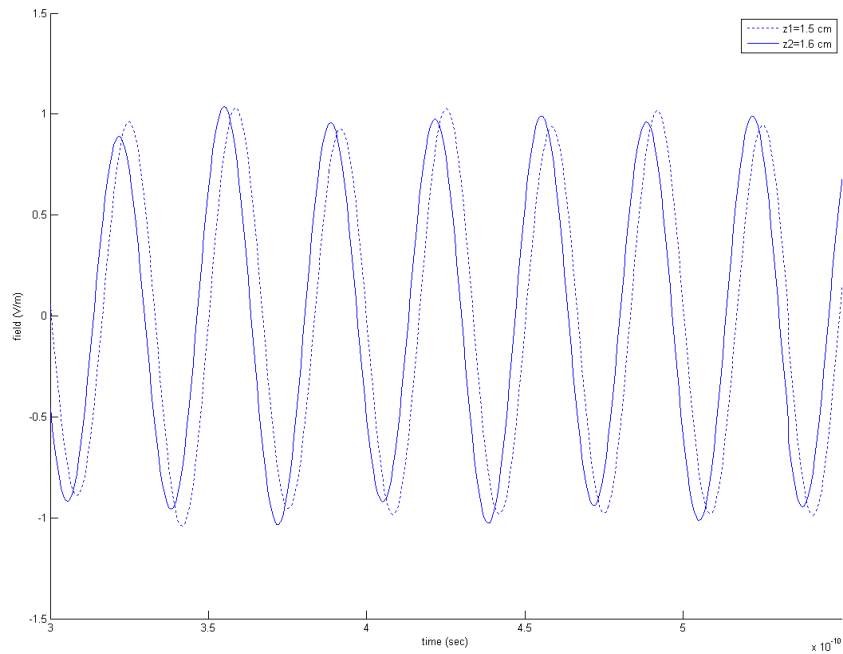


Figure 28 The continuous wave portion of the propagating pulse at $z_1 = 1.5 \text{ cm}$ and $z_2 = 1.6 \text{ cm}$

In the Figure 29, the observations made at $z_1 = 1.5 \text{ cm}$ and $z_2 = 3.0 \text{ cm}$ show that the pulse is propagating towards positive z direction although the phase velocity of the steady-state portion is towards the negative z direction. Hence, it is proven that in a DNG medium, the power propagation direction is opposite to the phase velocity direction and the causality is preserved.

For an rf pulse obtained by modulating a carrier sinusoid of the fundamental period of 33.3 picoseconds with a modulating signal of $m = 10$ and $s = 15$, the propagating waveform shown in the Figure 30 is obtained for the observation points of $z_1 = 1.5 \text{ cm}$ and $z_2 = 1.6 \text{ cm}$.

In the Figure 31, the leading edge of the propagating time domain pulse is observed. The dotted curve ($z_1 = 1.5 \text{ cm}$) starts to move before the continuous curve ($z_2 = 1.6 \text{ cm}$). This is the expected physical behavior because the medium is causal.

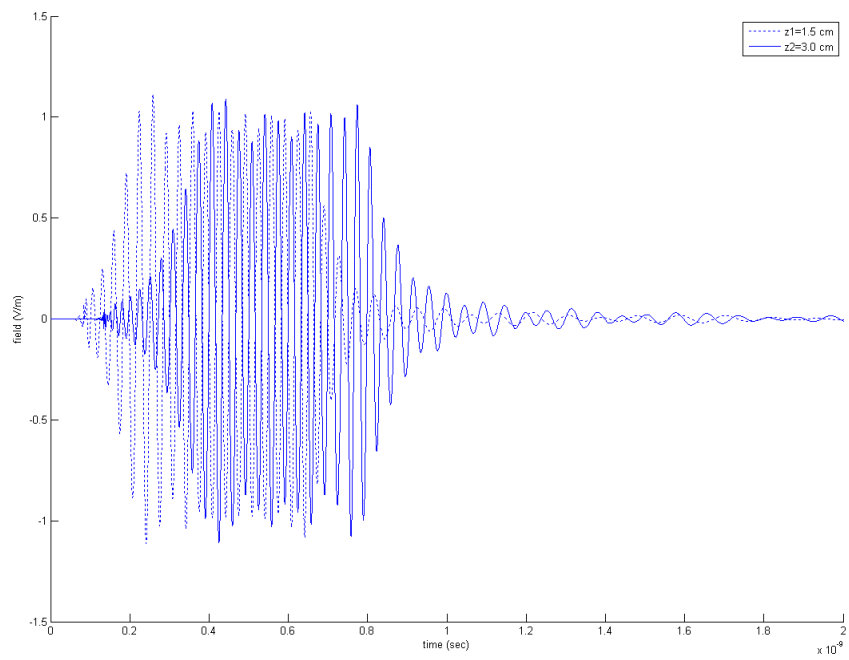


Figure 29 The propagating waveform observed at $z_1 = 1.5 \text{ cm}$ and $z_2 = 3.0 \text{ cm}$

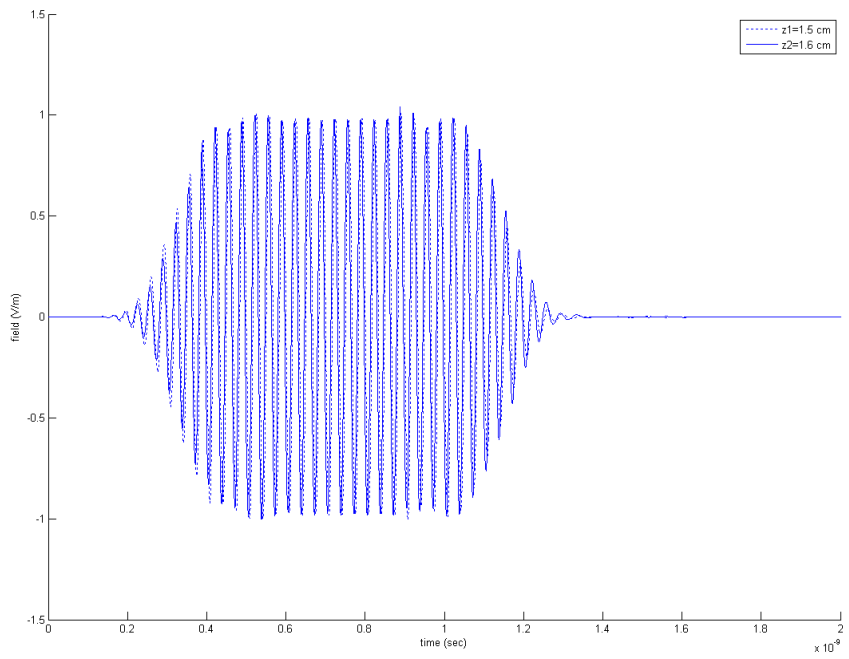


Figure 30 The propagating waveform observed at $z_1 = 1.5 \text{ cm}$ and $z_2 = 1.6 \text{ cm}$

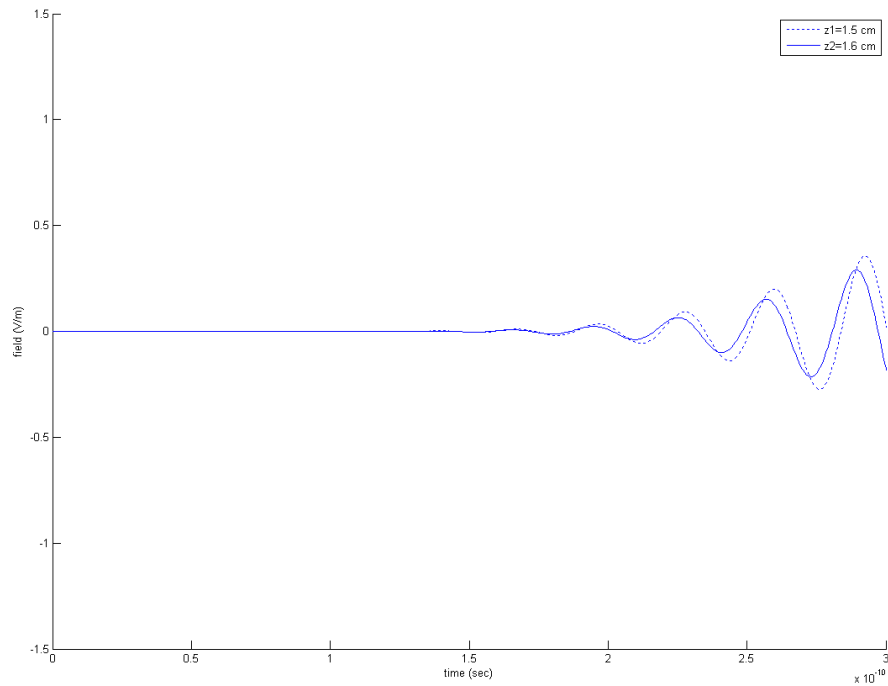


Figure 31 The leading edge of the propagating pulse at $z_1 = 1.5 \text{ cm}$ and $z_2 = 1.6 \text{ cm}$

In the Figure 32, the steady-state portion of the propagating pulse at $z_1 = 1.5 \text{ cm}$ and $z_2 = 1.6 \text{ cm}$ show that the phase velocity direction is opposite to the power propagation direction and the medium is DNG at this frequency. In this part, the continuous curve ($z_2 = 1.6 \text{ cm}$) is to the left of the dotted curve ($z_1 = 1.5 \text{ cm}$) although the power propagates to the right.

In the trailing edge of the propagating pulse, Figure 33, the continuous curve ($z_2 = 1.6 \text{ cm}$) stops later than the dotted curve ($z_1 = 1.5 \text{ cm}$). This is also in agreement with the expected physical result since the medium properties do not violate causality.

In the Figure 34, the observations made for $z_1 = 1.5 \text{ cm}$ and $z_2 = 3.0 \text{ cm}$ show that the pulse propagates towards the positive z direction although the phase velocities of the parts feeling the double negativeness of the medium are toward the negative z direction.

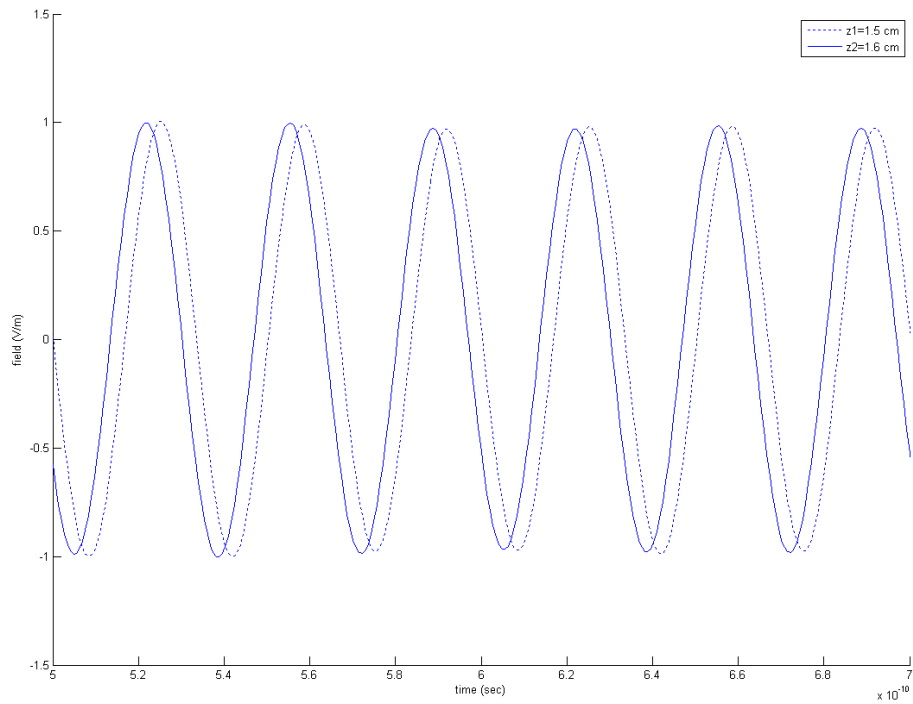


Figure 32 The continuous wave portion at $z_1 = 1.5 \text{ cm}$ and $z_2 = 1.6 \text{ cm}$

By observing the propagation of an rf pulse in a dispersive medium adjusted to be double negative at the carrier frequency of the rf pulse, it is proven that the propagation direction of the pulse, i.e. the power propagation direction, is opposite to the phase velocity directions of the rf pulse's portions which feel the double negativeness of the dispersive medium and this property does not violate causality.

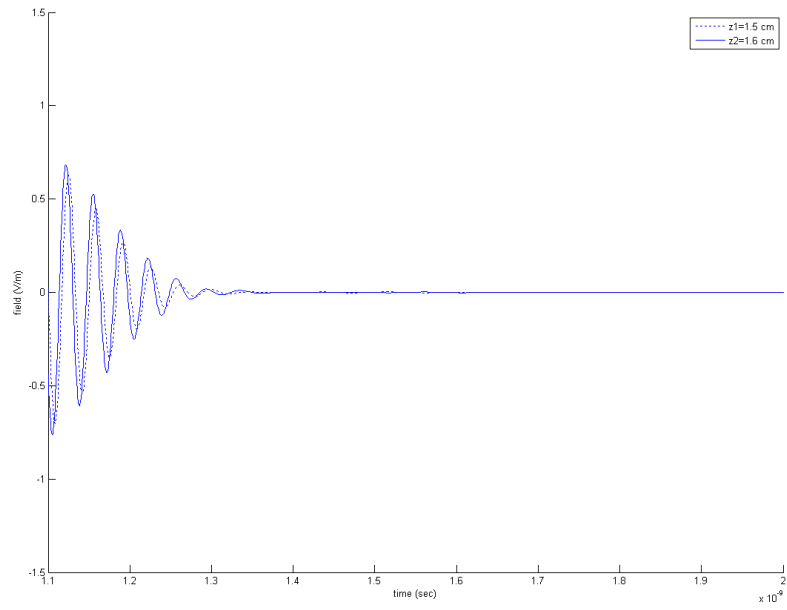


Figure 33 The trailing edge of the propagating pulse at $z_1 = 1.5 \text{ cm}$ and $z_2 = 1.6 \text{ cm}$

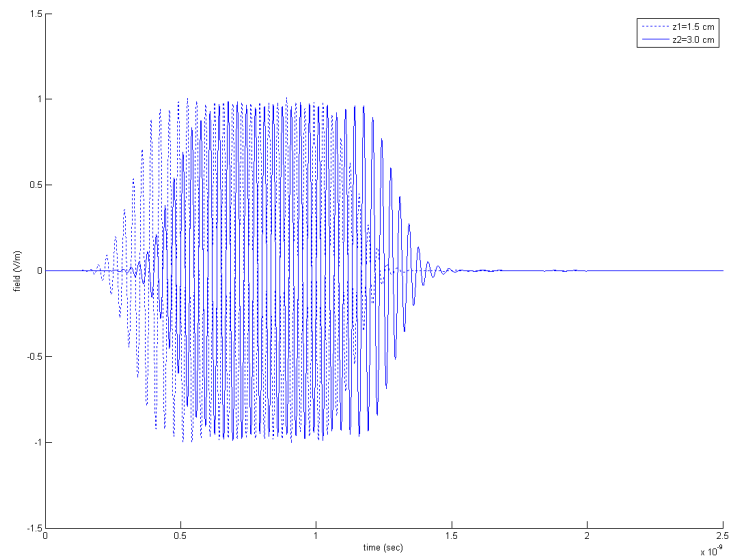


Figure 34 The propagating waveform observed at $z_1 = 1.5 \text{ cm}$ and $z_2 = 3.0 \text{ cm}$

CHAPTER 4

HIGH FREQUENCY PLANE WAVE SCATTERING BY AN INFINITELY LONG DOUBLE NEGATIVE CYLINDER

In this chapter, the scattering of a high frequency plane wave by an infinitely long cylinder is analyzed using the modified Watson transform along with the Debye expansion. Both the double positive cylinder and the double negative cylinder are examined. The contributions of the first two terms of the Debye expansion to the scattered field in the corresponding geometrical shadow and the geometrically lit regions are derived. The physical insight to the scattering problem is revealed.

In this chapter, the time harmonic dependence is fixed as $e^{-j\omega t}$. The reason of this change after the harmonic dependence of $e^{j\omega t}$ used in the third chapter is explained as in the following lines. Some of the results of this work were compared to some of the results in [28]. The time harmonic dependence in [28] is $e^{-j\omega t}$ and the time harmonic dependence of this chapter has been fixed as $e^{-j\omega t}$ due to this reason.

4.1 The Problem Description

A plane wave

$$\vec{E}^i = \hat{a}_z e^{-jk_0 x} \quad (47)$$

propagates in the negative x direction where

$$k_0 = \omega \sqrt{\mu_0 \epsilon_0} \quad (48)$$

is the free space propagation constant. A dielectric cylinder of infinite length is at the origin. The cylinder radius is a and it is assumed to be large compared to the wavelength of the incident plane wave. In other words, the operation frequency is very high. The problem geometry is given in Figure 35.

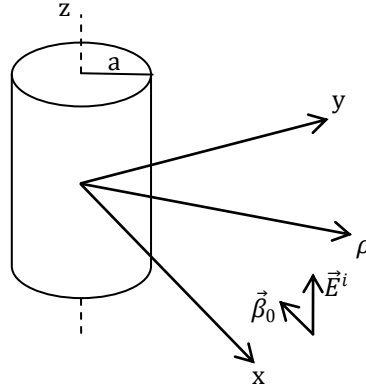


Figure 35 The problem geometry

4.2 Mie Series Solution

The incident plane wave is expanded as a series in terms of Bessel functions of the first kind as follows:

$$\vec{E}^i = \hat{a}_z \sum_{l=-\infty}^{\infty} j^{-l} J_l(k_0 \rho) e^{jl\phi} \quad (49)$$

The scattered field at the point (ρ, ϕ) can be expressed in terms of a series of Hankel functions of the first kind:

$$\vec{E}^s = \hat{a}_z \sum_{l=-\infty}^{\infty} c_l H_l^{(1)}(k_0 \rho) e^{jl\phi} \quad (50)$$

The continuity of the tangential electric field intensity and the tangential magnetic field intensity at the surface of the cylinder yields the following expression for c_l :

$$c_l = \frac{j^{-l}[-\mu_r J_l(\alpha) J_l'(\beta) + n J_l'(\alpha) J_l(\beta)]}{[\mu_r J_l(\alpha) H_l^{(1)'}(\beta) - n J_l'(\alpha) H_l^{(1)}(\beta)]} \quad (51)$$

where μ_r is the relative permeability of the cylinder, n is the refractive index of the cylinder, and

$$\beta = k_0 a \quad (52)$$

$$\alpha = n\beta \quad (53)$$

The convention for $f'(x_0)$ is given as follows:

$$f'(x_0) = \left. \frac{df}{dx} \right|_{x=x_0} \quad (54)$$

As an illustration of the Mie series solution for the scattered field, the scattered field from an infinitely long cylinder of radius one centimeter is plotted in the following figures when the cylinder is illuminated by a TM_z plane wave of 30 GHz and unit amplitude. The magnitude and the real part of the electric field intensity distribution for $0 \leq \rho \leq 2 \text{ cm}$ is displayed in the Figures 36-41. Color-bars are used to indicate the value of the displayed quantity in volts per meter. Both double positive and double negative cylinders with varying refractive indices are chosen.

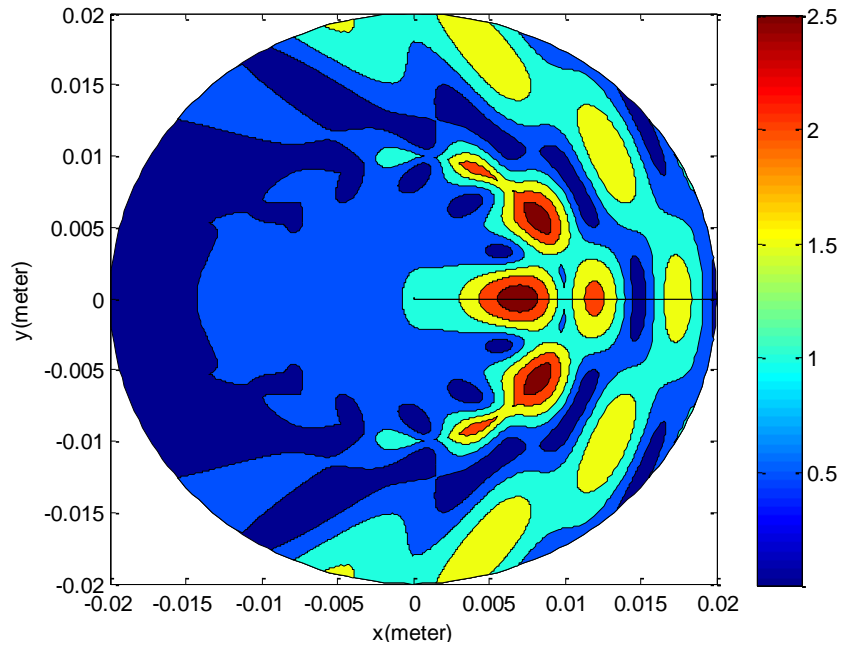


Figure 36 The magnitude of the electric field intensity distribution for $n = -1$

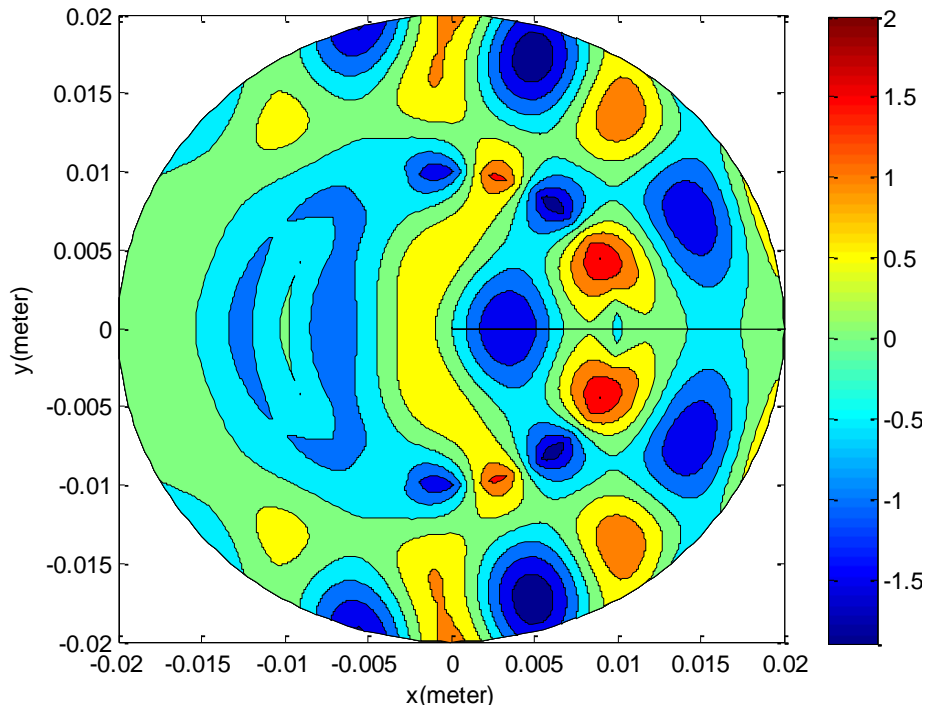


Figure 37 The real part of the electric field intensity distribution for $n = -1$

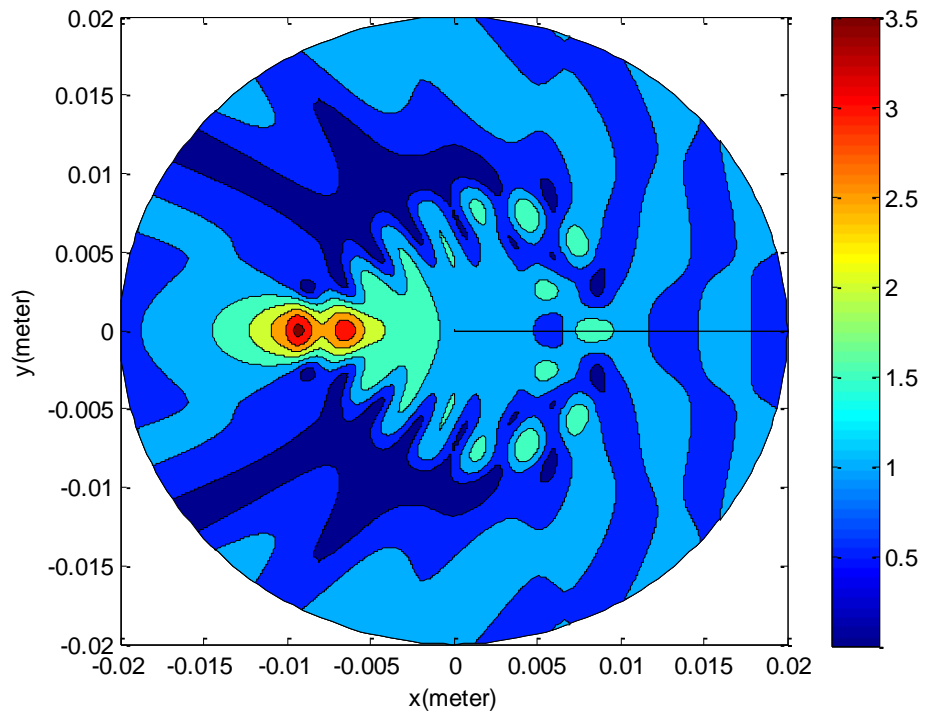


Figure 38 The magnitude of the electric field intensity distribution for $n = 2$

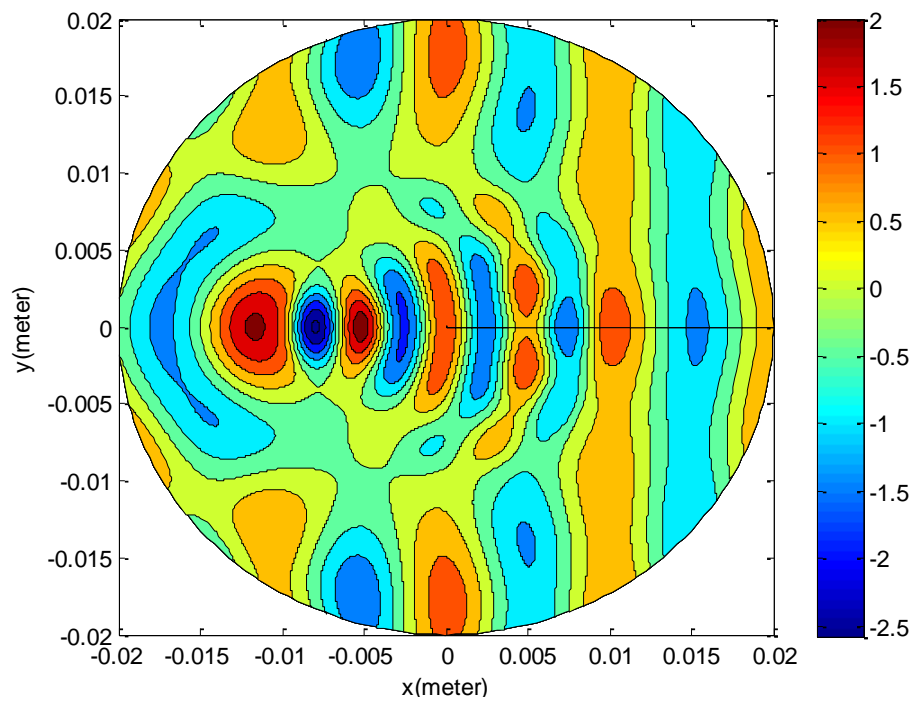


Figure 39 The real part of the electric field intensity distribution for $n = 2$

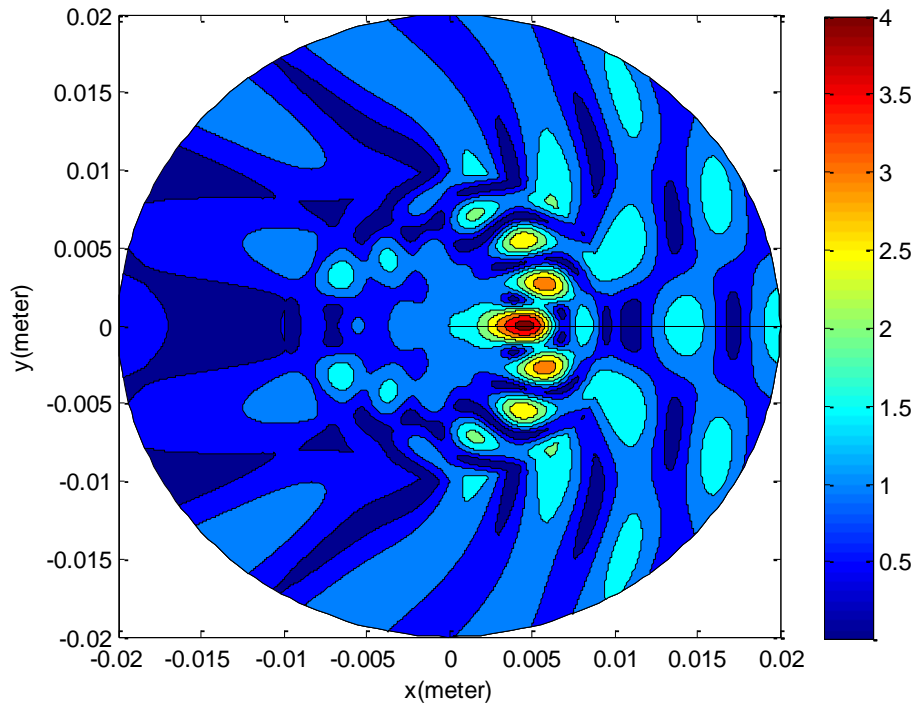


Figure 40 The magnitude of the electric field intensity distribution for $n = -2$

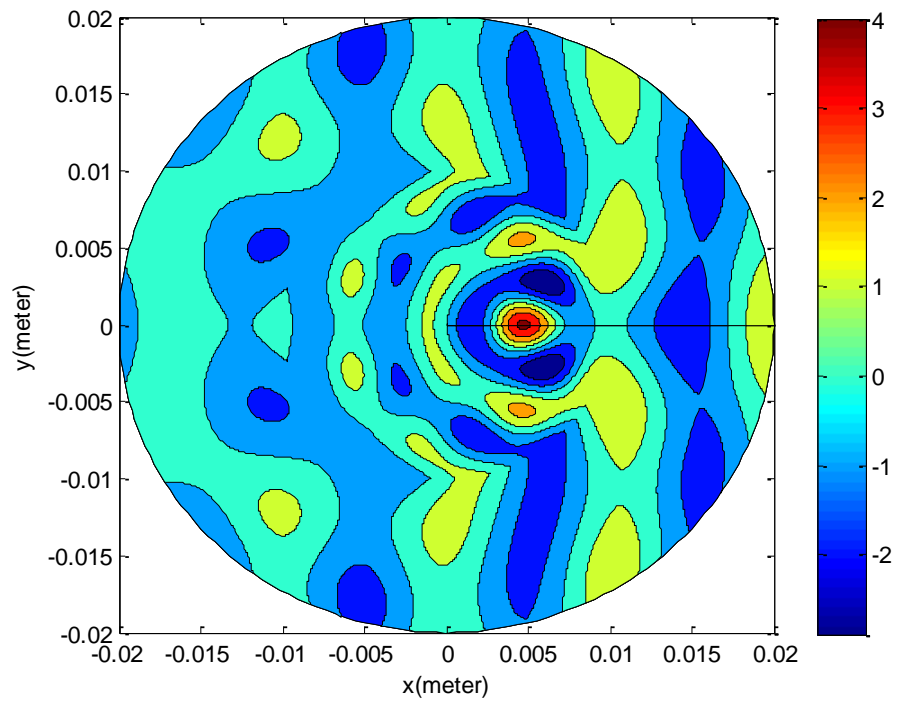


Figure 41 The real part of the electric field intensity distribution for $n = -2$

The Mie series solution for the scattered field is given by the equation (50). Theoretically, it is a sum consisting of infinite number of terms. However, at low frequencies, it converges rapidly to the solution. On the other hand, at high frequencies, the number of terms to be kept in the sum must be at least the integer closest to 2β . In the Figure 42 obtained using Mathematica, the number of terms to be kept in the Mie series for the correct result is shown versus β values. The results are for the scattering from a dielectric cylinder of the refractive index 3 and relative permeability 1. The ϕ coordinate of the field point is π radian and the ρ coordinate is $3\left(\beta + \beta^{\frac{1}{3}}\right)$.

The higher the operation frequency is, the smaller the convergence speed of the Mie series is. The convergence speed at high frequencies is low but using special package programs, such series sums can be obtained. Apart from the convergence issue, another point to consider in the high frequency scattering solution is the physics of the problem. The physical insight to the high frequency solution provides the information about the mechanisms in the scattering event. The desired physical insight does not exist in the Mie series solution. Hence, another method is required for the high frequency solution.

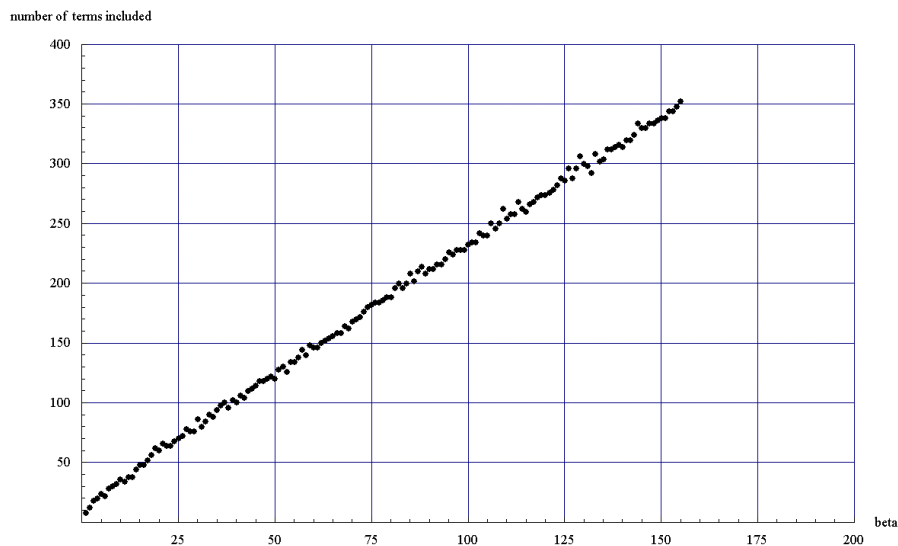


Figure 42 The number of terms to be kept in the Mie series versus beta

4.3 The Modified Watson Transform

The modified Watson transform is the method used in achieving a fast converging solution with physical insight into the scattering mechanism.

First, the Mie series is converted to an integral. The conversion is carried out using the following equality:

$$\sum_{l=-\infty}^{\infty} f(l)e^{-jl\phi} = \frac{1}{2j} \int_{C_1+C_2} \left[\frac{f(v)e^{-jv(\phi-\pi)}}{\sin(v\pi)} \right] dv \quad (55)$$

where the integration contours C_1 and C_2 are shown in the Figure 43.

If two functions p and q are analytic at a point z_0 and

$$p(z_0) \neq 0, q(z_0) = 0, q'(z_0) = \left. \frac{dq}{dz} \right|_{z=z_0} \neq 0$$

then z_0 is a simple pole of the quotient $\frac{p(z)}{q(z)}$ and the residue at this simple pole is $\frac{p(z_0)}{q'(z_0)}$.

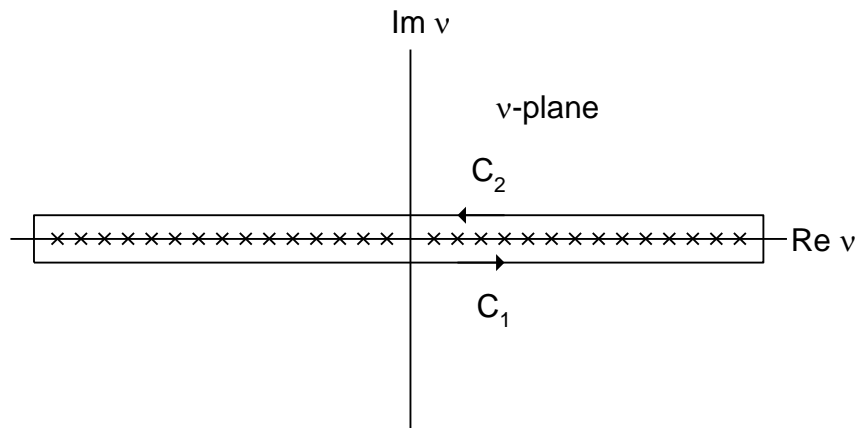


Figure 43 The integration contours C_1 and C_2

Using the mentioned theorem and assuming that

$$p(v) = f(v)e^{-jv(\phi-\pi)}, q(v) = \sin(v\pi),$$

the residue of the quotient $\frac{f(v)e^{-jv(\phi-\pi)}}{\sin(v\pi)}$ at the simple pole v which is an integer is given by

$$\text{Res} \left\{ \frac{f(v)e^{-jv(\phi-\pi)}}{\sin(v\pi)} \right\} = \frac{f(v)e^{-jv(\phi-\pi)}}{\pi \cos(v\pi)} \quad (56)$$

The Cauchy integral formula implies that the integral

$$\int_{C_1+C_2} \left[\frac{f(v)e^{-jv(\phi-\pi)}}{\sin(v\pi)} \right] dv$$

is equal to the $2\pi j$ times the sum of the residues of the integrand at the integrand's poles which are enclosed by the closed contour $(C_1 + C_2)$. Then,

$$\begin{aligned} \int_{C_1+C_2} \left[\frac{f(v)e^{-jv(\phi-\pi)}}{\sin(v\pi)} \right] dv &= 2\pi j \sum_{l=-\infty}^{\infty} \frac{f(l)e^{-jl(\phi-\pi)}}{\pi \cos(l\pi)} \\ &= 2j \sum_{l=-\infty}^{\infty} f(l)e^{-jl\phi} \end{aligned} \quad (57)$$

Equation (57) is the equation (55). Hence, the equality in equation (55) is proven.

The scattered field at the point $(\rho, -\phi)$ which is the same as the scattered field at the point (ρ, ϕ) due to the symmetry of the problem can now be written as the following integral:

$$\begin{aligned} \vec{E}^s &= \hat{a}_z \sum_{l=-\infty}^{\infty} c_l H_l^{(1)}(k_0 \rho) e^{-jl\phi} \\ &= \hat{a}_z \frac{1}{2j} \int_{C_1+C_2} \left[\frac{c_v H_v^{(1)}(k_0 \rho) e^{-jv(\phi-\pi)}}{\sin(v\pi)} \right] dv \end{aligned} \quad (58)$$

The integration contour consists of two parts. The first part C_1 is in the upper half of the complex v -plane and the second part C_2 is in the lower half of the

complex v -plane. In order to make the integration contour be completely in the upper half, the following Laurent series expansions for $\frac{1}{z}$ are used:

$$\frac{1}{z} = \sum_{m=0}^{\infty} (-1)^m (z-1)^m \text{ for } |z-1| < 1 \quad (59)$$

$$\frac{1}{z} = - \sum_{m=-\infty}^{-1} (-1)^m (z-1)^m \text{ for } |z-1| > 1 \quad (60)$$

Putting $z = 1 + e^{j2\pi(v-\frac{1}{2})}$ in the place of z in the Laurent series expansions in equations (59) and (60), the following Laurent series expansions for $\frac{1}{\sin(v\pi)}$ are obtained:

$$\frac{1}{\sin(v\pi)} = 2 \sum_{m=0}^{\infty} (-1)^m e^{[j(2m+1)\pi(v-\frac{1}{2})]} \text{ for } \text{Im}\{v\} > 0 \quad (61)$$

$$\frac{1}{\sin(v\pi)} = -2 \sum_{m=-\infty}^{-1} (-1)^m e^{[j(2m+1)\pi(v-\frac{1}{2})]} \text{ for } \text{Im}\{v\} < 0 \quad (62)$$

After inserting the derived expansions into the integral for the scattered field, the new form of the integral becomes as

$$\begin{aligned} E_s = & \frac{1}{2j} \int_{-\infty-j\varepsilon}^{\infty-j\varepsilon} c_v H_v^{(1)}(k_0 \rho) e^{-jv(\phi-\pi)} \left[-2 \sum_{m=-\infty}^{-1} (-1)^m e^{j(2m+1)\pi(v-\frac{1}{2})} \right] dv \\ & + \\ & \frac{1}{2j} \int_{-\infty+j\varepsilon}^{\infty+j\varepsilon} c_v H_v^{(1)}(k_0 \rho) e^{-jv(\phi-\pi)} \left[-2 \sum_{m=0}^{\infty} (-1)^m e^{j(2m+1)\pi(v-\frac{1}{2})} \right] dv \end{aligned} \quad (63)$$

where ε is an arbitrarily small positive number. In equation (63), in the first integral the integration variable v is changed to $-v$ to get the following expression for the scattered field:

$$\begin{aligned}
E_s = & \\
& -\frac{1}{2j} \int_{-\infty+j\varepsilon}^{\infty+j\varepsilon} c_{-v} H_{-v}^{(1)}(k_0 \rho) e^{jv(\phi-\pi)} \left[2 \sum_{m=-\infty}^{-1} (-1)^m e^{j(2m+1)\pi(-v-\frac{1}{2})} \right] dv \\
& + \\
& -\frac{1}{2j} \int_{-\infty+j\varepsilon}^{\infty+j\varepsilon} c_v H_v^{(1)}(k_0 \rho) e^{-jv(\phi-\pi)} \left[2 \sum_{m=0}^{\infty} (-1)^m e^{j(2m+1)\pi(v-\frac{1}{2})} \right] dv
\end{aligned} \tag{64}$$

Hence, the integration contour is now completely in the upper half of the complex v -plane. In order to simplify the expression for the scattered field, the series' in the integrands are explicitly written and compared with each other to detect if there is a similarity.

$$\begin{aligned}
& \sum_{m=-\infty}^{-1} (-1)^m e^{j(2m+1)\pi(-v-\frac{1}{2})} \\
& = \\
& -e^{j\pi v} e^{j\frac{\pi}{2}} + e^{j3\pi v} e^{j3\frac{\pi}{2}} - e^{j5\pi v} e^{j5\frac{\pi}{2}} + e^{j7\pi v} e^{j7\frac{\pi}{2}} - \dots
\end{aligned} \tag{65}$$

$$\begin{aligned}
& \sum_{m=0}^{\infty} (-1)^m e^{j(2m+1)\pi(v-\frac{1}{2})} \\
& = \\
& e^{j\pi v} e^{-j\frac{\pi}{2}} - e^{j3\pi v} e^{-j3\frac{\pi}{2}} + e^{j5\pi v} e^{-j5\frac{\pi}{2}} - e^{j7\pi v} e^{-j7\frac{\pi}{2}} + \dots
\end{aligned} \tag{66}$$

The explicit form of the series shows that they are in fact the same as each other. Then, the scattered field can now be written in a simpler form:

$$E^s = \sum_{l=-\infty}^{\infty} c_l H_l^{(1)}(k_0 \rho) e^{-jl\phi} =$$

$$-\frac{1}{2j} \int_{-\infty+j\varepsilon}^{\infty+j\varepsilon} [c_{-v} H_{-v}^{(1)}(k_0 \rho) e^{jv(\phi-\pi)} + c_v H_v^{(1)}(k_0 \rho) e^{-jv(\phi-\pi)}] \left[2 \sum_{m=0}^{\infty} (-1)^m e^{j(2m+1)\pi(v-\frac{1}{2})} \right] dv$$
(67)

The scattered field expression has been converted to an integral given by (67). This procedure is called the modified Watson transform.

4.4 The Debye Expansion

The Cauchy integral formula is one of the possible ways for calculating the integral in (67). It is necessary to examine the poles of the integrand in the upper half of the complex v -plane to use the Cauchy integral formula. The integral in (67) is composed of two parts. The first part is

$$-\frac{1}{2j} \int_{-\infty+j\varepsilon}^{\infty+j\varepsilon} [c_{-v} H_{-v}^{(1)}(k_0 \rho) e^{jv(\phi-\pi)}] \left[2 \sum_{m=0}^{\infty} (-1)^m e^{j(2m+1)\pi(v-\frac{1}{2})} \right] dv$$
(68)

and the second part is

$$-\frac{1}{2j} \int_{-\infty+j\varepsilon}^{\infty+j\varepsilon} [c_v H_v^{(1)}(k_0 \rho) e^{-jv(\phi-\pi)}] \left[2 \sum_{m=0}^{\infty} (-1)^m e^{j(2m+1)\pi(v-\frac{1}{2})} \right] dv$$
(69)

The poles of the second part are the poles of c_v given by

$$c_v = \frac{j^{-v} [-\mu_r J_v(\alpha) J'_v(\beta) + n J'_v(\alpha) J_v(\beta)]}{[\mu_r J_v(\alpha) H_v^{(1)'}(\beta) - n J'_v(\alpha) H_v^{(1)'}(\beta)]}$$
(70)

It is possible to write the equations with Bessel and Hankel functions in a more compact form using the following notations taken from [28]:

$$[x] \triangleq \frac{J'(x)}{J(x)} \tag{71}$$

$$[1 x] \triangleq \frac{H_v^{(1)'}(x)}{H_v^{(1)}(x)} \tag{72}$$

$$[2 x] \triangleq \frac{H_v^{(2)'}(x)}{H_v^{(2)}(x)} \tag{73}$$

The poles of c_v are the roots of

$$\mu_r J_v(\alpha) H_v^{(1)'}(\beta) - n J_v'(\alpha) H_v^{(1)}(\beta) = 0 \tag{74}$$

Making use of the notations, equation (74) can be written in a more compact form:

$$[1 \beta] = \frac{n}{\mu_r} [\alpha] \tag{75}$$

The roots of equation (75) can be collected in two groups. One group consists of those which are almost parallel to the real v -axis and the other group contains those which are almost parallel to the imaginary v -axis. The poles of the integrand are shown in Figure 44.

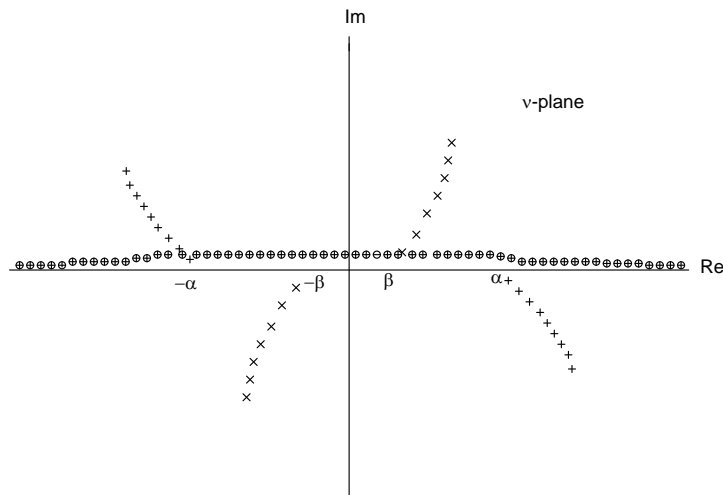


Figure 44 The roots of equation (75)

It is necessary to calculate the residues of the integrand at these two groups of poles and sum the residues up for the computation of the integral (69). Due to the fact that the residues at the poles which are almost parallel to the imaginary v -axis are fast decaying exponentials, the sum of these residues quickly converges to a result. However, the residues at the poles which are almost parallel to the real v -axis are not fast decaying exponentials. Their sum does not converge to a result rapidly. Due to the poor convergence property of the sum of these residues, it is not an efficient way to calculate the integral (69) by using the Cauchy integral formula. The integral (68) is similar to the integral (69).

At high frequency, the incident plane wave can be thought to be made up of incident rays. Each ray incident on the dielectric cylinder is reflected and refracted infinitely many times by the cylinder. Let a ray be traced in this series. After arriving at the surface of the cylinder, some part of it is reflected and the rest is transmitted into the cylinder by refraction. The first term in the series is formed by the reflection of the ray to the outside of the cylinder. The contribution to the scattered field as the first term is made by this reflected part. The transmitted part of the ray hits the surface from inside after traveling in the

cylinder. Then, some part of it is reflected and the rest is transmitted to the outside. The contribution to the scattered field as the second term in the series is made by this transmitted part. The third term in the series is the part which is formed after the first transmission into the cylinder, then reflection from inside the cylinder, and then transmission to the outside of the dielectric cylinder. The scattering mechanism described in the above is shown in Figure 45. The series is constructed in this way and converges to the scattered field at the end.

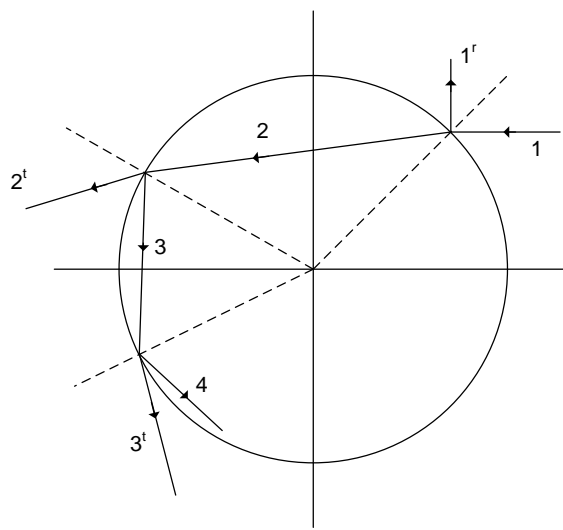


Figure 45 The scattering mechanism at high frequency

The physical picture in Figure 45 is valid for the problem at high frequency. This physical insight to the scattering problem is used for the scattering amplitude calculation due to a penetrable sphere in [28], for calculation of the scattered wave function of an impenetrable sphere in [27]. The problem of scattering by a dielectric cylinder can be attacked by using a similar model. The scattered field is a linear combination of infinite number of Hankel functions of the first kind scaled by the scattering coefficients c_l . The series of reflections and transmissions of cylindrical waves shape the scattering field coefficients into their final forms. Hence, the scattering phenomenon given in the Figure 45 must be mathematically represented by the coefficients c_l . In

[28], a quantity called S-function is decomposed into a series of reflection and transmission terms to mathematically express the physical picture in the Figure 45. Depending on this information and the fact that the scattering coefficients c_l is the overall mathematical representation of Figure 45, it is deduced that c_l must be able to be written in terms of the S-function which is denoted as x_l in this analysis and given in the equation (76). By writing c_l in terms of x_l , c_l is analyzed in terms of the mathematical building blocks of the whole physical picture and the Debye expansion is carried out.

x_l is defined as follows:

$$x_l = \frac{H_l^{(2)}(\beta)}{H_l^{(1)}(\beta)} \left\{ R_{22}(l, \beta) + T_{21}(l, \beta) T_{12}(l, \beta) \frac{H_l^{(1)}(\alpha)}{H_l^{(2)}(\alpha)} \sum_{p=1}^{\infty} \left[R_{11}(l, \beta) \frac{H_l^{(1)}(\alpha)}{H_l^{(2)}(\alpha)} \right]^{p-1} \right\} \quad (76)$$

where

$$\left| R_{11}(l, \beta) \frac{H_l^{(1)}(\alpha)}{H_l^{(2)}(\alpha)} \right| < 1$$

In the equation (76), the reflection coefficient for the cylindrical wave represented by the Hankel function of the first kind incident from inside of the cylinder to the surface is $R_{11}(l, \beta)$. The reflection coefficient for the cylindrical wave represented by the Hankel function of the second kind incident from outside of the cylinder to the surface is $R_{22}(l, \beta)$. The transmission coefficient for the cylindrical wave represented by the Hankel function of the first kind incident from inside of the cylinder to the surface is $T_{12}(l, \beta)$. The transmission coefficient for the cylindrical wave represented by the Hankel function of the second kind incident from outside of the cylinder to the surface is $T_{21}(l, \beta)$. These coefficients are mathematically expressed as follows:

$$R_{11}(l, \beta) = - \frac{[1 \beta] - \frac{n}{\mu_r} [1 \alpha]}{[1 \beta] - \frac{n}{\mu_r} [2 \alpha]} \quad (77)$$

$$R_{22}(l, \beta) = -\frac{[2 \beta] - \frac{n}{\mu_r} [2 \alpha]}{[1 \beta] - \frac{n}{\mu_r} [2 \alpha]} \quad (78)$$

$$T_{12}(l, \beta) = \frac{4j}{\pi \beta H_l^{(1)}(\alpha) H_l^{(2)}(\alpha) \left([1 \beta] - \frac{n}{\mu_r} [2 \alpha] \right)} \quad (79)$$

$$T_{21}(l, \beta) = \frac{4j}{\pi \beta H_l^{(1)}(\beta) H_l^{(2)}(\beta) \left([1 \beta] - \frac{n}{\mu_r} [2 \alpha] \right)} \quad (80)$$

The first part of x_l which is given by

$$\frac{H_l^{(2)}(\beta)}{H_l^{(1)}(\beta)} R_{22}(l, \beta) \quad (81)$$

represents the rays which are reflected by the cylinder. The rest of it given by

$$\frac{H_l^{(2)}(\beta)}{H_l^{(1)}(\beta)} T_{21}(l, \beta) T_{12}(l, \beta) \frac{H_l^{(1)}(\alpha)}{H_l^{(2)}(\alpha)} \sum_{p=1}^{\infty} \left[R_{11}(l, \beta) \frac{H_l^{(1)}(\alpha)}{H_l^{(2)}(\alpha)} \right]^{p-1} \quad (82)$$

represents the rays which are first transmitted into the cylinder, make $p - 1$ number of reflections and are transmitted to the outside of the cylinder after these $p - 1$ reflections.

It is possible to write the scattering coefficients c_l in terms of x_l as follows:

$$c_l = \frac{j^{-l}}{2} (x_l - 1) \quad (83)$$

Putting the relation in (83) into the equation (67), the scattered field is written as follows:

$$E^s = -\frac{1}{2j} \int_{-\infty+j\varepsilon}^{\infty+j\varepsilon} \left[\frac{j^v}{2} (x_{-v} - 1) H_{-v}^{(1)}(k_0 \rho) e^{jv(\phi-\pi)} + \frac{j^{-v}}{2} (x_v - 1) H_v^{(1)}(k_0 \rho) e^{-jv(\phi-\pi)} \right] \times \left[2 \sum_{m=0}^{\infty} (-1)^m e^{j(2m+1)\pi(v-\frac{1}{2})} \right] dv \quad (84)$$

The application of the Debye expansion to c_l is performed by writing c_l in terms of x_l . The Debye expansion reveals the physical mechanism in the scattering. Another use of the Debye expansion is that it makes the residue series form of the integral in (84) converge very fast in the appropriate field region. The following new equation is to be solved to find the poles:

$$[1 \beta] = \frac{n}{\mu_r} [2 \alpha] \quad (85)$$

The roots of this equation, i.e. the poles of the integrand, are almost parallel to the imaginary v -axis. The poles which are almost parallel to the real v -axis have been eliminated. Hence, the residue series is now quickly convergent. The new poles are shown in the Figure 46.

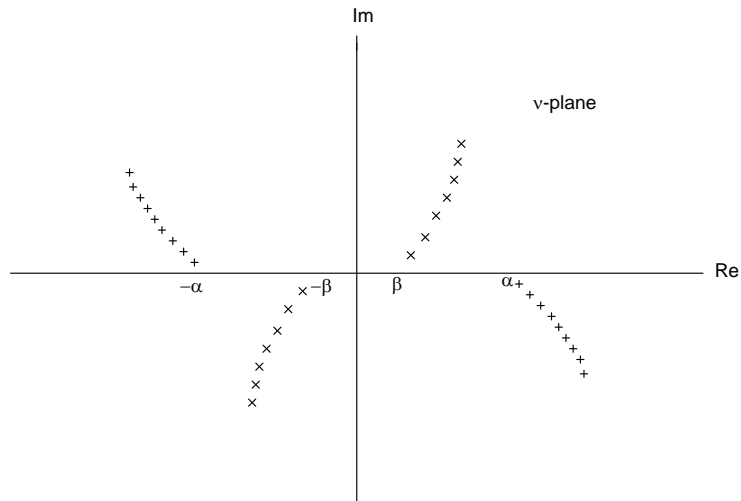


Figure 46 The roots of equation (85)

In the following sections, the contribution of the first two terms of the Debye expansion to the scattered field is computed using the scattering integral (84) and the related physical interpretation is confirmed.

4.5 The First Term of the Debye Expansion

The expression in (81) is inserted into the place of x_v in the scattered field integral in (84) to get the contribution of the first term of the Debye expansion to the scattered field:

$$\begin{aligned}
E_{first\ term}^s = & \\
& -\frac{1}{2j} \int_{-\infty+j\varepsilon}^{\infty+j\varepsilon} \left[\frac{H_{-v}^{(2)}(\beta)}{H_{-v}^{(1)}(\beta)} R_{22}(-v, \beta) - 1 \right] H_{-v}^{(1)}(k_0\rho) e^{jv(\phi-\frac{\pi}{2})} + \\
& \left[\frac{H_v^{(2)}(\beta)}{H_v^{(1)}(\beta)} R_{22}(v, \beta) - 1 \right] H_v^{(1)}(k_0\rho) e^{-jv(\phi-\frac{\pi}{2})} \times \\
& \left[\sum_{m=0}^{\infty} (-1)^m e^{j(2m+1)\pi(v-\frac{1}{2})} \right] dv
\end{aligned} \tag{86}$$

Using the information that

$$R_{22}(v, \beta) = R_{22}(-v, \beta) \tag{87}$$

the integral in equation (86) can be written in the following form:

$$\begin{aligned}
E_{first\ term}^s = & \\
& -\frac{1}{2j} \int_{-\infty+j\varepsilon}^{\infty+j\varepsilon} \left[\frac{H_{-v}^{(2)}(\beta)}{H_{-v}^{(1)}(\beta)} R_{22}(v, \beta) - 1 \right] H_{-v}^{(1)}(k_0\rho) e^{jv(\phi-\frac{\pi}{2})} + \\
& + \left[\frac{H_v^{(2)}(\beta)}{H_v^{(1)}(\beta)} R_{22}(v, \beta) - 1 \right] H_v^{(1)}(k_0\rho) e^{-jv(\phi-\frac{\pi}{2})} \times \\
& \left[\sum_{m=0}^{\infty} (-1)^m e^{j(2m+1)\pi(v-\frac{1}{2})} \right] dv
\end{aligned} \tag{88}$$

In order to examine if the integral can be written as residue series, the integrands are tested for vanishing as $|v| \rightarrow \infty$ in the upper half of the complex v -plane. Neither

$$\left[\frac{H_{-v}^{(2)}(\beta)}{H_{-v}^{(1)}(\beta)} R_{22}(v, \beta) - 1 \right] H_{-v}^{(1)}(k_0 \rho) e^{jv(\phi - \frac{\pi}{2})} e^{j(2m+1)\pi(v - \frac{1}{2})} \quad (89)$$

nor

$$\left[\frac{H_v^{(2)}(\beta)}{H_v^{(1)}(\beta)} R_{22}(v, \beta) - 1 \right] H_v^{(1)}(k_0 \rho) e^{-jv(\phi - \frac{\pi}{2})} e^{j(2m+1)\pi(v - \frac{1}{2})} \quad (90)$$

vanish as $|v| \rightarrow \infty$ in the upper half of the complex v -plane. Hence, in this form, the integrals are not appropriate to be written in the form of a residue series.

In order to make the integrals vanish in the upper half of the complex v -plane as $|v| \rightarrow \infty$, the expressions in (89) and (90) are put into the following forms:

$$\left[\frac{H_{-v}^{(2)}(\beta) H_{-v}^{(1)}(k_0 \rho)}{H_{-v}^{(1)}(\beta)} R_{22}(v, \beta) - H_{-v}^{(1)}(k_0 \rho) - H_{-v}^{(2)}(k_0 \rho) + H_{-v}^{(2)}(k_0 \rho) \right] e^{jv(\phi - \frac{\pi}{2})} e^{j(2m+1)\pi(v - \frac{1}{2})} \quad (91)$$

$$\left[\frac{H_v^{(2)}(\beta) H_v^{(1)}(k_0 \rho)}{H_v^{(1)}(\beta)} R_{22}(v, \beta) - H_v^{(1)}(k_0 \rho) - H_v^{(2)}(k_0 \rho) + H_v^{(2)}(k_0 \rho) \right] e^{-jv(\phi - \frac{\pi}{2})} e^{j(2m+1)\pi(v - \frac{1}{2})} \quad (92)$$

Putting (91) and (92) into the integral in (88) and assuming that the condition for the separation of the integral into its parts is satisfied, the following expression is obtained for the first term of the Debye expansion for the scattered field:

$$\begin{aligned}
E_{first\ term}^s = & \\
& \sum_{m=0}^{\infty} \left[\left(-\frac{1}{2j} \right) \left[\int_{-\infty+j\varepsilon}^{\infty+j\varepsilon} I_1 (-1)^m e^{-j(2m+1)\frac{\pi}{2}} dv \right] \right. \\
& + \\
& \left. \left(-\frac{1}{2j} \right) \left[\int_{-\infty+j\varepsilon}^{\infty+j\varepsilon} I_2 (-1)^m e^{-j(2m+1)\frac{\pi}{2}} dv \right] \right]
\end{aligned} \tag{93}$$

where

$$\begin{aligned}
I_1 = & \left[\frac{R_{22} H_{-v}^{(2)}(\beta) H_{-v}^{(1)}(k_0 \rho) + H_{-v}^{(1)}(\beta) H_{-v}^{(2)}(k_0 \rho)}{H_{-v}^{(1)}(\beta)} \right] e^{jv \left[\phi - \frac{\pi}{2} + (2m+1)\pi \right]} \\
& + \\
& \left[\frac{R_{22} H_v^{(2)}(\beta) H_v^{(1)}(k_0 \rho) + H_v^{(1)}(\beta) H_v^{(2)}(k_0 \rho)}{H_v^{(1)}(\beta)} \right] e^{-jv \left[\phi - \frac{\pi}{2} - (2m+1)\pi \right]}
\end{aligned} \tag{94}$$

$$\begin{aligned}
I_2 = & - \left[H_{-v}^{(1)}(k_0 \rho) + H_{-v}^{(2)}(k_0 \rho) \right] e^{jv \left[\phi - \frac{\pi}{2} + (2m+1)\pi \right]} \\
& + \\
& (-1) \left[H_v^{(1)}(k_0 \rho) + H_v^{(2)}(k_0 \rho) \right] e^{-jv \left[\phi - \frac{\pi}{2} - (2m+1)\pi \right]}
\end{aligned} \tag{95}$$

The separation of the integral in (93) into the integrals of each of I_1 and I_2 is possible only if each of the integrals of I_1 and I_2 converge. In the following sections, it will be shown that each of the integrals of I_1 and I_2 converge.

From the related section of [29], the following identities are written:

$$H_{-v}^{(1)}(z) = e^{jv\pi} H_v^{(1)}(z) \tag{96}$$

$$H_{-v}^{(2)}(z) = e^{-jv\pi} H_v^{(2)}(z) \tag{97}$$

Using the identities in (96) and (97), I_1 can be put into the following form:

$$I_1 = \left[\frac{R_{22} H_v^{(2)}(\beta) H_v^{(1)}(k_0 \rho) + H_v^{(1)}(\beta) H_v^{(2)}(k_0 \rho)}{H_v^{(1)}(\beta)} \right] \times \left\{ e^{jv \left[\phi - \frac{3\pi}{2} + (2m+1)\pi \right]} + e^{-jv \left[\phi - \frac{\pi}{2} - (2m+1)\pi \right]} \right\} \quad (98)$$

The form of the integrand in (98) vanishes as $|v| \rightarrow \infty$ in the upper half of the complex v -plane. The reason of the vanishing is the symmetry of the Hankel functions in the numerator of the integrand. The asymptotic behavior of R_{22} as $|v| \rightarrow \infty$ in the v -plane is given in the appendix B of [28]. According to this behavior, in the regions where $R_{22} \rightarrow -1$, there is a some sort of cancellation in the numerator of the integrand. The vanishing in these regions is due to the cancellation. In the region where $R_{22} \rightarrow 0$, $H_v^{(2)}(k_0 \rho)$ is the remaining cylindrical function in the numerator. However, in this region, $H_v^{(2)}(k_0 \rho)$ goes to zero as $|v| \rightarrow \infty$. Hence, the integrand in (88) is made suitable for residue series representation by means of adding and subtracting the required terms shown before.

The integral of I_1 in (93) is represented by the residue series given as follows:

$$\begin{aligned} & \sum_{m=0}^{\infty} \left[\left(-\frac{1}{2j} \right) \left[\int_{-\infty+j\varepsilon}^{\infty+j\varepsilon} I_1 (-1)^m e^{-j(2m+1)\frac{\pi}{2}} dv \right] \right] \\ & = \\ & \sum_{m=0}^{\infty} \left(-\frac{1}{2j} \right) (2\pi j) \sum_{q=1}^{\infty} \text{Res} \left\{ I_1 (-1)^m e^{-j(2m+1)\frac{\pi}{2}} \right\} \Big|_{v=v_q} \\ & = \\ & \sum_{m=0}^{\infty} (-\pi) \sum_{q=1}^{\infty} \left[(-1)^m e^{-j(2m+1)\frac{\pi}{2}} \right] \frac{4j H_v^{(1)}(k_0 \rho) \left\{ e^{jv \left[\phi - \frac{3\pi}{2} + (2m+1)\pi \right]} + e^{-jv \left[\phi - \frac{\pi}{2} - (2m+1)\pi \right]} \right\}}{\pi \beta [H_v^{(1)}(\beta)]^2 \frac{\partial}{\partial v} \left([1 \beta] - \frac{n}{\mu_r} [2 \alpha] \right)} \Big|_{v=v_q} \quad (99) \end{aligned}$$

where $v = v_q$ are the poles of the integrand I_1 . The exponential term of the residue series in (99) determines the convergence of the residue series. It is useful to make the Debye asymptotic expansion of $H_v^{(1)}(k_0\rho)$ in the residue series to find a good approximation to the residue series convergence region which is in agreement with the physical insight to the problem. The Debye asymptotic expansion taken from the appendix A of [27] is given by

$$H_v^{(1)}(z) \approx \left(\frac{2}{\pi}\right)^{\frac{1}{2}} (z^2 - v^2)^{-\frac{1}{4}} \exp\left\{j\left[(z^2 - v^2)^{\frac{1}{2}} - v \cos^{-1}\left(\frac{v}{z}\right) - \frac{\pi}{4}\right]\right\} \quad (100)$$

with the following expansion conditions

$$\left. \begin{aligned} (z^2 - v^2)^{-\frac{1}{4}} &> 0 \\ 0 &< \cos^{-1}\left(\frac{v}{z}\right) < \frac{\pi}{2} \\ -z &< v < z \\ |v - z| &> |z|^{\frac{1}{3}} \end{aligned} \right\} \quad (101)$$

The use of the asymptotic expansion in the residue series in (99) puts the overall exponential term into the following form:

$$\begin{aligned} &\exp\left\{j\left[\left((k_0\rho)^2 - v^2\right)^{\frac{1}{2}} - v \cos^{-1}\left(\frac{v}{k_0\rho}\right) - \frac{\pi}{4} + v\left[\phi - \frac{3\pi}{2} + (2m+1)\pi\right]\right]\right\} \\ &+ \\ &\exp\left\{j\left[\left((k_0\rho)^2 - v^2\right)^{\frac{1}{2}} - v \cos^{-1}\left(\frac{v}{k_0\rho}\right) - \frac{\pi}{4} - v\left[\phi - \frac{\pi}{2} - (2m+1)\pi\right]\right]\right\} \end{aligned} \quad (102)$$

The poles far away from the real axis hardly contribute to the residue series because the residue series terms exponentially decay to zero as the imaginary parts of the poles increase. Then, approximating the poles of the integrand with β in (102) is meaningful and puts the exponential term into the following form:

$$\begin{aligned}
& e^{jk_0 \left[(\rho^2 - a^2)^{\frac{1}{2}} \right]} e^{-j\frac{\pi}{4}} \exp \left\{ j \left[-v \cos^{-1} \left(\frac{a}{\rho} \right) + v \left[\phi - \frac{3\pi}{2} + (2m+1)\pi \right] \right] \right\} \\
& + \\
& e^{jk_0 \left[(\rho^2 - a^2)^{\frac{1}{2}} \right]} e^{-j\frac{\pi}{4}} \exp \left\{ j \left[-v \cos^{-1} \left(\frac{a}{\rho} \right) - v \left[\phi - \frac{\pi}{2} - (2m+1)\pi \right] \right] \right\}
\end{aligned} \tag{103}$$

The exponential expression in (103) converges provided both of the following conditions are satisfied at the same time:

$$\left. \begin{aligned}
& \operatorname{Re} \left\{ j \left[-v \cos^{-1} \left(\frac{a}{\rho} \right) + v \left[\phi - \frac{3\pi}{2} + (2m+1)\pi \right] \right] \right\} < 0 \\
& \operatorname{Re} \left\{ j \left[-v \cos^{-1} \left(\frac{a}{\rho} \right) - v \left[\phi - \frac{\pi}{2} - (2m+1)\pi \right] \right] \right\} < 0 \\
& m = 0, 1, 2, 3, 4, \dots
\end{aligned} \right\} \tag{104}$$

The poles v are in the upper half of the v -plane. Hence, the imaginary parts of the poles are positive. Then, equation (104) implies the following:

$$\left. \begin{aligned}
& -\cos^{-1} \left(\frac{a}{\rho} \right) + \phi - \frac{3\pi}{2} + (2m+1)\pi > 0 \\
& -\cos^{-1} \left(\frac{a}{\rho} \right) - \phi + \frac{\pi}{2} + (2m+1)\pi > 0 \\
& m = 0, 1, 2, 3, 4, \dots
\end{aligned} \right\} \tag{105}$$

From (105), the range of ϕ for the convergence of the residue series is given as follows:

$$\left. \begin{aligned}
& \frac{\pi}{2} + \cos^{-1} \left(\frac{a}{\rho} \right) < \phi < \frac{3\pi}{2} - \cos^{-1} \left(\frac{a}{\rho} \right) \quad \text{for } m = 0 \\
& \frac{\pi}{2} + \cos^{-1} \left(\frac{a}{\rho} \right) - 2m\pi < \phi < \frac{3\pi}{2} - \cos^{-1} \left(\frac{a}{\rho} \right) + 2m\pi \quad \text{for } m > 0
\end{aligned} \right\} \tag{106}$$

The range of ϕ when $m = 0$ corresponds to the region called the geometrical shadow region of the dielectric cylinder. The geometrical shadow region of the

dielectric cylinder for a specific ρ coordinate is shown in the Figure 47 with the following definition for ϕ_0 :

$$\phi_0 = \cos^{-1} \left(\frac{a}{\rho} \right) \quad (107)$$

The range of ϕ corresponds to the whole dielectric cylinder when $m > 0$. Hence, the intersection of the convergence ranges of ϕ is the geometrical shadow of the dielectric cylinder and the validity region of the equality in (99) is the geometrical shadow region of the cylinder for the high frequency scattering.

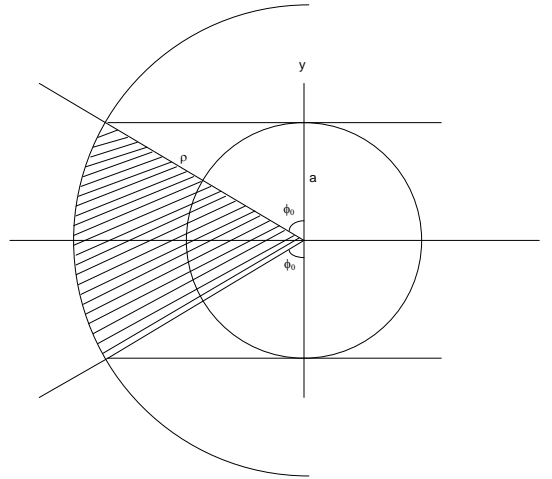


Figure 47 The geometrical shadow region of the double positive cylinder for a specific ρ coordinate corresponding to the first term of the Debye series

The exponential part of the residue series has a physical interpretation. The exponential part at point $F(\rho, \phi)$ can be written in the following form which is suitable for the interpretation:

$$\begin{aligned}
& e^{jk_0 \left[(\rho^2 - a^2)^{\frac{1}{2}} \right]} e^{-Im\{v\}(\phi_F - \phi_1 + 2m\pi)} e^{jRe\{v\}(\phi_F - \phi_1)} e^{jRe\{v\}(2m\pi)} \\
& \quad + \\
& e^{jk_0 \left[(\rho^2 - a^2)^{\frac{1}{2}} \right]} e^{-Im\{v\}(-\phi_F + \phi_2 - 2m\pi)} e^{jRe\{v\}(-\phi_F + \phi_2)} e^{jRe\{v\}(-2m\pi)}
\end{aligned} \tag{108}$$

where

$$\left. \begin{aligned}
\phi_1 &= \frac{\pi}{2} + \phi_0 \\
\phi_2 &= \frac{3\pi}{2} - \phi_0
\end{aligned} \right\} \tag{109}$$

The Figure 48 helps in making the physical interpretation of the residue series exponential part. The first part in (108) represents the diffraction of the ray hitting P_1 . At point P_1 , the incident ray has the mathematical form of $e^{-jk_0x} \Big|_{x=0}$. After hitting point P_1 , the ray travels an arc length of $|P_1T_1| = a\phi_{s1}$. Then, at point T_1 , the exponential representation of the ray becomes $e^{-jk_0x} \Big|_{x=0} \times e^{jk_0|P_1T_1|} = e^{-jk_0x} \Big|_{x=0} \times e^{jk_0a\phi_{s1}}$. After travelling on the surface to the point T_1 , the ray propagates to the field point F taking a distance of $|T_1F| = (\rho^2 - a^2)^{\frac{1}{2}}$. Then, the exponential representation of the ray is modified to be $e^{-jk_0x} \Big|_{x=0} \times e^{jk_0a\phi_{s1}} \times e^{jk_0a(\rho^2 - a^2)^{\frac{1}{2}}}$.

The ϕ coordinate of the field point F satisfies the following relation:

$$\phi|_{point F} = \phi_{s1} + \phi_1 \tag{110}$$

Hence, at point F , the exponential representation of the ray can be written as

$$e^{-jk_0x} \Big|_{x=0} \times e^{jk_0a(\rho^2 - a^2)^{\frac{1}{2}}} \times e^{jk_0a\phi_{s1}} = e^{jk_0a(\rho^2 - a^2)^{\frac{1}{2}}} \times e^{jk_0a(\phi_F - \phi_1)} \tag{111}$$

Since the real part of the poles are close to β , the first part of (108) has the same propagating exponential part as (111). Hence, the physical interpretation

for the first part of (108) has been made using the geometrical optics (GO). If $m > 0$, then the ray takes m tours in the anti-clockwise direction around the cylinder before its propagation to the field point. This is expressed by the extra $e^{jRe\{v\}(2m\pi)}$ term in (108). The propagation of the ray in the anti-clockwise direction as a creeping wave on the cylinder, the time harmonic dependence $e^{-j\omega t}$, $e^{jRe\{v\}(\phi_F - \phi_1)}$ and the sign of $Re\{v\}$ which is positive are all in good agreement with each other.

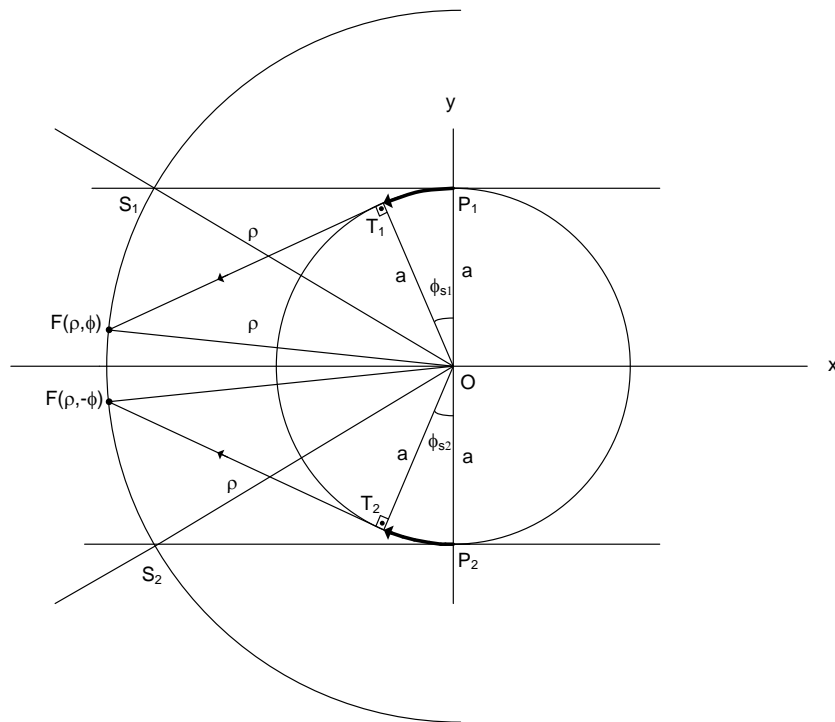


Figure 48 The mechanism of the shadow field formation by the 1st term of the Debye expansion for the double positive cylinder

The physical interpretation of the second term in (108) is similar to that of the first term. The second term is interpreted to be the diffraction of the ray to the field point $F(\rho, -\phi)$. The field at the point $F(\rho, \phi)$ and the point $F(\rho, -\phi)$ are the same due to the symmetry of the problem. Hence, there is an inherent $\frac{1}{2}$ factor in (99). The verification of the amplitude of the residue series terms are

not made theoretically using geometrical optics. The verification is to be carried out by comparing the residue series numerical results with the first term of the Debye expansion results in the fifth chapter.

The computation of the second integral in (93) requires the operation in the equation (67) to be carried out in the reverse direction. The equality in (67) is repeated for a function $f(v)$ for convenience:

$$\sum_{l=-\infty}^{\infty} f(l)e^{-jl\phi} = \left(-\frac{1}{2j}\right) \int_{-\infty}^{\infty} \{[f(-v)e^{jv(\phi-\pi)} + f(v)e^{-jv(\phi-\pi)}] \times \left[2 \sum_{m=0}^{\infty} (-1)^m e^{j(2m+1)\pi(v-\frac{1}{2})}\right]\} dv \quad (112)$$

Using the equation (112), the second integral in (93) satisfies the following equality:

$$\left(-\frac{1}{2j}\right) \left[\int_{-\infty+j\varepsilon}^{\infty+j\varepsilon} I_2 (-1)^m e^{-j(2m+1)\frac{\pi}{2}} dv \right] = - \sum_{l=-\infty}^{\infty} j^{-l} J_l(k_0\rho) e^{jl\phi} = -e^{-jk_0x} \quad (113)$$

It has now been shown that both of the integrals in (93) converge. The first integral in (93) can be written as a residue series which converges in the geometrical shadow region of the dielectric cylinder. The second integral converges without any restriction. Hence, the integral in (88) can be written as the sum of a converging residue series and $-e^{-jk_0x}$ only in the geometric shadow region of the dielectric cylinder. The term $-e^{-jk_0x}$ is called the shadow forming field of the first term of the Debye series. Since the operation frequency is high, the representation of the incident plane wave with rays is appropriate. From the physical interpretation of the residue series, it is known that the field in the geometrical shadow of the dielectric cylinder is due to the rays which creep on the surface of the dielectric cylinder and enter the geometrical shadow region. The creeping waves on the surface of the cylinder are responsible for the geometrical shadow field. The rest of the incident plane

wave cannot enter the geometrical shadow of the dielectric cylinder. The mathematical counterpart of this physical interpretation is the shadow forming field. In the geometrical shadow region, the incident plane wave exists. However, according to the physical interpretation, there must be no field except the creeping waves. The shadow forming field $-e^{-jk_0x}$ cancels the incident plane wave e^{-jk_0x} in the geometrical shadow region. The physical interpretation and the mathematical result agree with each other.

Up to this point, the whole analysis has been carried out assuming that the dielectric cylinder is not made of a DNG material. If the material is DNG, then the refractive index, the relative permeability and the relative permittivity of the material will be negative. The new equation to be solved instead of equation (85) is

$$[1 \beta] = -\frac{|n|}{|\mu_r|} [1 (|n|\beta)] \quad (114)$$

The roots of the equation (114) which are near the zeros of $H_v^{(1)}(\beta)$ are similar to those roots of the equation (85). The field in the geometrical shadow region of the DNG cylinder will be given by

$$\begin{aligned} & \sum_{m=0}^{\infty} \left[\left(-\frac{1}{2j} \right) \left[\int_{-\infty+j\epsilon}^{\infty+j\epsilon} I_1(-1)^m e^{-j(2m+1)\frac{\pi}{2}} dv \right] \right] \\ & = \\ & \sum_{m=0}^{\infty} \left(-\frac{1}{2j} \right) (2\pi j) \sum_{q=1}^{\infty} \text{Res} \left\{ I_1(-1)^m e^{-j(2m+1)\frac{\pi}{2}} \right\} \Big|_{v=v_q} \\ & = \\ & \sum_{m=0}^{\infty} (-\pi) \sum_{q=1}^{\infty} \left[(-1)^m e^{-j(2m+1)\frac{\pi}{2}} \right] \frac{4jH_v^{(1)}(k_0\rho) \left\{ e^{jv[\phi-\frac{3\pi}{2}+(2m+1)\pi]} + e^{-jv[\phi-\frac{\pi}{2}-(2m+1)\pi]} \right\}}{\pi\beta [H_v^{(1)}(\beta)]^2 \frac{\partial}{\partial v} \left([1 \beta] + \frac{n}{\mu_r} [1 (|n|\beta)] \right)} \Big|_{v=v_q} \end{aligned} \quad (115)$$

The geometrical shadow region of the DNG cylinder is the same as that of the double positive cylinder. The physical interpretation made for the double positive cylinder is also valid for the DNG cylinder.

The scattered field in the geometrical shadow region of the dielectric cylinder due to the first term of the Debye series has been calculated along with its physical interpretation. The other region of interest is the geometrically lit region of the dielectric cylinder. The ϕ angles of the field points will be chosen near zero radian to guarantee that the geometrically lit region is not left.

The residue series representation of the integral in (99) is valid in the geometrical shadow region. The residue series does not converge for $m = 0$ outside of the geometrical shadow region since the source of the scattered field is not the creeping waves. One of the regions where the residue series does not converge for $m = 0$ is the geometrically lit region. The source of the scattered field for $m = 0$ in the geometrically lit region is the rays reflected by the dielectric cylinder. The field due to reflected or transmitted rays can be calculated from the scattering integral using the steepest descent method (SDM).

The following integral is computed in the geometrically lit region:

$$\frac{1}{2} \left\{ \int_{-\infty+j\varepsilon}^{\infty+j\varepsilon} \left[\frac{R_{22}H_v^{(2)}(\beta)H_v^{(1)}(k_0\rho) + H_v^{(1)}(\beta)H_v^{(2)}(k_0\rho)}{H_v^{(1)}(\beta)} \right] \left[e^{jv(\phi-\frac{\pi}{2})} + e^{-jv(\phi-\frac{3\pi}{2})} \right] dv \right\} \quad (116)$$

The term corresponding to $m = 0$ in the integral series in the first part of equation (99) is the integral in (116). First, it is assumed that the separation of the integral in (116) into two parts is possible. The integral can be separated into two parts only if each of the parts is a convergent integral. The separation is performed in the following way:

$$\begin{aligned}
& \frac{1}{2} \left\{ \int_{-\infty+j\varepsilon}^{\infty+j\varepsilon} \left[\frac{R_{22} H_v^{(2)}(\beta) H_v^{(1)}(k_0 \rho)}{H_v^{(1)}(\beta)} \right] \left[e^{jv(\phi-\frac{\pi}{2})} + e^{-jv(\phi-\frac{3\pi}{2})} \right] dv \right\} \\
& + \\
& \frac{1}{2} \left\{ \int_{-\infty+j\varepsilon}^{\infty+j\varepsilon} H_v^{(2)}(k_0 \rho) \left[e^{jv(\phi-\frac{\pi}{2})} + e^{-jv(\phi-\frac{3\pi}{2})} \right] dv \right\}
\end{aligned} \tag{117}$$

It is necessary to apply the Debye asymptotic expansion to the integrand to compute the first integral in (117). The asymptotic expansion puts the integrand to a form which is suitable for the ray interpretation. The following Debye asymptotic expansions are applied:

$$\begin{aligned}
H_v^{(1)}(\beta) & \approx \left(\frac{2}{\pi}\right)^{\frac{1}{2}} (\beta^2 - v^2)^{-\frac{1}{4}} \exp \left\{ j \left[(\beta^2 - v^2)^{\frac{1}{2}} - v \cos^{-1} \left(\frac{v}{\beta} \right) - \frac{\pi}{4} \right] \right\} \\
H_v^{(2)}(\beta) & \approx \left(\frac{2}{\pi}\right)^{\frac{1}{2}} (\beta^2 - v^2)^{-\frac{1}{4}} \exp \left\{ -j \left[(\beta^2 - v^2)^{\frac{1}{2}} - v \cos^{-1} \left(\frac{v}{\beta} \right) - \frac{\pi}{4} \right] \right\} \\
H_v^{(1)}(k_0 \rho) & \approx \left(\frac{2}{\pi}\right)^{\frac{1}{2}} [(k_0 \rho)^2 - v^2]^{-\frac{1}{4}} \exp \left\{ j \left[[(k_0 \rho)^2 - v^2]^{\frac{1}{2}} - v \cos^{-1} \left(\frac{v}{k_0 \rho} \right) - \frac{\pi}{4} \right] \right\}
\end{aligned} \tag{118}$$

The first integral in (117) is also separated into two parts assuming that each of them is convergent. The separation is as follows:

$$\begin{aligned}
& \frac{1}{2} \left\{ \int_{-\infty+j\varepsilon}^{\infty+j\varepsilon} \left[\frac{R_{22}H_v^{(2)}(\beta)H_v^{(1)}(k_0\rho)}{H_v^{(1)}(\beta)} \right] \left[e^{jv(\phi-\frac{\pi}{2})} + e^{-jv(\phi-\frac{3\pi}{2})} \right] dv \right\} \\
& = \\
& \frac{1}{2} \left\{ \int_{-\infty+j\varepsilon}^{\infty+j\varepsilon} \left[\frac{R_{22}H_v^{(2)}(\beta)H_v^{(1)}(k_0\rho)}{H_v^{(1)}(\beta)} \right] e^{jv(\phi-\frac{\pi}{2})} dv \right\} \\
& + \\
& \frac{1}{2} \left\{ \int_{-\infty+j\varepsilon}^{\infty+j\varepsilon} \left[\frac{R_{22}H_v^{(2)}(\beta)H_v^{(1)}(k_0\rho)}{H_v^{(1)}(\beta)} \right] e^{-jv(\phi-\frac{3\pi}{2})} dv \right\}
\end{aligned} \tag{119}$$

The Debye asymptotic expansion is applied to the integrand of the first integral in (119). The first derivative of the exponential part of the integrand is taken to find the following equation for the saddle point \bar{v} :

$$2 \cos^{-1} \left(\frac{\bar{v}}{\beta} \right) - \cos^{-1} \left(\frac{\bar{v}}{k_0\rho} \right) + \phi - \frac{\pi}{2} = 0 \tag{120}$$

The following definitions are used in the solution of the equation in (120):

$$\left. \begin{aligned}
& \bar{v} = \beta \sin(w) \\
& x = \cos^{-1} \left(\frac{\bar{v}}{k_0\rho} \right) \quad \text{for } 0 < x < \frac{\pi}{2}
\end{aligned} \right\} \tag{121}$$

The solution of the equation (120) is

$$x = \frac{\pi}{2} - 2w + \phi \tag{122}$$

The saddle point is a first order saddle point. When the solution of the steepest descent equation is put into the Debye asymptotic expansion of the integrand, the following is obtained as the exponential contribution of the saddle point to the integral in the first part of (119):

$$\exp\{jk_0[-2a \cos(w) + \rho \sin(x)]\}e^{j\frac{\pi}{4}} \quad (123)$$

The exponential contribution of the saddle point to the integral has a physical interpretation to be shown using the geometric optics. The Figure 49 is to be used for the interpretation. The wave incident on the point $P(a, \theta)$ is denoted by the ray $e^{-jk_0 a \cos(\theta)}$. The exponential dependence of the reflected ray at the field point $F(\rho, \phi)$ is expressed as $e^{-jk_0 a \cos(\theta)} \times e^{(jk_0 |PF|)}$. This exponential dependence must be equal to the exponential dependence in (123) if the right matching is made between the physical picture and the saddle point evaluation of the integral. If w is chosen as being equal to θ , then the physical picture and the saddle point contribution to the integral match with each other in terms of the exponential dependence and the following equation can be written using the Figure 49:

$$jk_0[-2a \cos(w) + \rho \sin(x)] = jk_0[|PF| - a \cos(\theta)] \quad (124)$$

The matching between the two in terms of the amplitude is to be verified numerically in another chapter. Hence, as a result, it has been shown in terms of the exponential dependence that the first of the integral in (119) denotes the field at the point $F(\rho, \phi)$ due to the ray which is incident on the point $P(a, \theta)$ and is reflected by the cylinder to the field point $F(\rho, \phi)$.

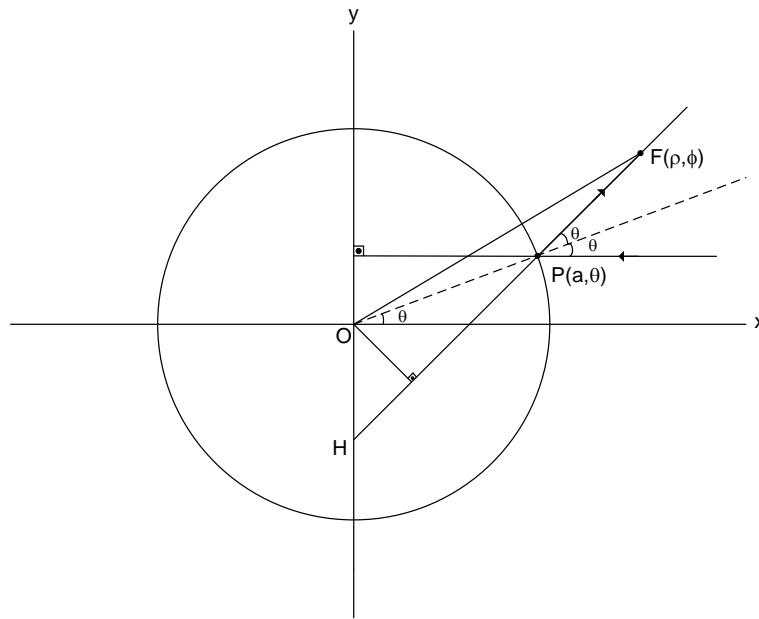


Figure 49 The physical interpretation for the geometrically lit region

In a similar way, it can be proven in terms of the exponential dependence that the second integral in (119) represents the field at the point $F(\rho, -\phi)$ due to the ray which is incident on the point $P(a, -\theta)$ and is reflected by the cylinder to the field point $F(\rho, -\phi)$.

Hence, the separation of the integral into two parts in (119) has been proven to be correct since each of the parts is convergent.

Due to the symmetry in the problem geometry, the field at $F(\rho, \phi)$ and the field $F(\rho, -\phi)$ must be equal to each other. Hence, in terms of the exponential dependence, the integral in (119) denotes the field at the point $F(\rho, \phi)$ (or $F(\rho, -\phi)$) due to the ray which is incident on the point $P(a, \theta)$ (or $P(a, -\theta)$) and is reflected by the cylinder to the field point $F(\rho, \phi)$ (or $F(\rho, -\phi)$).

It is time to calculate the second part of the integral in (117). It is assumed that the second part can be separated into two parts as follows:

$$\begin{aligned}
& \frac{1}{2} \left\{ \int_{-\infty+j\varepsilon}^{\infty+j\varepsilon} H_v^{(2)}(k_0\rho) \left[e^{jv\left(\phi-\frac{\pi}{2}\right)} + e^{-jv\left(\phi-\frac{3\pi}{2}\right)} \right] dv \right\} \\
& = \\
& \frac{1}{2} \int_{-\infty+j\varepsilon}^{\infty+j\varepsilon} H_v^{(2)}(k_0\rho) e^{jv\left(\phi-\frac{\pi}{2}\right)} dv + \frac{1}{2} \int_{-\infty+j\varepsilon}^{\infty+j\varepsilon} H_v^{(2)}(k_0\rho) e^{-jv\left(\phi-\frac{3\pi}{2}\right)} dv
\end{aligned} \tag{125}$$

After the Debye asymptotic form of the integrand of the first integral in (125) is obtained and the first derivative of the exponential part of the integrand is taken, the following equation is found for the saddle point \bar{v} :

$$\cos^{-1}\left(\frac{\bar{v}}{k_0\rho}\right) + \phi - \frac{\pi}{2} = 0 \tag{126}$$

The solution of the steepest descent equation is given by the following:

$$\bar{v} = k_0\rho \sin(\phi) \tag{127}$$

The saddle point is again a first order saddle point. The contribution of the saddle point to the first integral in equation (125) is calculated to be $\frac{1}{2} e^{-jk_0x}$.

After similar operations are carried out for the second integral in equation (125), the following steepest descent equation is obtained:

$$-\cos^{-1}\left(\frac{\bar{v}}{k_0\rho}\right) + \phi - \frac{3\pi}{2} = 0 \tag{128}$$

The solution of the steepest descent equation is

$$\bar{v} = -k_0\rho \sin(\phi) \tag{129}$$

The saddle point is a first order saddle point and the contribution of it to the second integral in equation (125) is calculated to be $\frac{1}{2} e^{-jk_0x}$.

Since each of the first and second integrals in equation (125) has been shown to converge, the separation in (125) is proven to be appropriate. Then, the second part of the integral in equation (117) is equal to e^{-jk_0x} which cancels out the shadow forming field $-e^{-jk_0x}$ in the geometrically lit region. This result is physically expected as well.

In the case of a DNG cylinder, the first part of the integral in equation (117) has a different integrand due to the R_{22} multiplier. The physical picture is the same as the double positive cylinder case. The second part of the integral in equation (117) does not change either. It cancels out the shadow forming field.

4.6 The Second Term of the Debye Expansion

Inserting the expression in (82) with p being equal to 1 into the place of x_v in the scattered field integral in (84) reveals the contribution of the second term of the Debye expansion to the scattered field. The contribution of the second term of the Debye expansion to the scattered field is expressed as follows after some operations on the integrand and setting m to 0:

$$\begin{aligned}
E_s^{second\ term} &= \frac{1}{2} \int_{-\infty+j\epsilon}^{\infty+j\epsilon} H_v^{(1)}(k_0\rho) \frac{H_v^{(2)}(\beta) H_v^{(1)}(\alpha)}{H_v^{(1)}(\beta) H_v^{(2)}(\alpha)} T_{12} T_{21} e^{jv(\phi+\frac{3\pi}{2})} dv \\
&+ \\
&\frac{1}{2} \int_{-\infty+j\epsilon}^{\infty+j\epsilon} H_v^{(1)}(k_0\rho) \frac{H_v^{(2)}(\beta) H_v^{(1)}(\alpha)}{H_v^{(1)}(\beta) H_v^{(2)}(\alpha)} T_{12} T_{21} e^{jv(-\phi+\frac{3\pi}{2})} dv
\end{aligned} \tag{130}$$

The integral is separated into two parts assuming that each of the two parts is convergent. The automatic verification of this assumption is delayed to the calculation of the integrals. The scattered field due to the rays which are transmitted into the cylinder and then transmitted out of the cylinder to form the scattered field at the field point is represented by the second term of the Debye expansion. The geometrically lit regions and geometrical shadow

regions formed by these rays are specific to the second term of the Debye series. The shaded region shown in the Figure 50 is the geometrically lit region of the cylinder for the ρ coordinate of ρ_0 , $n > \sqrt{2}$ and corresponding to the second term of the Debye series.

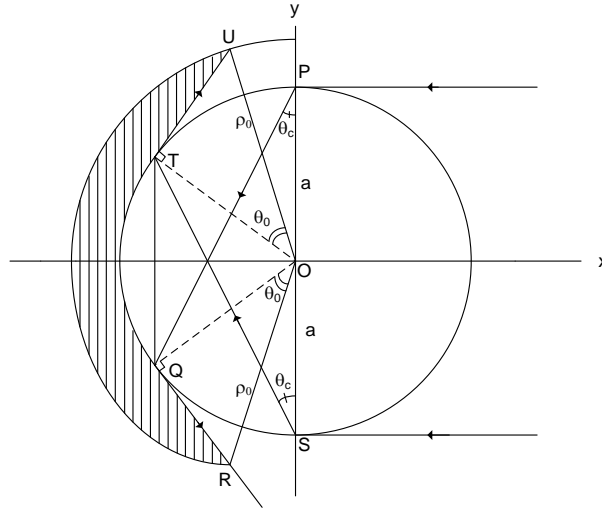


Figure 50 The geometrically lit region of the double positive cylinder for the ρ coordinate of ρ_0 and corresponding to the second term of the Debye series

First, the contribution of a typical ray to its geometrically lit region is calculated. The field in the geometrically lit region is formed by the ray propagating to the field point after transmission to the inside of the cylinder and a later transmission to the outside of the cylinder. Hence, the SDM is used for the calculation of the contribution to the scattered field.

The Debye asymptotic expansion of the second integrand in (130) is performed and the derivative of the exponential part with respect to v is taken to get the following steepest descent equation for the saddle point:

$$2 \cos^{-1} \left(\frac{\bar{v}}{\beta} \right) - \cos^{-1} \left(\frac{\bar{v}}{k_0 \rho} \right) - 2 \cos^{-1} \left(\frac{\bar{v}}{\alpha} \right) - \phi + \frac{3\pi}{2} = 0 \quad (131)$$

The following change of variable is used:

$$\bar{v} \triangleq \beta \cos(w) \quad (132)$$

Then, the steepest descent equation becomes as follows:

$$2w - \cos^{-1} \left[\frac{a}{\rho} \cos(w) \right] - 2 \cos^{-1} \left[\frac{1}{n} \cos(w) \right] - \phi + \frac{3\pi}{2} = 0 \quad (133)$$

The connection between the steepest descent equation and the physical picture for the second term of the Debye expansion is set by drawing the expected physical picture and deriving the mathematical expression related to the physical picture. As an additional check for the matching between the physical picture and the SDM evaluation of the integral, the exponential part of the scattered field obtained from the geometrical optics and the exponential part of the scattered field obtained from the SDM evaluation will be compared and detected to be the same.

From the Figure 51, the following equation can be derived:

$$2 \sin^{-1} \left[\frac{1}{n} \sin(\phi_1) \right] - 2\phi_1 + \sin^{-1} \left[\frac{a}{\rho} \sin(\phi_1) \right] = \phi - \pi \quad (134)$$

The following relations are inserted in the equation (134):

$$\left. \begin{aligned} \phi_1 &= \frac{\pi}{2} - x \\ \sin^{-1}(t) &= \frac{\pi}{2} - \cos^{-1}(t) \end{aligned} \right\} \quad (135)$$

Then, the equation (134) takes the following form:

$$2x - \cos^{-1} \left[\frac{a}{\rho} \cos(x) \right] - 2 \cos^{-1} \left[\frac{1}{n} \cos(x) \right] - \phi + \frac{3\pi}{2} = 0 \quad (136)$$

The comparison between the equation (133) and the equation (136) shows that they become the same as each other if the following equation is written for w :

$$w = x \tag{137}$$

Using the equation (135), the equation (137) can be written as follows:

$$w = \frac{\pi}{2} - \phi_1 \tag{138}$$

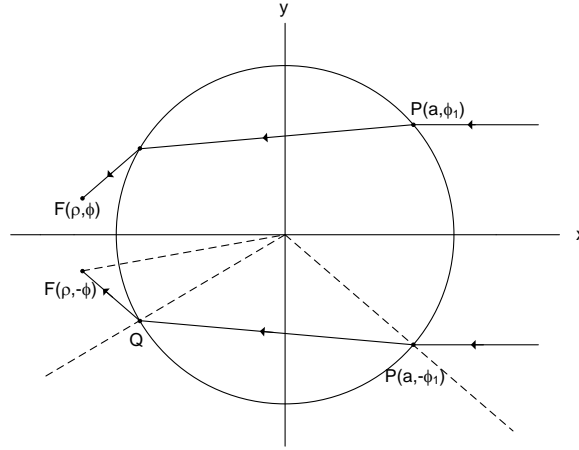


Figure 51 The physical picture for the second term of the Debye series in the geometrically lit region for the double positive cylinder

The steepest descent equation is matched to the physical picture by the relation in (138). The next step is to compare the exponential contributions to the scattered field.

When the saddle point solution is put into the exponential part of the Debye asymptotic expansion of the integrand, the following exponential part is obtained:

$$\exp \left\{ jk_0 \left[2a(n^2 - \sin^2 \phi_1)^{\frac{1}{2}} + (\rho^2 - a^2 \sin^2 \phi_1)^{\frac{1}{2}} - 2a \cos(\phi_1) \right] \right\} e^{-j\frac{\pi}{4}} \tag{139}$$

Due to the high frequency operation, the plane wave incident on the cylinder can be represented by rays. The plane wave incident on the point $P(a, -\phi_1)$ is represented by a ray incident at the point $P(a, -\phi_1)$. The ray incident on the

point $P(a, -\phi_1)$ is denoted by $e^{-jk_0 a \cos(\phi_1)}$. Then, the ray is transmitted into the cylinder and propagates for a path length of $|PQ|$. This propagation is reflected as a multiplication by $e^{(jn k_0 |PQ|)}$. Hence, the exponential dependence of the ray at the point Q is given by $e^{-jk_0 a \cos(\phi_1)} \times e^{(jn k_0 |PQ|)}$. Then, the ray is transmitted out of the cylinder and propagates to the field point $F(\rho, -\phi)$. During this propagation, it takes a path of length $|QF|$. The exponential dependence of the ray at the field point is given by $e^{-jk_0 a \cos(\phi_1)} \times e^{(jn k_0 |PQ|)} \times e^{(j k_0 |QF|)}$. After the calculations for the path lengths, it can be shown that the exponential dependence of the ray at the field point is equal to

$$\exp \left\{ jk_0 \left[2a(n^2 - \sin^2 \phi_1)^{\frac{1}{2}} + (\rho^2 - a^2 \sin^2 \phi_1)^{\frac{1}{2}} - 2a \cos(\phi_1) \right] \right\} \quad (140)$$

Hence, in terms of the exponential dependence, it is proven that the second term of the Debye series physically represents the ray which is transmitted into the cylinder and is transmitted outside of the cylinder. The verification for the amplitude will be carried out numerically in a separate chapter.

The first integral in (130) represents another ray. This ray is incident on the point $P(a, \phi_1)$ and contributes to the scattered field at the point $F(\rho, \phi)$. Due to the symmetry of the problem geometry, the contribution to the scattered field at the point $F(\rho, -\phi)$ is the same as the one at the point $F(\rho, \phi)$. Hence, taking the $\frac{1}{2}$ coefficient in front of the integral in (130), it is proven in terms of the exponential dependence that the integral in (130) represents the contribution of the ray incident on the point $P(a, -\phi_1)(P(a, \phi_1))$ to the scattered field at the point $F(\rho, \phi)(F(\rho, -\phi))$.

The contribution of the second term of the Debye series to the scattered field in the geometrical shadow region of the cylinder is calculated using the residue series. In order to express the integral in (130) in terms of a residue series, the integrand must be checked for vanishing in the upper half of the complex v -plane as $|v| \rightarrow \infty$. After making the asymptotic expansion of the integrand as

$|v| \rightarrow \infty$ in the upper half of the complex v -plane, it is determined that the integrand vanishes for the ϕ values of the geometrical shadow region.

The integral in the equation (130) is modified as follows after some mathematical operations:

$$E_s^{second\ term} = \left[-\frac{8}{(\pi\beta)^2} \right] \int_{-\infty+j\epsilon}^{\infty+j\epsilon} \frac{H_v^{(1)}(k_0\rho) \left[e^{jv(\phi+\frac{3\pi}{2})} + e^{jv(-\phi+\frac{3\pi}{2})} \right]}{\left[H_v^{(1)}(\beta)H_v^{(2)}(\alpha) \right]^2 \left([1\ \beta] - \frac{n}{\mu_r} [2\ \alpha] \right)^2} dv \quad (141)$$

The poles of the integrand in the equation (141) are the same as the poles of the integrand of the first term of the Debye series. However, the poles of the second term of the Debye series are second order poles. The following definition is made for making the residue calculations easier:

$$f(v) \triangleq \frac{\left. \begin{aligned} & [1\ \beta] - \frac{n}{\mu_r} [2\ \alpha] \triangleq g(v)(v - v_l) \\ & H_v^{(1)}(k_0\rho) \left[e^{jv(\phi+\frac{3\pi}{2})} + e^{jv(-\phi+\frac{3\pi}{2})} \right] \end{aligned} \right\}}{\left[H_v^{(1)}(\beta)H_v^{(2)}(\alpha) \right]^2} \quad (142)$$

where v_l is the l^{th} pole of the integrand in the equation (141). Then, the residue series representation of the integral in the equation (141) for the geometrical shadow region of the second term of the Debye series is given by the following:

$$E_s^{second\ term} = \left[-\frac{16\pi j}{(\pi\beta)^2} \right] \sum_l Res \left\{ \frac{[f(v)/[g(v)]^2]}{(v - v_l)^2} \right\} \Big|_{v \rightarrow v_l} \quad (143)$$

The scattered field due to the second term of the Debye series is expressed as follows when the residue operation in the equation (143) is carried out:

$$E_s^{second\ term} = \left[-\frac{16\pi j}{(\pi\beta)^2} \right] \sum_l \left\{ \frac{f'(v)}{[g(v)]^2} - \frac{2f(v)g'(v)}{[g(v)]^3} \right\} \Big|_{v \rightarrow v_l} \quad (144)$$

If the equation (144) is explicitly written, then it can be seen that

$$\frac{H_v^{(1)}(k_0\rho)}{[H_v^{(2)}(\alpha)]^2} \left[e^{jv(\phi+\frac{3\pi}{2})} + e^{jv(-\phi+\frac{3\pi}{2})} \right] \quad (145)$$

can be fixed as a common factor. The Hankel functions in the common factor are expanded into their Debye asymptotic forms. The purpose of applying the Debye asymptotic expansions is to determine the convergence region of the residue series and relate it to the physical picture of the creeping waves traveling on the cylinder from the geometrically lit region to the geometrical shadow region. Then, the exponential terms in the common factor takes the following form:

$$e^{\left\{ j \left[((k_0\rho)^2 - v^2)^{\frac{1}{2}} + 2(\alpha^2 - v^2)^{\frac{1}{2}} \right] \right\}} e^{\left\{ j \left[-v \cos^{-1}\left(\frac{v}{k_0\rho}\right) - 2v \cos^{-1}\left(\frac{v}{\alpha}\right) \right] \right\}} \left[e^{jv(\phi+\frac{3\pi}{2})} + e^{jv(-\phi+\frac{3\pi}{2})} \right] \quad (146)$$

The approximation of the poles to β in the first exponential factor in (146) is enabled by their proximity to β . In addition, the following equality and the definitions

$$\left. \begin{aligned} \cos^{-1}(t) &= \frac{\pi}{2} - \sin^{-1}(t) \\ \theta_0 &= \cos^{-1}\left(\frac{\alpha}{\rho}\right) \\ \theta_c &= \sin^{-1}\left(\frac{1}{n}\right) \end{aligned} \right\} \quad (147)$$

are used in the equation (146) to obtain the common factor in the following form:

$$e^{\left\{ j \left[((k_0\rho)^2 - \beta^2)^{\frac{1}{2}} + 2(\alpha^2 - \beta^2)^{\frac{1}{2}} \right] \right\}} e^{[jv(-\theta_0+2\theta_c-\pi)]} e^{jv(\phi+\frac{3\pi}{2})} + e^{\left\{ j \left[((k_0\rho)^2 - \beta^2)^{\frac{1}{2}} + 2(\alpha^2 - \beta^2)^{\frac{1}{2}} \right] \right\}} e^{[jv(-\theta_0+2\theta_c-\pi)]} e^{jv(-\phi+\frac{3\pi}{2})} \quad (148)$$

The convergence of the residue series depends on the convergence of the exponentials in the expression (148). The fact that the imaginary parts of the poles are positive implies the following conditions for the convergence of the residue series:

$$\left. \begin{aligned} -\theta_0 + 2\theta_c + \phi + \frac{\pi}{2} &> 0 \\ -\theta_0 + 2\theta_c - \phi + \frac{\pi}{2} &> 0 \end{aligned} \right\} \quad (149)$$

The intersection of the ranges in (149) yields the following range of convergence of the residue series:

$$\theta_0 - 2\theta_c - \frac{\pi}{2} < \phi < -\theta_0 + 2\theta_c + \frac{\pi}{2} \quad (150)$$

It can be seen in the Figure 50 that the above range is actually the geometrical shadow of the cylinder for the second term of the Debye series.

The residue series representation has a physical interpretation which is obtained using the ray interpretation of the incident high frequency plane wave. The Figure 52 is used to display the physical picture. The high frequency plane wave incident on the point $P \left(a, \frac{\pi}{2} \right)$ is denoted by the exponential dependence $e^{-jk_0 a \cos \left(\frac{\pi}{2} \right)}$. Then, it is critically refracted into the cylinder and takes a path of length

$$|PQ| = 2a \cos(\theta_c) = 2a \frac{(n^2 - 1)^{\frac{1}{2}}}{n} \quad (151)$$

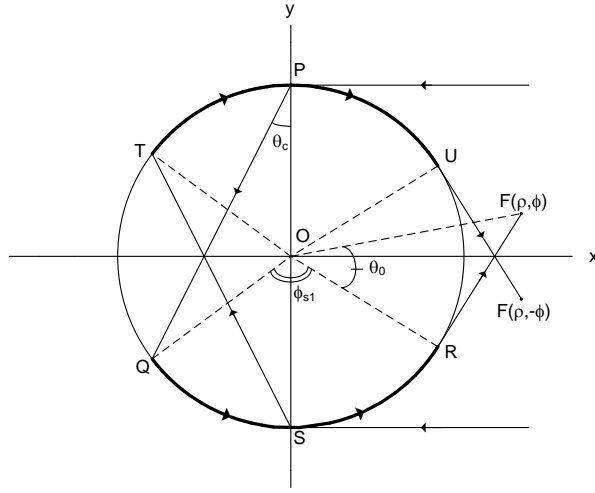


Figure 52 The physical picture corresponding to the residue series for the second term of the Debye series in the case of a double positive cylinder

According to the geometric optics, the propagation along this path is mathematically reflected to the ray as a multiplication by $e^{jn k_0 |PQ|}$. Then, the ray is denoted by $e^{-jk_0 a \cos(\frac{\pi}{2})} \times e^{j2\beta(n^2-1)^{\frac{1}{2}}}$ at the point $Q(a, -\frac{\pi}{2} - 2\theta_c)$. At the point $Q(a, -\frac{\pi}{2} - 2\theta_c)$, the ray is transmitted to the outside of the cylinder, but it does not leave the cylinder surface and creeps on the surface of the cylinder into the geometrical shadow region for the second term of the Debye series. The creeping ray leaves the surface of the cylinder at the point $R(a, -\frac{\pi}{2} - 2\theta_c + \phi_{s1})$. At this point, the creeping wave has the exponential dependence of $e^{-jk_0 a \cos(\frac{\pi}{2})} \times e^{j2\beta(n^2-1)^{\frac{1}{2}}} \times e^{j\beta \phi_{s1}}$. The ray propagates to the field point $F(\rho, \phi)$ after taking the path $|RF|$. The ray finally arrives at this point with an exponential dependence of $e^{-jk_0 a \cos(\frac{\pi}{2})} \times e^{j2\beta(n^2-1)^{\frac{1}{2}}} \times e^{j\beta \phi_{s1}} \times e^{jk_0 |RF|}$. The length of the path $|RF|$ is given by

$$|RF| = (\rho^2 - a^2)^{\frac{1}{2}} \quad (152)$$

Then, the overall exponential dependence of the ray at the field point is given by the following expression:

$$e^{-jk_0 a \cos\left(\frac{\pi}{2}\right)} \times e^{j2\beta(n^2-1)^{\frac{1}{2}}} \times e^{j\beta\phi_{s1}} \times e^{j[(k_0\rho)^2-\beta^2]^{\frac{1}{2}}} \quad (153)$$

The angle ϕ_{s1} corresponding to the arc travelled by the creeping wave on the cylinder satisfies the following relation:

$$\phi_{s1} = \phi + \frac{\pi}{2} + 2\theta_c - \theta_0 \quad (154)$$

Using the relation in the equation (154), the exponential dependence of the ray at the field point can be written as follows:

$$e^{-jk_0 a \cos\left(\frac{\pi}{2}\right)} \times e^{j2\beta(n^2-1)^{\frac{1}{2}}} \times e^{j\beta\left(\phi + \frac{\pi}{2} + 2\theta_c - \theta_0\right)} \times e^{j[(k_0\rho)^2-\beta^2]^{\frac{1}{2}}} \quad (155)$$

Since the real part of the first few poles of the integrand in (141) are close to β , the propagating part of the first part of the common factor in (148) becomes equal to the expression in (155) if the real part of the poles are approximated with β . In this way, the residue series is matched with the physical picture in the Figure 52.

The second exponential term in the common factor in (148) can be related to the other ray in the physical picture shown in the Figure 52 by using exactly the same reasoning.

The mathematical calculations and the physical interpretations have been made for an infinite length cylinder made of a double positive material. A material of positive relative permittivity and positive permeability is meant by means of the double positive medium. The analysis for a double negative is to be carried out and there will be some differences in the analysis for the double negative medium.

The integral to be calculated is again the one in the equation (130). However, the negativity of the refractive index which shows itself in the following relation causes the differences in the calculations:

$$\alpha = -|n|\beta \quad (156)$$

The Debye asymptotic approximation is used in the integrand of the second integral in (130). In treating the Hankel functions with the argument α , the following analytical continuity relations are used from [29]:

$$\left. \begin{aligned} H_v^{(1)}(ze^{j\pi}) &= -e^{-jv\pi} H_v^{(2)}(z) \\ H_v^{(2)}(ze^{-j\pi}) &= -e^{jv\pi} H_v^{(1)}(z) \end{aligned} \right\} \quad (157)$$

The application of the Debye asymptotic approximation with the analytical continuation relations is followed by taking the first derivative of the exponent of the resulting integrand with respect to v . The obtained derivative expression is equated to zero to find the possible saddle point \bar{v} :

$$2 \cos^{-1}\left(\frac{\bar{v}}{\beta}\right) + 2 \cos^{-1}\left(\frac{\bar{v}}{|n|\beta}\right) - \cos^{-1}\left(\frac{\bar{v}}{k_0\rho}\right) - \phi - \frac{\pi}{2} = 0 \quad (158)$$

The physical picture shown in the Figure 53 for the double negative cylinder differs from that of the double positive cylinder in the negative refraction. From the Figure 53, the following relation can be derived:

$$\phi = \pi - 2\theta_1 - 2 \sin^{-1}\left(\frac{1}{|n|} \sin \theta_1\right) + \sin^{-1}\left(\frac{a}{\rho} \sin \theta_1\right) \quad (159)$$

The following definition and the relation is used in the equation (158):

$$\left. \begin{aligned} \bar{v} &= \beta \cos w \\ \sin^{-1} x &= \frac{\pi}{2} - \cos^{-1} x \end{aligned} \right\} \quad (160)$$

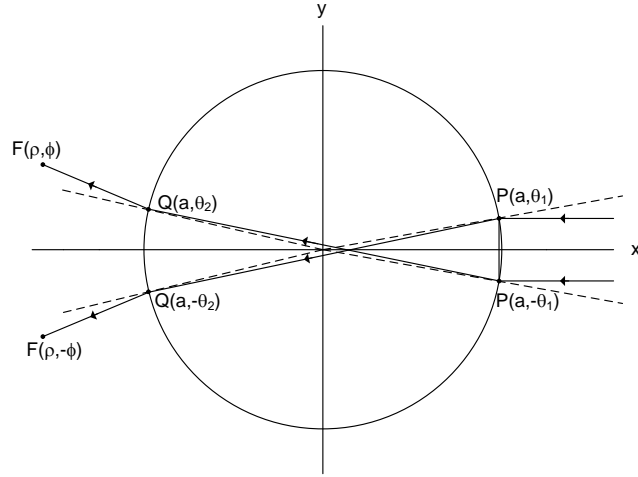


Figure 53 The physical picture in the geometrically lit region of the DNG cylinder corresponding to the second term of the Debye series

After using the definitions in (160), it can be seen that the equation (158) and the equation (159) become the same when the solution for the saddle point is expressed as follows:

$$w = \frac{\pi}{2} - \theta_1 \quad (161)$$

In this way, the integral under investigation is partly related to a physical picture. This connection is to be made stronger using the SDM evaluation of the integral and the geometrical optics. It is going to be proven that the exponential part of the SDM result of the integral is the same as the exponential part of the ray obtained using the geometrical optics at the field point.

The SDM evaluation of the integral produces the following exponential expression:

$$\exp \left\{ jk_0 \left[(\rho^2 - a^2 \sin^2 \theta_1)^{\frac{1}{2}} - 2a(|n|^2 - \sin^2 \theta_1)^{\frac{1}{2}} - 2a \cos \theta_1 \right] \right\} \quad (162)$$

The high frequency plane wave incident on the point $P(a, -\theta_1)$ can be denoted by a ray of exponential dependence $e^{-jk_0 a \cos \theta_1}$. The incident ray is negatively

refracted into the cylinder and takes the path of length $|PQ|$ to arrive at the point $Q(a, \theta_2)$. The exponential dependence of the ray at the point $Q(a, \theta_2)$ is given by $e^{-jk_0 a \cos \theta_1} \times e^{jk_0 |n| |PQ|}$. The ray is again negatively refracted at the point $Q(a, \theta_2)$ to the outside of the cylinder and propagates to the field point $F(\rho, \phi)$ after taking the path of length $|QF|$. The exponential dependence of the ray at the field point is given by the following $e^{-jk_0 a \cos \theta_1} \times e^{jk_0 |n| |PQ|} \times e^{jk_0 |QF|}$. If the required mathematical operations are carried out to determine the path lengths, then it can be shown that the exponential dependence of the ray at the field point is given by the following expression:

$$\exp \left\{ jk_0 \left[(\rho^2 - a^2 \sin^2 \theta_1)^{\frac{1}{2}} - 2a(|n|^2 - \sin^2 \theta_1)^{\frac{1}{2}} - 2a \cos \theta_1 \right] \right\} \quad (163)$$

This exponential dependence is the same as the one in the equation (162). Hence, it is proven that the geometrical optics calculation of the exponential part of the integral and the SDM solution for the exponential part of the integral yield the same results. The physical picture for the integral has been proven to be right in terms of the exponential part of the field at the field point. The verification in terms of the amplitude will be numerically carried out in a later chapter.

The first part of the integral in the equation (130) has a similar interpretation. It represents the scattered field formed at the field point by the ray incident at the point $P(a, \theta_1)$. This ray is negatively refracted into the cylinder and propagates to the point $Q(a, -\theta_2)$. At that point, it is negatively refracted again and propagates to the field point $F(\rho, -\phi)$. Due to the symmetry of the problem geometry, the scattered field at the point $F(\rho, -\phi)$ is the same as the one at the point $F(\rho, \phi)$. Hence, in terms of the exponential dependence, the overall integral in (130) is equal to the contribution of the ray incident on the point $P(a, \theta_1)$ (or $P(a, -\theta_1)$) to the scattered field at the point $F(\rho, -\phi)$ (or $F(\rho, \phi)$). The verification in terms of the magnitude will be numerically carried out in a later chapter.

For the case of the double negative cylinder, the contribution of the second term of the Debye series to the scattered field at the geometrical shadow region corresponding to the second term of the Debye series is calculated in a similar way to the double positive case. The only main difference is the critical negative refraction.

The analysis for the double negative cylinder goes parallel with the one for the double positive cylinder. The integral in the equation (130) takes the following form after some mathematical operations:

$$E_s^{second \ term} = \left[-\frac{8}{(\pi\beta)^2} \right] \int_{-\infty+j\epsilon}^{\infty+j\epsilon} \frac{H_v^{(1)}(k_0\rho) \left[e^{jv(\phi+\frac{3\pi}{2})} + e^{jv(-\phi+\frac{3\pi}{2})} \right]}{\left[H_v^{(1)}(\beta)H_v^{(2)}(\alpha) \right]^2 \left([1\ \beta] + \frac{n}{\mu_r} [1\ |n|\beta] \right)^2} dv \quad (164)$$

where

$$\alpha = -|n|\beta \quad (165)$$

The integral in the equation (164) must be checked for vanishing as $|v| \rightarrow \infty$ in the upper half of the complex v -plane. The examination for vanishing is carried out by making the asymptotic expansion of the integrand as $|v| \rightarrow \infty$ in the upper half of the complex v -plane. The integrand vanishes in the geometrical shadow region corresponding to the second term of the Debye series. In this region, the integral in the equation (164) can be written as a residue series:

$$E_s^{second \ term} = \left[-\frac{16\pi j}{(\pi\beta)^2} \right] \sum_l Res \left\{ \frac{[f(v)/[g(v)]^2]}{(v-v_l)^2} \right\} \Big|_{v \rightarrow v_l} \quad (166)$$

where

$$f(v) \triangleq \frac{\left. \begin{aligned} & [1\ \beta] + \frac{n}{\mu_r} [1\ \alpha] \triangleq g(v)(v-v_l) \\ & H_v^{(1)}(k_0\rho) \left[e^{jv(\phi-\frac{\pi}{2})} + e^{jv(-\phi-\frac{\pi}{2})} \right] \end{aligned} \right\}}{\left[H_v^{(1)}(\beta)H_v^{(1)}(|n|\beta) \right]^2} \quad (167)$$

After the residue series is written explicitly, it can be seen that

$$\frac{H_v^{(1)}(k_0\rho)}{\left[H_v^{(1)}(|n|\beta)\right]^2} \left[e^{jv(\phi - \frac{\pi}{2})} + e^{jv(-\phi - \frac{\pi}{2})} \right] \quad (168)$$

can be fixed as a common factor. A more detailed determination of the convergence region of the residue series is allowed by the application of the Debye asymptotic expansion to the common factor. The exponential part of the common factor after the Debye asymptotic expansion is given as follows:

$$e^{\left\{ j \left[((k_0\rho)^2 - v^2)^{\frac{1}{2}} - 2(|n|^2\beta^2 - v^2)^{\frac{1}{2}} \right] \right\}} e^{\left\{ j \left[-v \cos^{-1}\left(\frac{v}{k_0\rho}\right) + 2v \cos^{-1}\left(\frac{v}{|n|\beta}\right) \right] \right\}} \left[e^{jv(\phi - \frac{\pi}{2})} + e^{jv(-\phi - \frac{\pi}{2})} \right] \quad (169)$$

Due to the closeness of the poles in the equation (166) to β , they are approximated by β . It is possible to write the common factor in the following more compact form using the definitions in (147) with n replaced with $|n|$:

$$\begin{aligned} & e^{\left\{ j \left[((k_0\rho)^2 - \beta^2)^{\frac{1}{2}} - 2\beta(|n|^2 - 1)^{\frac{1}{2}} \right] \right\}} e^{jv(-\theta_0 - 2\theta_c + \phi + \frac{\pi}{2})} \\ & + \\ & e^{\left\{ j \left[((k_0\rho)^2 - \beta^2)^{\frac{1}{2}} - 2\beta(|n|^2 - 1)^{\frac{1}{2}} \right] \right\}} e^{jv(-\theta_0 - 2\theta_c - \phi + \frac{\pi}{2})} \end{aligned} \quad (170)$$

Since the imaginary parts of the poles are positive, the following conditions are required for the convergence of the common factor:

$$\left. \begin{aligned} -\theta_0 - 2\theta_c + \phi + \frac{\pi}{2} &> 0 \\ -\theta_0 - 2\theta_c - \phi + \frac{\pi}{2} &> 0 \end{aligned} \right\} \quad (171)$$

The conditions in the equation (171) require the following range of ϕ for the convergence of the residue series:

$$\theta_0 + 2\theta_c - \frac{\pi}{2} < \phi < -\theta_0 - 2\theta_c + \frac{\pi}{2} \quad (172)$$

The geometrical shadow region of the double negative cylinder for a specific ρ coordinate corresponding to the second term of the Debye series is shown in the Figure 54. The comparison made between the geometrical shadow region of the double negative cylinder corresponding to the second term of the Debye series and that of the double positive cylinder corresponding to the second term of the Debye series reveals that the double negative cylinder has a quite smaller geometric shadow region for $|n| > \sqrt{2}$.

The residue series solution is expected to be related with the physical picture shown in the Figure 55. The high frequency plane wave which is incident on the cylinder is denoted by the ray hitting the point $P\left(a, \frac{\pi}{2}\right)$. The ray has the exponential dependence of $e^{-jk_0 a \cos \frac{\pi}{2}}$. After hitting the point $P\left(a, \frac{\pi}{2}\right)$, the ray is negatively refracted into the double negative cylinder and propagates to the point $Q\left(a, -\frac{\pi}{2} + 2\theta_c\right)$. The length of the path taken by the ray is given by the following:

$$|PQ| = 2a \frac{(|n|^2 - 1)^{\frac{1}{2}}}{|n|} \quad (173)$$

The propagation of the ray to the point $Q\left(a, -\frac{\pi}{2} + 2\theta_c\right)$ is reflected as a multiplication by the exponential factor $e^{jk_0 |n| |PQ|}$. The exponential dependence of the ray at the point $Q\left(a, -\frac{\pi}{2} + 2\theta_c\right)$ is given by $e^{-jk_0 a \cos \frac{\pi}{2}} \times e^{j2\beta(|n|^2 - 1)^{\frac{1}{2}}}$. Then, the ray is transmitted to the outside of the cylinder and creeps on the surface of the cylinder into the geometrical shadow region corresponding to the second term of the Debye series. The creeping wave travels to the point $R\left(a, -\frac{\pi}{2} + 2\theta_c + \phi_{s1}\right)$. At this point, the creeping wave has the exponential dependence of $e^{-jk_0 a \cos \frac{\pi}{2}} \times e^{j2\beta(|n|^2 - 1)^{\frac{1}{2}}} \times e^{j\beta \phi_{s1}}$. Then,

the ray leaves the cylinder at this point and propagates to the field point $F(\rho, \phi)$ by taking the path of length

$$|RF| = (\rho^2 - a^2)^{\frac{1}{2}} \quad (174)$$

The exponential dependence of the ray at the field point is given by

$$e^{-jk_0 a \cos \frac{\pi}{2}} \times e^{j2\beta(|n|^2-1)^{\frac{1}{2}}} \times e^{j\beta \phi_{s1}} \times e^{jk_0(\rho^2-a^2)^{\frac{1}{2}}} \quad (175)$$

The angle ϕ_{s1} corresponding to the arc travelled by the creeping wave on the cylinder satisfies the following relation:

$$\phi_{s1} = \phi + \frac{\pi}{2} - 2\theta_c - \theta_0 \quad (176)$$

The exponential dependence of the ray at the field point given by (175) becomes equal to the first exponential term given in the equation (170) if the relation in (176) is put into the expression in (175).

The second exponential term in the expression (170) has a similar interpretation and it corresponds to the second ray in the Figure 55.

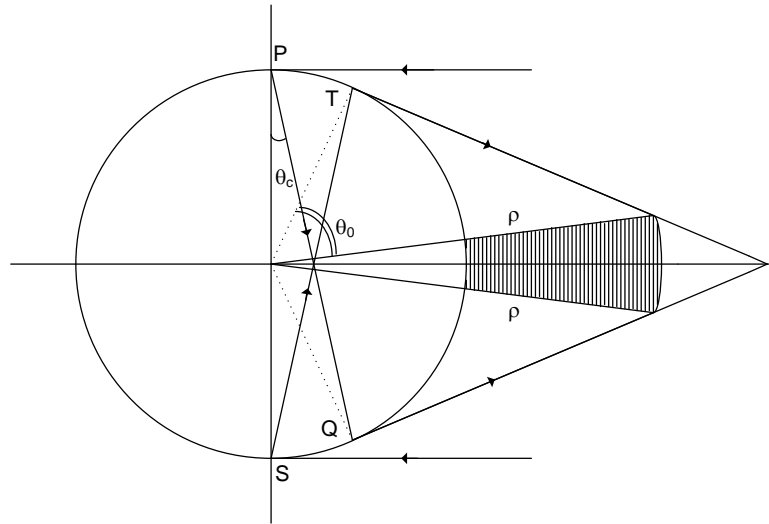


Figure 54 The geometrical shadow region of the double negative cylinder for a specific ρ coordinate corresponding to the second term of the Debye series is the shaded region for $n > \sqrt{2}$.

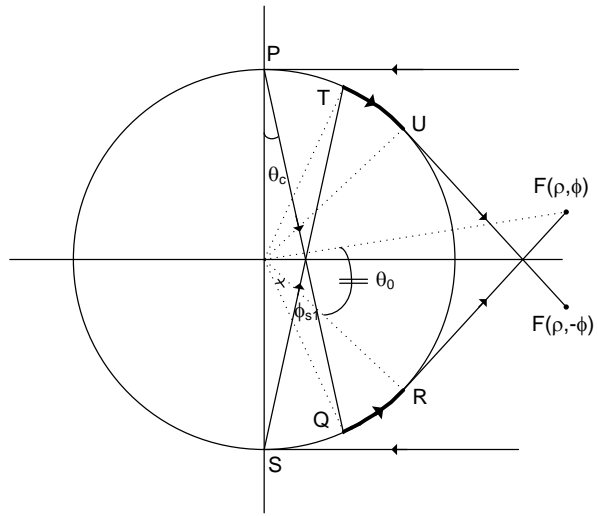


Figure 55 The physical picture in the geometrical shadow region of the DNG cylinder corresponding to the second term of the Debye series

CHAPTER 5

NUMERICAL RESULTS

In this chapter, the series results of the first and the second terms of the Debye expansion are tabulated along with the corresponding residue series results and the corresponding steepest descent method (SDM) results. The series results and the results obtained using the physical insight into the problem, i.e. the residue series and the SDM calculations are compared to each other.

Throughout the tabulation of the results, the following definition is valid for the percentage errors in the results:

$$\text{percentage error in the result} \triangleq \frac{|\text{result} - \text{Debye series result}|}{\text{Debye series result}} \times 100$$

5.1 The Geometrical Shadow Region of the Double Positive Cylinder Corresponding to the First Term of the Debye Series

The following series expression represents the contribution of the first term of the Debye series to the field in the geometrical shadow region corresponding to the first term of the Debye series for the double positive cylinder:

$$\sum_{l=-\infty}^{\infty} \frac{1}{2} j^{-l} \left[R_{22}(l) \frac{H_l^{(2)}(\beta)}{H_l^{(1)}(\beta)} H_l^{(1)}(k_0 \rho) + H_l^{(2)}(k_0 \rho) \right] e^{-jl\phi} \quad (177)$$

Mathematica is used in the computation of the series. Calculation of the integral corresponding to the series is carried out using the residue series. The results shown in the tables are obtained using only three terms of the residue series corresponding to first three poles of the integrand. There is an obvious computational advantage. The Debye expansion for $H_v^{(1)}(k_0 \rho)$ in the residue series is not applied for getting the residue series results.

First, the series results and the residue series results are tabulated with respect to varying refracting indices. The following parameters are used in the calculations:

$$\beta = 50\pi$$

$$\mu_r = 1$$

$$k_0\rho = 3\left(\beta + \beta^{\frac{1}{3}}\right)$$

Table 1 The series results for varying refractive indices, the geometrical shadow region of the double positive cylinder corresponding to the first term of the Debye series

n	161.2°	164.96°	168.72°
1.5	-0.379717+0.171978j	0.0689067+0.14581j	0.0573083-0.0486615j
2	-0.374175+0.174276j	0.0686173+0.141592j	0.0540335-0.047026j
3	-0.370288+0.175848j	0.0683746+0.13867j	0.0518701-0.0458813j
4	-0.368638+0.176509j	0.0682645+0.137437j	0.0509806-0.0453984j
5	-0.367703+0.176882j	0.0682007+0.136742j	0.0504841-0.0451262j
n	172.48°	176.24°	180°
1.5	-0.0356742-0.0133717j	-0.00611043+0.015343j	0.0227899-0.00727888j
2	-0.03332-0.0124896j	-0.00529878+0.0143123j	0.0203606-0.00672293j
3	-0.0317692-0.0119097j	-0.00479522+0.0136158j	0.0188199-0.00633763j
4	-0.0311339-0.0116706j	-0.00459544+0.0133272j	0.0182019-0.00617759j
5	-0.03078-0.0115369j	-0.0044857+0.0131658j	0.0178609-0.00608818j

Table 2 The residue series results for varying refractive indices, the geometrical shadow region of the double positive cylinder corresponding to the first term of the Debye series

n	161.2°	164.96°	168.72°
1.5	-0.299323+0.0742719j	0.0632328+0.127644j	0.054299-0.0489249j
2	-0.297048+0.0759453j	0.0626646+0.124136j	0.0511709-0.0471958j
3	-0.29544+0.0772511j	0.0622701+0.121708j	0.0491097-0.0459967j
4	-0.294751+0.0778292j	0.0621032+0.120682j	0.048263-0.0454929j
5	-0.294359+0.0781613j	0.0620089+0.120103j	0.0477904-0.0452092j
n	172.48°	176.24°	180°
1.5	-0.0358715-0.0128958j	-0.00603859+0.0153968j	0.0228173-0.00729995j
2	-0.0334897-0.0120419j	-0.00523181+0.0143592j	0.0203843-0.00674257j
3	-0.0319224-0.0114819j	-0.00473178+0.0136585j	0.0188413-0.00635612j
4	-0.0312807-0.0112512j	-0.00453347+0.0133683j	0.0182225-0.0061956j

Table 2 The residue series results for varying refractive indices, the geometrical shadow region of the double positive cylinder corresponding to the first term of the Debye series (Cont'd)

n	172.48°	176.24°	180°
5	-0.0309233-0.0111222j	-0.00442456+0.0132059j	0.017881-0.00610593j

Table 3 The percentage error in the magnitude of the residue series results for varying refractive indices, the geometrical shadow region of the double positive cylinder corresponding to the first term of the Debye series

n	161.2°	164.96°	168.72°
1.5	26.01601741	11.67237896	2.782388157
2	25.720693	11.62197489	2.818472675
3	25.50459352	11.57605097	2.83591935
4	25.41208932	11.55565389	2.842028832
5	25.35953829	11.5441504	2.845536165
n	172.48°	176.24°	180°
1.5	0.055627587	0.143074541	0.135906736
2	0.014011419	0.137176753	0.133691132
3	0.010832329	0.134329729	0.131857541
4	0.020396943	0.133624874	0.13161273
5	0.025669261	0.132428704	0.131185537

Second, the series results and the residue series results are tabulated with respect to varying operating frequencies. The following parameters are used in the calculations:

$$\begin{aligned}
 n &= 3 \\
 \mu_r &= 1 \\
 k_0\rho &= 3\left(\beta + \beta^{\frac{1}{3}}\right)
 \end{aligned}$$

Table 4 The tabulation of the results for $\beta = 10\pi$, the geometrical shadow region of the double positive cylinder corresponding to the first term of the Debye series

	162.368°	165.894°	169.421°
Series	-0.0609014-0.376342j	0.215358+0.117345j	-0.166967+0.0615577j
Residue series without the Debye approximation	-0.00341465-0.33116j	0.188239+0.114018j	-0.157882+0.0570327j
The percentage error in the magnitude of the residue series	13.13096976	10.26510147	5.667667625
	172.947°	176.474°	180°
Series	0.0406401-0.0841446j	0.0608596+0.0172329j	-0.0967259+0.0231716j
Residue series without the Debye approximation	0.0389236-0.0808288j	0.0604285+0.0157956j	-0.0959294+0.0239236j
The percentage error in the magnitude of the residue series	3.994074053	1.254590306	0.598355753

Table 5 The tabulation of the results for $\beta = 20\pi$, the geometrical shadow region of the double positive cylinder corresponding to the first term of the Debye series

	161.73°	165.384°	169.038°
Series	-0.0752267+0.391876j	0.206762-0.0021143j	-0.0448998-0.115676j
Residue series without the Debye approximation	-0.112459+0.306594j	0.182617+0.00356314j	-0.044009-0.109096j
The percentage error in the magnitude of the residue series	18.15967649	11.66548543	5.195041326
	172.692°	176.346°	180°
Series	-0.0355867+0.0544876j	0.0271474+0.0224718j	-0.011326-0.052127j
Residue series without the Debye approximation	-0.0337649+0.0543157j	0.0271086+0.0220066j	-0.0116163-0.052098j
The percentage error in the magnitude of the residue series	1.727282997	0.922010638	0.063898433

Table 6 The tabulation of the results for $\beta = 30\pi$, the geometrical shadow region of the double positive cylinder corresponding to the first term of the Debye series

	161.459°	165.167°	168.876°
Series	-0.0838648-0.394836j	0.0332628-0.18627j	0.035451-0.090705j
Residue series without the Debye approximation	-0.0106799-0.317969j	0.0311276-0.164171j	0.03196-0.0875153j
The percentage error in the magnitude of the residue series	21.1810355	11.69067462	4.331398088
	172.584°	176.292°	180°
Series	0.0268974-0.0507225j	0.0214958-0.0339658j	0.0197858-0.02992684j
Residue series without the Debye approximation	0.0258559-0.050645j	0.0212935-0.0341051j	0.0197403-0.0293724j
The percentage error in the magnitude of the residue series	0.957158587	0.025557729	1.356275329

Table 7 The tabulation of the results for $\beta = 40\pi$, the geometrical shadow region of the double positive cylinder corresponding to the first term of the Debye series

	161.303°	165.043°	168.782°
Series	0.341557+0.218905j	-0.170124+0.00616087j	0.0536875-0.0603431j
Residue series without the Debye approximation	0.225856+0.211528j	-0.150179+0.00620783j	0.0502209-0.0595802j
The percentage error in the magnitude of the residue series	23.72337052	11.70629326	3.524109725
	172.521°	176.261°	180°
Series	0.00529038+0.0366238j	-0.0212161-0.00136576j	0.0221089-0.0132127j
Residue series without the Debye approximation	0.00587064+0.0362938j	-0.0213027-0.00126135j	0.0221281-0.0132626j
The percentage error in the magnitude of the residue series	0.644251304	0.376274443	0.163458275

Table 8 The tabulation of the results for $\beta = 50\pi$, the geometrical shadow region of the double positive cylinder corresponding to the first term of the Debye series

	161.2°	164.96°	168.72°
Series	-0.370288+0.175848j	0.0683746+0.13867j	0.0518701-0.0458813j
Residue series without the Debye approximation	-0.29544+0.0772511j	0.0622701+0.121708j	0.0491097-0.0459967j
The percentage error in the magnitude of the residue series	25.50459352	11.57605097	2.83591935
	172.48°	176.24°	180°
Series	-0.0317692-0.0119097j	-0.00479522+0.0136158j	0.0188199-0.00633763j
Residue series without the Debye approximation	-0.0319224-0.0114819j	-0.00473178+0.0136585j	0.0188413-0.00635612j
The percentage error in the magnitude of the residue series	0.010832329	0.134329729	0.131857541

5.2 The Geometrically Lit Region of the Double Positive Cylinder Corresponding to the First Term of the Debye Series

The contribution of the first term of the Debye series to the corresponding geometrically lit region is denoted by the following series expression for the double positive cylinder:

$$\sum_{l=-\infty}^{\infty} \frac{1}{2} j^{-l} \left[R_{22}(l) \frac{H_l^{(2)}(\beta)}{H_l^{(1)}(\beta)} - 1 \right] H_l^{(1)}(k_0 \rho) e^{-jl\phi} \quad (178)$$

The integral corresponding to the series is calculated using the steepest descent method. However, only the upper half of the steepest descent path is traversed since the integrand blows up in the lower half of the v -plane. This causes a factor of $\frac{1}{2}$ to be put in front of the steepest descent result.

First, the series results and the SDM results are tabulated with respect to varying refractive indices. The following parameters are used in the calculations:

$$\beta = 50\pi$$

$$\mu_r = 1$$

$$k_0\rho = 3\left(\beta + \beta^{\frac{1}{3}}\right)$$

Table 9 The series results with respect to varying n, the geometrically lit region of the double positive cylinder corresponding to the first term of the Debye series

n	0°	5°	10°
1.5	0.077826+0.04033j	0.0589269+0.0650204j	-0.0286799+0.0832317j
2	0.129668+0.0672989j	0.0980985+0.108381j	-0.0478029+0.138439j
3	0.194438+0.101072j	0.146979+0.162592j	-0.0717077+0.207239j
4	0.233288+0.12136j	0.176273+0.195122j	-0.0860507+0.248435j
5	0.259183+0.134893j	0.195791+0.21681j	-0.0956127+0.275872j
n	15°	20°	
1.5	-0.0760301-0.0453139j	0.0884806-0.0111156j	
2	-0.126153-0.0752999j	0.146415-0.0182925j	
3	-0.188391-0.112615j	0.218063-0.0270983j	
4	-0.225569-0.134936j	0.260747-0.0323174j	
5	-0.250299-0.149795j	0.289102-0.0357756j	

Table 10 The SDM results with respect to varying n, the geometrically lit region of the double positive cylinder corresponding to the first term of the Debye series

n	0°	5°	10°
1.5	0.0777952+0.0403869j	0.058878+0.065063j	-0.0287411+0.0832092j
2	0.129659+0.0673116j	0.0980863+0.108389j	-0.0478136+0.138433j
3	0.194489+0.100968j	0.147064+0.162511j	-0.0715894+0.207276j
4	0.233387+0.121161j	0.176437+0.194969j	-0.0858291+0.248508j
5	0.259319+0.134624j	0.196015+0.216603j	-0.0953138+0.275971j
n	15°	20°	
1.5	-0.0759951-0.0453697j	0.0884871-0.0110493j	
2	-0.126147-0.0753054j	0.146413-0.0182905j	
3	-0.188457-0.112497j	0.21804-0.0272473j	

Table 10 The SDM results with respect to varying n, the geometrically lit region of the double positive cylinder corresponding to the first term of the Debye series (Cont'd)

n	15°	20°
4	-0.225692-0.134722j	0.260709-0.0325829j
5	-0.250465-0.149508j	0.289053-0.0361272j

Table 11 The percentage error in the magnitudes of the SDM results, the geometrically lit region of the double positive cylinder corresponding to the first term of the Debye series

n	0°	5°	10°
1.5	0.001303738	0.001422775	0.001488743
2	0.001462766	0.0015426	0.001487473
3	0.001225374	0.001394386	0.001679149
4	0.001490111	0.001330177	0.001310485
5	0.001161864	0.001143627	0.001428488
n	15°	20°	
1.5	0.001664168	0.002007237	
2	0.001587879	0.001513017	
3	0.001755394	0.002001514	
4	0.001593397	0.001871791	
5	0.001629581	0.001796254	

Second, the series results and the SDM results are tabulated with respect to varying operating frequencies. The following parameters are used in the calculations:

$$\begin{aligned}
 n &= 3 \\
 \mu_r &= 1 \\
 k_0\rho &= 3\left(\beta + \beta^{\frac{1}{3}}\right)
 \end{aligned}$$

Table 12 The tabulation of the results for $\beta = 10\pi$, the geometrically lit region of the double positive cylinder corresponding to the first term of the Debye series

	0°	5°	10°
Series	0.211088+0.00931496j	0.209945+0.0241705j	0.200309+0.0677121j
SDM	0.211041+0.00872599j	0.209938+0.0235699j	0.200433+0.0670942j
Percentage error for the magnitude of the SDM	0.03412577	0.035397303	0.037589081
	15°	20°	
Series	0.164885+0.132662j	0.0830161+0.194936j	
SDM	0.165239+0.132081j	0.0836648+0.194551j	
Percentage error for the magnitude of the SDM	0.04126199	0.046596951	

Table 13 The tabulation of the results for $\beta = 20\pi$, the geometrically lit region of the double positive cylinder corresponding to the first term of the Debye series

	0°	5°	10°
Series	-0.173117+0.128484j	-0.189577+0.102737j	-0.215187+0.0154159j
SDM	-0.172928+0.128707j	-0.189418+0.102989j	-0.215145+0.0157256j
Percentage error for the magnitude of the SDM	0.008659284	0.009052323	0.009055912
	15°	20°	
Series	-0.173767-0.128173j	0.011131-0.215889j	
SDM	-0.173949-0.127887j	0.0107539-0.215882j	
Percentage error for the magnitude of the SDM	0.010669967	0.012064413	

Table 14 The tabulation of the results for $\beta = 30\pi$, the geometrically lit region of the double positive cylinder corresponding to the first term of the Debye series

	0°	5°	10°
Series	-0.101123-0.192454j	-0.0580983-0.209537j	0.0784306-0.202928j
SDM	-0.101291-0.192356j	-0.0582858-0.209476j	0.0782338-0.202994j
Percentage error for the magnitude of the SDM	0.003920393	0.003952788	0.004268637
	15°	20°	
Series	0.215652-0.0301133j	0.0487773+0.212471j	
SDM	0.215611-0.0303349j	0.0490194+0.212403j	

Table 14 The tabulation of the results for $\beta = 30\pi$, the geometrically lit region of the double positive cylinder corresponding to the first term of the Debye series (Cont'd)

	15°	20°
Percentage error for the magnitude of the SDM	0.004520485	0.005486793

Table 15 The tabulation of the results for $\beta = 40\pi$, the geometrically lit region of the double positive cylinder corresponding to the first term of the Debye series

	0°	5°	10°
Series	0.169749-0.137494j	0.201582-0.0842667j	0.196101+0.0965975j
SDM	0.169654-0.137603j	0.201521-0.0844007j	0.196165+0.0964559j
Percentage error for the magnitude of the SDM	0.002365644	0.002082144	0.002334713
	15°	20°	
Series	-0.0660486+0.208583j	-0.165074-0.143985j	
SDM	-0.065886+0.208629j	-0.165193-0.143839j	
Percentage error for the magnitude of the SDM	0.002361473	0.002835043	

Table 16 The tabulation of the results for $\beta = 50\pi$, the geometrically lit region of the double positive cylinder corresponding to the first term of the Debye series

	0°	5°	10°
Series	0.194438+0.101072j	0.146979+0.162592j	-0.0717077+0.207239j
SDM	0.194489+0.100968j	0.147064+0.162511j	-0.0715894+0.207276j
Percentage error for the magnitude of the SDM	0.001225374	0.001394386	0.001679149
	15°	20°	
Series	-0.188391-0.112615j	0.218063-0.0270983j	
SDM	-0.188457-0.112497j	0.21804-0.0272473j	
Percentage error for the magnitude of the SDM	0.001755394	0.002001514	

5.3 The Geometrical Shadow Region of the Double Positive Cylinder Corresponding to the Second Term of the Debye Series

The contribution of the second term of the Debye series to the corresponding geometrical shadow region is represented by the following series for the double positive cylinder:

$$\sum_{l=-\infty}^{\infty} 0.5 j^{-l} T_{12}(l) T_{21}(l) \frac{H_l^{(2)}(\beta) H_l^{(1)}(\alpha)}{H_l^{(1)}(\beta) H_l^{(2)}(\alpha)} H_l^{(1)}(k_0 \rho) e^{-jl\phi} \quad (179)$$

The series is computed in the geometrical shadow region corresponding to the second term of the Debye series using Mathematica and is compared to the residue series result. The residue series computation is carried out by using only three terms of the series corresponding to first three poles of the integrand of the integral calculated by the residue series. The Debye approximation is not employed in the residue series computations. The comparisons are shown in the following tabulations.

First, the series and the residue series results are tabulated with respect to varying n. The following parameters are used in the calculations:

$$\begin{aligned} \beta &= 50\pi \\ \mu_r &= 1 \\ k_0 \rho &= 3 \left(\beta + \beta^{\frac{1}{3}} \right) \end{aligned}$$

Table 17 The tabulation for $n = 1.5$, the geometrical shadow region of the double positive cylinder corresponding to the second term of the Debye series

	-102.421°	-81.9364°	-61.4523°
Series	0.00811495+0.0287956j	-0.0028666+0.00368152j	-0.000476873-0.000182164j
Residue series without the Debye approximation	0.00787638+0.0293638j	-0.00286644+0.00368143j	-0.000476873-0.000182164j
Percentage error for the magnitude of the residue series	1.619832997	0.003628638	0
	-40.9682°	-20.4841°	0°
Series	$7.0813 \times 10^{-6} - 4.53639 \times 10^{-5} j$	$3.70995 \times 10^{-6} - 1.11998 \times 10^{-7} j$	$1.19492 \times 10^{-7} + 5.59763 \times 10^{-7} j$
Residue series without the Debye approximation	$7.0813 \times 10^{-6} - 4.53639 \times 10^{-5} j$	$3.70995 \times 10^{-6} - 1.11999 \times 10^{-7} j$	$1.19492 \times 10^{-7} + 5.59763 \times 10^{-7} j$
Percentage error for the magnitude of the residue series	0	8.12981×10^{-7}	0

Table 18 The tabulation for $n = 2$, the geometrical shadow region of the double positive cylinder corresponding to the second term of the Debye series

	-78.7999°	-63.0399°	-47.2799°
Series	0.0168291-0.0107059j	0.00446829-0.0017163j	0.00088392+0.0000841903j
Residue series without the Debye approximation	0.0175271-0.0097219j	0.00446721-0.0017188j	0.000883942+0.0000842033j
Percentage error for the magnitude of the residue series	0.486415296	0.002318948	0.002605366
	-31.52°	-15.76°	0°
Series	0.000110704+0.0000838428j	$6.34239 \times 10^{-6} + 1.87364 \times 10^{-5} j$	$-1.28445 \times 10^{-6} + 5.08038 \times 10^{-6} j$
Residue series without the Debye approximation	0.000110703+0.0000838431j	$6.34239 \times 10^{-6} + 1.87364 \times 10^{-5} j$	$-1.28445 \times 10^{-6} + 5.08038 \times 10^{-6} j$
Percentage error for the magnitude of the residue series	0.000443613	0	0

Table 19 The tabulation for $n = 3$, the geometrical shadow region of the double positive cylinder corresponding to the second term of the Debye series

	-57.7423°	-46.1939°	-34.6454°
Series	-0.00151798-0.0124084j	-0.00319885-0.00309481j	0.00127646+0.00044366j
Residue series without the Debye approximation	-0.000198208-0.0118244j	-0.00318208-0.00309723j	0.00127663+0.000443667j
Percentage error for the magnitude of the residue series	5.398368627	0.23252977	0.012052728
	-23.0969°	-11.5485°	0°
Series	$1.78828 \times 10^{-5} + 0.000361966j$	$-7.98758 \times 10^{-5} + 2.99428 \times 10^{-5}j$	$-2.72072 \times 10^{-5} - 3.08645 \times 10^{-5}j$
Residue series without the Debye approximation	$1.78809 \times 10^{-5} + 0.000361967j$	$-7.98758 \times 10^{-5} + 2.99428 \times 10^{-5}j$	$-2.72072 \times 10^{-5} - 3.08645 \times 10^{-5}j$
Percentage error for the magnitude of the residue series	0.000249728	0	0

Table 20 The tabulation for $n = 4$, the geometrical shadow region of the double positive cylinder corresponding to the second term of the Debye series

	-47.7549°	-38.2039°	-28.6529°
Series	0.00892118-0.00233223j	0.000898382+0.00385j	-0.00150771+9.96836x10 ⁻³ j
Residue series without the Debye approximation	0.00817356-0.000571589j	0.000918087+0.00381587j	-0.0015082+0.000100244j
Percentage error for the magnitude of the residue series	11.14276036	0.725113087	0.034811011
	-19.102°	-9.55098°	0°
Series	$9.60039 \times 10^{-5} - 0.000516861j$	$0.000144047 + 6.1196 \times 10^{-5}j$	$-7.0413 \times 10^{-5} + 7.4897 \times 10^{-5}j$
Residue series without the Debye approximation	$9.60161 \times 10^{-5} - 0.000516865j$	$0.000144046 + 6.11958 \times 10^{-5}j$	$-7.0413 \times 10^{-5} + 7.48971 \times 10^{-5}j$
Percentage error for the magnitude of the residue series	0.001171925	0.000638046	7.08745E-05

Table 21 The tabulation for $n = 5$, the geometrical shadow region of the double positive cylinder corresponding to the second term of the Debye series

	-41.8738°	-33.499°	-25.1243°
Series	-0.000442139+0.00731774j	0.00349516-0.000252527j	-0.000141901-0.00151922j
Residue series without the Debye approximation	-0.00167997+0.00592755j	0.00344391-0.0002288648j	-0.000143786-0.00152006j
Percentage error for the magnitude of the residue series	15.9603451	1.505719992	0.066371782
	-16.7495°	-8.37476°	0°
Series	-0.000624322+2.23494x10 ⁻⁵ j	-2.94065 x10 ⁻⁶ +0.000204502j	0.000165061+2.57575 x10 ⁻⁵ j
Residue series without the Debye approximation	-0.000624386+2.23343 x10 ⁻⁵ j	-0.00000294248+0.000204502j	0.000165061+2.57575 x10 ⁻⁵ j
Percentage error for the magnitude of the residue series	0.010151568	1.2869x10 ⁻⁵	0

Second, the series and the residue series results are tabulated with respect to varying operating frequency. The following parameters are used in the calculations:

$$\begin{aligned}
 n &= 3 \\
 \mu_r &= 1 \\
 k_0\rho &= 3\left(\beta + \beta^{\frac{1}{3}}\right)
 \end{aligned}$$

Table 22 The tabulation for $\beta = 10\pi$, the geometrical shadow region of the double positive cylinder corresponding to the second term of the Debye series

	-56.5749°	-45.2599°	-33.9449°
Series	0.0199969-0.0171593j	0.0135712-0.00616888j	0.00793058-0.000507103j
Residue series without the Debye approximation	0.0209684-0.0166604j	0.0135461-0.00610014j	0.00792589-0.000508304j
Percentage error for the magnitude of the residue series	1.6375046	0.343477699	0.057931182

Table 22 The tabulation for $\beta = 10\pi$, the geometrical shadow region of the double positive cylinder corresponding to the second term of the Debye series (Cont'd)

	-22.63°	-11.315°	0°
Series	0.00376084+0.00153307j	0.00137366+0.00186362j	0.000621587+0.00182093j
Residue series without the Debye approximation	0.00376089+0.00153276j	0.00137368+0.00186362j	0.000621587+0.00182093j
Percentage error for the magnitude of the residue series	0.001740991	0.00051256	0

Table 23 The tabulation for $\beta = 20\pi$, the geometrical shadow region of the double positive cylinder corresponding to the second term of the Debye series

	-57.2126°	-45.7701°	-34.3275°
Series	-0.00237558-0.0190577j	0.00299391-0.00870605j	0.00315406-0.00252371j
Residue series without the Debye approximation	-0.000919246-0.0191861j	0.00298094-0.00866035j	0.00315288-0.00252466j
Percentage error for the magnitude of the residue series	0.015200152	0.515219765	0.008109063
	-22.885°	-11.4425°	0°
Series	0.00162306-0.0000537783j	0.000475703+0.000449058j	0.000114048+0.000451814j
Residue series without the Debye approximation	0.00162311-0.0000537988j	0.000475703+0.000449059j	0.000114048+0.000451814j
Percentage error for the magnitude of the residue series	0.003119033	0.000104933	0

Table 24 The tabulation for $\beta = 30\pi$, the geometrical shadow region of the double positive cylinder corresponding to the second term of the Debye series

	-57.4832°	-45.9866°	-34.4899°
Series	-0.0150892+0.00501975j	-0.00647151-0.00197141j	-0.00127781-0.00222817j
Residue series without the Debye approximation	-0.0152304+0.00337952j	-0.00644602-0.00195169j	-0.00127842-0.0022281j
Percentage error for the magnitude of the residue series	1.895442507	0.445232939	0.009452784
	-22.9933°	-11.4966°	0°
Series	0.000267-0.000838659j	0.000268146-0.0000829196j	0.000152594+0.0000832453j
Residue series without the Debye approximation	0.000267008-0.000838667j	0.000268146-0.0000829194j	0.000152594+0.0000832453j
Percentage error for the magnitude of the residue series	0.001141861	2.10515x10 ⁻⁵	0

Table 25 The tabulation for $\beta = 40\pi$, the geometrical shadow region of the double positive cylinder corresponding to the second term of the Debye series

	-57.639°	-46.1112°	-34.5834°
Series	0.0108217+0.0087106j	0.000647306+0.00532905j	-0.0013118+0.00124403j
Residue series without the Debye approximation	0.00931399+0.0096015j	0.000659043+0.0053094j	-0.00131183+0.00124432j
Percentage error for the magnitude of the residue series	3.707514424	0.336666399	0.012242597
	-23.0556°	-11.5278°	0°
Series	-0.000526443-0.000135682j	-2.95322x10 ⁻⁵ -0.00014313j	5.74618 x10 ⁻⁵ -5.49643 x10 ⁻⁵ j
Residue series without the Debye approximation	-0.000526444-0.000135685j	-2.95321 x10 ⁻⁵ -0.00014313j	5.74618 x10 ⁻⁵ -5.49643 x10 ⁻⁵ j
Percentage error for the magnitude of the residue series	0.000315847	1.3827 x10 ⁻⁵	0

Table 26 The tabulation for $\beta = 50\pi$, the geometrical shadow region of the double positive cylinder corresponding to the second term of the Debye series

	-57.7423°	-46.1939°	-34.6454°
Series	-0.00151798-0.0124084j	0.00319885-0.00309481j	0.00127646+0.00044366j
Residue series without the Debye approximation	0.000198208-0.0118244j	0.00318208-0.00309723j	0.00127663+0.000443667j
Percentage error for the magnitude of the residue series	5.398368627	0.23252977	0.012052728
	-23.0969°	-11.5485°	0°
Series	1.78828x10 ⁻⁵ +0.000361966j	-7.98758x10 ⁻⁵ +2.99428x10 ⁻⁵ j	-2.72072x10 ⁻⁵ -3.08645x10 ⁻⁵ j
Residue series without the Debye approximation	1.78809x10 ⁻⁵ +0.000361967j	-7.98758x10 ⁻⁵ +0.0000299428j	-2.72072x10 ⁻⁵ -3.08645x10 ⁻⁵ j
Percentage error for the magnitude of the residue series	0.000249728	0	0

5.4 The Geometrically Lit Region of the Double Positive Cylinder Corresponding to the Second Term of the Debye Series

The contribution of the second term of the Debye series to the corresponding geometrically lit region is calculated both by using the series expression and by the saddle point method (SDM). The computed series is given by the following expression for the double positive cylinder:

$$\sum_{l=-\infty}^{\infty} 0.5 j^{-l} T_{12}(l) T_{21}(l) \frac{H_l^{(2)}(\beta) H_l^{(1)}(\alpha)}{H_l^{(1)}(\beta) H_l^{(2)}(\alpha)} H_l^{(1)}(k_0 \rho) e^{-jl\phi} \quad (180)$$

The integral corresponding to the series is calculated using the SDM. The integrand of the integral does not vanish as $|v| \rightarrow \infty$ in the lower half of the v -plane. Hence, only the upper part of the steepest descent path contributes to the

integral. This causes a $\frac{1}{2}$ factor to be put in front of the SDM result of the integral.

First, the series results and the SDM results are displayed in a table with respect to varying refractive indices. The following parameters are used in the calculations:

$$\begin{aligned}\beta &= 50\pi \\ \mu_r &= 1 \\ k_0\rho &= 3\left(\beta + \beta^{\frac{1}{3}}\right)\end{aligned}$$

Table 27 The series results with respect to varying refractive indices, the geometrically lit region of the double positive cylinder corresponding to the second term of the Debye series

n	161.2°	164.96°	168.72°
1.5	-0.543463-j0.135508	-0.638525+j0.00360506	-0.547074-j0.477797
2	0.0839989+j0.518188	-0.514014-j0.204624	0.56774+j0.10663
3	-0.258209-j0.299259	0.19536+j0.354863	0.135407-j0.390139
4	-0.306748+j0.0837676	0.305996+j0.106257	-0.0276797-j0.327458
5	-0.184307+j0.19298	0.271129-j0.00462893	-0.0769239-j0.263577
n	172.48°	176.24°	180°
1.5	0.73072-j0.368002	-0.89048+j0.100699	-0.436084+j0.819792
2	-0.374067-j0.464854	-0.50606+j0.338426	-0.28484+j0.542764
3	-0.406106-j0.10207	-0.307772+j0.289094	-0.196419+j0.375124
4	-0.331469-j0.019358	-0.232422+j0.240004	-0.155273+j0.296605
5	-0.276897+j0.00859809	-0.189217+j0.204372	-0.129405+j0.247188

Table 28 The SDM results with respect to varying refractive indices, the geometrically lit region of the double positive cylinder corresponding to the second term of the Debye series

n	161.2°	164.96°	168.72°
1.5	-0.544241-j0.131481	-0.638338+j0.00728203	-0.549592-j0.474695
2	0.0866296+j0.517714	-0.514949-j0.202171	0.568194+j0.104038
3	-0.25942-j0.29819	0.196725+j0.354093	0.133956-0.390627
4	-0.306412+j0.0849537	0.306379+j0.105119	-0.0288521-j0.327348
5	-0.183564+j0.193676	0.271103-j0.00562478	-0.0778616-j0.263295
n	172.48°	176.24°	180°
1.5	0.72817-j0.372793	-0.889548+j0.108511	-0.427871+j0.824187
2	-0.376129-j0.463159	-0.504535+0.340662	-0.282418+j0.544008
3	-0.40646-j0.100606	-0.306741+j0.290172	-0.195095+j0.375802
4	-0.331527-j0.0181989	-0.231589+j0.240797	-0.154252+j0.297129
5	-0.276859+j0.00956449	-0.188507+j0.205019	-0.128553+j0.247626

Table 29 The percentage error in the magnitude of the SDM results, the geometrically lit region of the double positive cylinder corresponding to the second term of the Debye series

n	161.2°	164.96°	168.72°
1.5	0.03649382	0.02437489	0.018314087
2	0.007647069	0.005846285	0.004545734
3	0.003784372	0.003260423	0.002882563
4	0.002918323	0.002862235	0.002662558
5	0.002959991	0.002643004	0.002278534
n	172.48°	176.24°	180°
1.5	0.012775426	0.001533926	0.007516596
2	0.003662533	0.00306465	0.00292165
3	0.002586232	0.002555896	0.002575825
4	0.002303246	0.002349911	0.002189631
5	0.002274031	0.002132304	0.001960057

Second, the series results and the SDM results are tabulated with respect to varying operating frequencies. The following parameters are used in the calculations:

$$n = 3$$

$$\mu_r = 1$$

$$k_0\rho = 3\left(\beta + \beta^{\frac{1}{3}}\right)$$

Table 30 The tabulation of the results for $\beta = 10\pi$, the geometrically lit region of the double positive cylinder corresponding to the second term of the Debye series

	162.368°	165.894°	169.421°
Series	-0.382611+0.0329866j	-0.324655+0.219775j	-0.217164+0.334069j
SDM	-0.381569+0.0404719j	-0.320234+0.225665j	-0.210934+0.337721j
Percentage error for the magnitude of the SDM	0.083577722	0.074005858	0.067316171
	172.947°	176.474°	180°
Series	-0.115031+0.386353j	-0.0471518+0.403203j	-0.0238449+0.406204j
SDM	-0.108122+0.388081j	-0.040107+0.40372j	-0.0168012+0.406315j
Percentage error for the magnitude of the SDM	0.062647672	0.059953183	0.059239932

Table 31 The tabulation of the results for $\beta = 20\pi$, the geometrically lit region of the double positive cylinder corresponding to the second term of the Debye series

	161.73°	165.384°	169.038°
Series	0.247034+0.302048j	0.389934-0.085446j	0.191523-0.358414j
SDM	0.250002+0.299483j	0.389025-0.0891485j	0.188192-0.360094j
Percentage error for the magnitude of the SDM	0.022242295	0.019342244	0.017482649
	172.962°	176.346°	180°
Series	-0.0537704-0.408098j	-0.201002-0.362872j	-0.245392-0.335786j
SDM	-0.0574018-0.407536j	-0.204149-0.361038j	-0.248277-0.333581j
Percentage error for the magnitude of the SDM	0.016135957	0.015296785	0.014951493

Table 32 The tabulation of the results for $\beta = 30\pi$, the geometrically lit region of the double positive cylinder corresponding to the second term of the Debye series

	161.459°	165.167°	168.876°
Series	-0.15478-0.361017j	-0.344881+0.206948j	0.124864+0.390258j
SDM	-0.157201-0.359926j	-0.343518+0.209135j	0.127252+0.389452j
Percentage error for the magnitude of the SDM	0.010125209	0.008751774	0.007860481
	172.584°	176.292°	180°
Series	0.39709+0.121484j	0.401783-0.117514j	0.372534-0.193399j
SDM	0.39778+0.119101j	0.401058-0.119863j	0.371373-0.195558j
Percentage error for the magnitude of the SDM	0.007206802	0.006979608	0.006787953

Table 33 The tabulation of the results for $\beta = 40\pi$, the geometrically lit region of the double positive cylinder corresponding to the second term of the Debye series

	161.303°	165.043°	168.782°
Series	0.174053+0.353782j	0.144813-0.377089j	-0.40888-0.0479778j
SDM	0.175843+0.352871j	0.142985-0.377764j	-0.409079-0.046084j
Percentage error for the magnitude of the SDM	0.005611722	0.005077435	0.004531601
	172.521°	176.261°	180°
Series	-0.153738+0.388002j	0.168887+0.385425j	0.264367+0.328882j
SDM	-0.151988+0.388672j	0.170579+0.384661j	0.265797+0.327706j
Percentage error for the magnitude of the SDM	0.004205176	0.003944512	0.003935127

Table 34 The tabulation of the results for $\beta = 50\pi$, the geometrically lit region of the double positive cylinder corresponding to the second term of the Debye series

	161.2°	164.96°	168.72°
Series	-0.258209-0.299259j	0.19536+0.354863j	0.135407-0.390139j
SDM	-0.25942-0.29819j	0.196725+0.354093j	0.133956-0.390627j
Percentage error for the magnitude of the SDM	0.003784372	0.003260423	0.002882563
	172.48°	176.24°	180°
Series	-0.406106-0.10207j	-0.307772+0.289094j	-0.196419+0.375124j
SDM	-0.40646-0.100606j	-0.306741+0.290172j	-0.195095+0.375802j

Table 34 The tabulation of the results for $\beta = 50\pi$, the geometrically lit region of the double positive cylinder corresponding to the second term of the Debye series (Cont'd)

	172.48°	176.24°	180°
Percentage error for the magnitude of the SDM	0.002586232	0.002555896	0.002575825

5.5 The Geometrical Shadow Region of the Double Negative Cylinder Corresponding to the First Term of the Debye Series

The following series expression represents the contribution of the first term of the Debye series to the field in the geometrical shadow region corresponding to the first term of the Debye series for the DNG cylinder:

$$\sum_{l=-\infty}^{\infty} \frac{1}{2} j^{-l} \left[R_{22}(l) \frac{H_l^{(2)}(\beta)}{H_l^{(1)}(\beta)} H_l^{(1)}(k_0 \rho) + H_l^{(2)}(k_0 \rho) \right] e^{-jl\phi} \quad (181)$$

Mathematica is used in the computation of the series. Calculation of the integral corresponding to the series is carried out using the residue series. The results shown in the tables are obtained using only three terms of the residue series corresponding to first three poles of the integrand. There is an obvious computational advantage. The Debye expansion for $H_v^{(1)}(k_0 \rho)$ in the residue series is not applied for getting the residue series results.

First, the tabulation of the series and the residue series results are made with respect to n . The following parameters are used in the calculations:

$$\begin{aligned} \beta &= 50\pi \\ \mu_r &= -1 \\ k_0 \rho &= 3 \left(\beta + \beta^{\frac{1}{3}} \right) \end{aligned}$$

Table 35 The tabulation of the series results with respect to n, the geometrical shadow region of the double negative cylinder corresponding to the first term of the Debye series

n	161.2°	164.96°	168.72°
-1.5	-0.379787+0.172141j	0.0690321+0.145803j	0.057261-0.0487625j
-2	-0.374195+0.174326j	0.0686548+0.141589j	0.054019-0.0470544j
-3	-0.370295+0.175864j	0.0683862+0.138669j	0.0518655-0.0458897j
-4	-0.368641+0.176517j	0.0682703+0.137437j	0.0509783-0.0454026j
-5	-0.367705+0.176887j	0.0682042+0.136741j	0.0504828-0.0451287j
n	172.48°	176.24°	180°
-1.5	-0.0357022-0.0132994j	-0.00607961+0.0153692j	0.0227744-0.00735572j
-2	-0.0333277-0.0124693j	-0.00528976+0.0143191j	0.0203557-0.00674348j
-3	-0.0317714-0.0119036j	-0.00479248+0.0136177j	0.0188184-0.00634356j
-4	-0.031135-0.0116677j	-0.00459408+0.0133282j	0.0182011-0.00618047j
-5	-0.0307807-0.0115351j	-0.00448488+0.0131663j	0.0178605-0.00608991j

Table 36 The tabulation of the residue series results with respect to n, the geometrical shadow region of the double negative cylinder corresponding to the first term of the Debye series

n	161.2°	164.96°	168.72°
-1.5	-0.299356+0.074339j	0.0633379+0.127624j	0.0542479-0.0490218j
-2	-0.297064+0.0759645j	0.0626955+0.124131j	0.0511558-0.0472228j
-3	-0.295446+0.0772575j	0.0622797+0.121706j	0.049105-0.0460048j
-4	-0.294754+0.0778325j	0.0621081+0.120682j	0.0482606-0.0454969j
-5	-0.294361+0.0781634j	0.0620119+0.120103j	0.047789-0.0452116j
n	172.48°	176.24°	180°
-1.5	-0.0358987-0.0128224j	-0.00600752+0.0154229j	0.0228018-0.00737693j
-2	-0.0334971-0.0120215j	-0.00522277+0.014366j	0.0203794-0.00676312j
-3	-0.0319246-0.0114758j	-0.00472903+0.0136604j	0.0188398-0.00636206j
-4	-0.0312818-0.0112482j	-0.0045321+0.0133692j	0.0182217-0.0061985j
-5	-0.030924-0.0111203j	-0.00442373+0.0132065j	0.0178805-0.00610766j

Table 37 The tabulation of the error in the magnitudes of the residue series results with respect to n , the geometrical shadow region of the double negative cylinder corresponding to the first term of the Debye series

n	161.2°	164.96°	168.72°
-1.5	26.0277082	11.68043921	2.784514192
-2	25.72284684	11.62363111	2.818869024
-3	25.50517893	11.57679535	2.835851408
-4	25.4122978	11.55567987	2.842098704
-5	25.35965865	11.54363599	2.845602239
n	172.48°	176.24°	180°
-1.5	0.055425729	0.143061852	0.136195848
-2	0.013943727	0.137469196	0.133731128
-3	0.010576374	0.13441283	0.131887027
-4	0.020374045	0.132983807	0.131653501
-5	0.02569378	0.133119844	0.130687912

Second, the tabulation of the series and the residue series results are made with respect to the operating frequency. The calculations are made with the following parameters:

$$\begin{aligned}
 n &= -3 \\
 \mu_r &= -1 \\
 k_0\rho &= 3\left(\beta + \beta^{\frac{1}{3}}\right)
 \end{aligned}$$

Table 38 The tabulation of the residue series results for $\beta = 10\pi$, the geometrical shadow region of the double negative cylinder corresponding to the first term of the Debye series

	162.368°	165.894°	169.421°
Series	-0.061015-0.376474j	0.215468+0.117267j	-0.166974+0.0617348j
Residue series without the Debye approximation	-0.0034586-0.331269j	0.188319+0.113953j	-0.157882+0.0571969j
Percentage error for the magnitude of the residue series	13.13608746	10.27261898	5.672273443
	172.947°	176.424°	180°
Series	0.0405906-0.0842335j	0.0608833+0.017155j	-0.0967225+0.0233301j

Table 38 The tabulation of the residue series results for $\beta = 10\pi$, the geometrical shadow region of the double negative cylinder corresponding to the first term of the Debye series (Cont'd)

	172.947°	176.424°	180°
Residue series without the Debye approximation	0.0388758-0.0809121j	0.0604495+0.0157167j	-0.0959237+0.0240816j
Percentage error for the magnitude of the residue series	3.996079265	1.256478807	0.59907445

Table 39 The tabulation of the residue series results for $\beta = 20\pi$, the geometrical shadow region of the double negative cylinder corresponding to the first term of the Debye series

	161.73°	165.384°	169.038°
Series	-0.0751919+0.391928j	0.20679-0.00215453j	-0.0449515-0.115673j
Residue series without the Debye approximation	-0.112448+0.306626j	0.182639+0.00353131j	-0.0440576-0.109091j
Percentage error for the magnitude of the residue series	18.16222519	11.66728495	5.196281977
	172.692°	176.346°	180°
Series	-0.0355618+0.0545043j	0.0271676+0.0224617j	-0.0113677-0.0521238j
Residue series without the Debye approximation	-0.0337394+0.0543315j	0.0271285+0.0219958j	-0.0116579-0.0520946j
Percentage error for the magnitude of the residue series	1.727903316	0.923124796	0.063906225

Table 40 The tabulation of the residue series results for $\beta = 30\pi$, the geometrical shadow region of the double negative cylinder corresponding to the first term of the Debye series

	161.459°	165.167°	168.876°
Series	-0.0838941-0.394859j	0.0332387-0.186288j	0.0354313-0.09072j
Residue series without the Debye approximation	-0.010621-0.317986j	0.0311069-0.164185j	0.0319405-0.0875288j
Percentage error for the magnitude of the residue series	21.18289661	11.69173583	4.331925176
	172.584°	176.292°	180°
Series	0.0268809-0.0507356j	0.0214812-0.0339779j	0.0197718-0.0292801j
Residue series without the Debye approximation	0.0258392-0.0506577j	0.0212788-0.0341171j	0.0197263-0.0293842j
Percentage error for the magnitude of the residue series	0.957313357	0.025498939	0.172484766

Table 41 The tabulation of the residue series results for $\beta = 40\pi$, the geometrical shadow region of the double negative cylinder corresponding to the first term of the Debye series

	161.303°	165.043°	168.782°
Series	0.341579+0.218901j	-0.170129+0.00617772j	0.0536793-0.0603552j
Residue series without the Debye approximation	0.225867+0.211531j	-0.150182+0.00622232j	0.0502126-0.0595916j
Percentage error for the magnitude of the residue series	23.72396275	11.70708881	3.524228236
	172.521°	176.261°	180°
Series	0.00529827+0.0366248j	-0.0212161-0.00135912j	0.0221046-0.0132216j
Residue series without the Debye approximation	0.00587851+0.0362946j	-0.0213026-0.00125467j	0.0221237-0.0132716j
Percentage error for the magnitude of the residue series	0.644407216	0.375961669	0.163368355

Table 42 The tabulation of the residue series results for $\beta = 50\pi$, the geometrical shadow region of the double negative cylinder corresponding to the first term of the Debye series

	161.2°	164.96°	168.72°
Series	-0.370295+0.175864j	0.0683862+0.138669j	0.0518655-0.0458897j
Residue series without the Debye approximation	-0.295446+0.0772575j	0.0622797+0.121706j	0.049105-0.0460048j
Percentage error for the magnitude of the residue series	25.50517893	11.57679535	2.835851408
	172.48°	176.24°	180°
Series	-0.0317714-0.0119036j	-0.00479248+0.0136177j	0.0188184-0.00634356j
Residue series without the Debye approximation	-0.0319246-0.0114758j	-0.00472903+0.0136604j	0.0188398-0.00636206j
Percentage error for the magnitude of the residue series	0.010576374	0.13441283	0.131887027

5.6 The Geometrically Lit Region of the Double Negative Cylinder Corresponding to the First Term of the Debye Series

The contribution of the first term of the Debye series to the corresponding geometrically lit region for the DNG cylinder is obtained using the following series:

$$\sum_{l=-\infty}^{\infty} \frac{1}{2} j^{-l} \left[R_{22}(l) \frac{H_l^{(2)}(\beta)}{H_l^{(1)}(\beta)} - 1 \right] H_l^{(1)}(k_0 \rho) e^{-jl\phi} \quad (182)$$

The series is computed using Mathematica at the field points. The integral corresponding to the series is calculated using the SDM. The SDM result is scaled by $\frac{1}{2}$ because the integrand does not vanish as $|v| \rightarrow \infty$ in the lower half of the v -plane and only the upper half of the steepest descent path is traversed. First, the tabulation of the series and the SDM results are made with respect to n . The following parameters are used in the calculations:

$$\beta = 50\pi$$

$$\mu_r = -1$$

$$k_0\rho = 3\left(\beta + \beta^{\frac{1}{3}}\right)$$

Table 43 The tabulation of the series results with respect to n, the geometrically lit region of the double negative cylinder corresponding to the first term of the Debye series

n	0°	5°	10°
-1.5	0.0774171+0.0411237j	0.0582661+0.0656221j	-0.0295278+0.0829418j
-2	0.129383+0.0678496j	0.0976393+0.108798j	-0.0483891+0.138237j
-3	0.194277+0.101381j	0.14672+0.162826j	-0.0720361+0.207125j
-4	0.233185+0.121558j	0.176108+0.195272j	-0.0862605+0.248363j
-5	0.259111+0.135031j	0.195676+0.216914j	-0.0957583+0.275822j
n	15°	20°	
-1.5	-0.0755711-0.0460884j	0.0885957-0.010217j	
-2	-0.125836-0.0758324j	0.146493-0.017678j	
-3	-0.188213-0.112912j	0.218105-0.0267571j	
-4	-0.225455-0.135126j	0.260774-0.0321003j	
-5	-0.250221-0.149926j	0.289121-0.0356253j	

Table 44 The tabulation of the SDM results with respect to n, the geometrically lit region of the double negative cylinder corresponding to the first term of the Debye series

n	0°	5°	10°
-1.5	0.0773859+0.0411803j	0.058217+0.0656643j	-0.0295889+0.0829189j
-2	0.129374+0.0678624j	0.0976275+0.108806j	-0.0484+0.138232j
-3	0.194329+0.101277j	0.146806+0.162745j	-0.0719181+0.207163j
-4	0.233284+0.121359j	0.176272+0.195119j	-0.0860391+0.248436j
-5	0.259247+0.134761j	0.1959+0.216707j	-0.0954595+0.275921j
n	15°	20°	
-1.5	-0.0755357-0.0461439j	0.0886019-0.0101506j	
-2	-0.12583-0.0758382j	0.146491-0.0176762j	
-3	-0.18828-0.112794j	0.218083-0.0269062j	
-4	-0.225579-0.134911j	0.260736-0.0323659j	
-5	-0.250387-0.14964j	0.289072-0.0359769j	

Table 45 The tabulation of the percentage errors in the magnitudes of the SDM results with respect to n , the geometrically lit region of the double negative cylinder corresponding to the first term of the Debye series

n	0°	5°	10°
-1.5	0.001115536	0.001162385	0.001200975
-2	0.001386143	0.001317989	0.000763007
-3	0.000904721	0.001174067	0.001293055
-4	0.001561836	0.001402496	0.001360445
-5	0.001374673	0.001199037	0.001474144
n	15°	20°	
-1.5	0.001469597	0.001595416	
-2	0.00146005	0.0014918	
-3	0.00146169	0.001651576	
-4	0.001541313	0.001952084	
-5	0.001513114	0.001859621	

Second, the tabulation of the series and the SDM results are made with respect to the operating frequency. The calculations are made with the following parameters:

$$\begin{aligned}
 n &= -3 \\
 \mu_r &= -1 \\
 k_0 \rho &= 3 \left(\beta + \beta^{\frac{1}{3}} \right)
 \end{aligned}$$

Table 46 The tabulation of the SDM results for $\beta = 10\pi$, the geometrically lit region of the double negative cylinder corresponding to the first term of the Debye series

	0°	5°	10°
Series	0.211015+0.0109949j	0.209754+0.0258397j	0.199773+0.0692999j
SDM	0.210985+0.010406j	0.209764+0.0252404j	0.199915+0.068687j
Percentage error for the magnitude of the SDM result	0.028295155	0.029577262	0.031111304
	15°	20°	
Series	0.163839+0.133963j	0.0814906+0.195586j	
SDM	0.164209+0.133392j	0.0821476+0.195219j	
Percentage error for the magnitude of the SDM result	0.034927323	0.040007398	

Table 47 The tabulation of the SDM results for $\beta = 20\pi$, the geometrically lit region of the double negative cylinder corresponding to the first term of the Debye series

	0°	5°	10°
Series	-0.173629+0.127795j	-0.189985+0.101984j	-0.215249+0.0145633j
SDM	-0.173443+0.128021j	-0.189831+0.102237j	-0.21521+0.0148734j
Percentage error for the magnitude of the SDM result	0.007251963	0.007338419	0.008228621
	15°	20°	
Series	-0.173262-0.128858j	0.0119757-0.215845j	
SDM	-0.173448-0.128575j	0.0115987-0.215843j	
Percentage error for the magnitude of the SDM result	0.008971598	0.01043325	

Table 48 The tabulation of the SDM results for $\beta = 30\pi$, the geometrically lit region of the double negative cylinder corresponding to the first term of the Debye series

	0°	5°	10°
Series	-0.100613-0.192722j	-0.0575431-0.209691j	0.0789667-0.202721j
SDM	-0.100781-0.192626j	-0.0577312-0.209632j	0.0787706-0.202789j
Percentage error for the magnitude of the SDM result	0.003342099	0.003232775	0.003546962
	15°	20°	
Series	0.215731-0.0295466j	0.0482232+0.212598j	
SDM	0.215692-0.0297686j	0.0484658+0.212533j	
Percentage error for the magnitude of the SDM result	0.003857174	0.004394526	

Table 49 The tabulation of the SDM results for $\beta = 40\pi$, the geometrically lit region of the double negative cylinder corresponding to the first term of the Debye series

	0°	5°	10°
Series	0.170022-0.137156j	0.20175-0.0838661j	0.19591+0.096986j
SDM	0.169928-0.137266j	0.201689-0.0840006j	0.195975+0.0968449j
Percentage error for the magnitude of the SDM result	0.001853441	0.002128063	0.001963958
	15°	20°	
Series	-0.0664596+0.208453j	-0.164792-0.144308j	

Table 49 The tabulation of the SDM results for $\beta = 40\pi$, the geometrically lit region of the double negative cylinder corresponding to the first term of the Debye series (Cont'd)

	15°	20°
SDM	-0.0662974+0.2085j	-0.164912-0.144163j
Percentage error for the magnitude of the SDM result	0.002022595	0.002359092

Table 50 The tabulation of the SDM results for $\beta = 50\pi$, the geometrically lit region of the double negative cylinder corresponding to the first term of the Debye series

	0°	5°	10°
Series	0.194277+0.101381j	0.14672+0.162826j	-0.0720361+0.207125j
SDM	0.194329+0.101277j	0.146806+0.162745j	-0.0719181+0.207163j
Percentage error for the magnitude of the SDM result	0.000904721	0.001174067	0.001293055
	15°	20°	
Series	-0.188213-0.112912j	0.218105-0.0267571j	
SDM	-0.18828-0.112794j	0.218083-0.0269062j	
Percentage error for the magnitude of the SDM result	0.00146169	0.001651576	

5.7 The Geometrically Lit Region of the Double Negative Cylinder Corresponding to the Second Term of the Debye Series

The contribution of the second term of the Debye series to the corresponding geometrically lit region for the DNG cylinder is denoted by the following series:

$$\sum_{l=-\infty}^{\infty} 0.5 j^{-l} T_{12}(l) T_{21}(l) \frac{H_l^{(2)}(\beta) H_l^{(1)}(\alpha)}{H_l^{(1)}(\beta) H_l^{(2)}(\alpha)} H_l^{(1)}(k_0 \rho) e^{-jl\phi} \quad (183)$$

The series is computed using Mathematica. The integral corresponding to the series is computed using SDM. The SDM result is scaled by $\frac{1}{2}$. The reason of

the scaling is the fact that the integrand does not vanish as $|v| \rightarrow \infty$ in the lower half of the complex v -plane and only the upper half of the steepest descent path is traversed.

First, the series and the SDM results are tabulated with respect to varying n . The calculations are carried out with the following parameters:

$$\begin{aligned}\beta &= 50\pi \\ \mu_r &= -1 \\ k_0\rho &= 3\left(\beta + \beta^{\frac{1}{3}}\right)\end{aligned}$$

Table 51 The tabulation for the series results for varying n , the geometrically lit region of the double negative cylinder corresponding to the second term of the Debye series

n	161.2°	164.96°	168.72°
-1.5	-0.0439222+0.310061j	0.239372+0.202416j	0.312637-0.0262297j
-2	-0.144509+0.2708j	0.18477+0.245746j	0.307575+0.0131774j
-3	-0.222489+0.163j	0.096654+0.259189j	0.271431+0.0565408j
-4	-0.228129+0.085107j	0.0438046+0.240508j	0.233884+0.0737095j
-5	-0.212743+0.0367327j	0.0131297+0.21654j	0.202784+0.0793392j
n	172.48°	176.24°	180°
-1.5	0.250831-0.188751j	0.174388-0.261152j	0.144033-0.279086j
-2	0.256319-0.171031j	0.17498-0.253845j	0.141635-0.273916j
-3	0.241623-0.136895j	0.162109-0.225817j	0.128001-0.246857j
-4	0.219052-0.111433j	0.145861-0.198206j	0.113496-0.218479j
-5	0.19752-0.0930337j	0.13102-0.175087j	0.100967-0.194109j

Table 52 The tabulation for the SDM results for varying n , the geometrically lit region of the double negative cylinder corresponding to the second term of the Debye series

n	161.2°	164.96°	168.72°
-1.5	-0.0430699+0.31018j	0.239922+0.201764j	0.312565-0.0270754j
-2	-0.143778+0.271188j	0.185424+0.245252j	0.307608+0.0123647j
-3	-0.222029+0.163623j	0.0973704+0.258919j	0.271583+0.0557978j
-4	-0.227874+0.0857792j	0.0445019+0.240377j	0.234092+0.0730388j
-5	-0.212627+0.0373855j	0.0137826+0.216497j	0.203016+0.078735j

Table 52 The tabulation for the SDM results for varying n, the geometrically lit region of the double negative cylinder corresponding to the second term of the Debye series (Cont'd)

n	172.48°	176.24°	180°
-1.5	0.250322-0.189427j	0.173686-0.26162j	0.143283-0.279471j
-2	0.255868-0.171703j	0.174316-0.254302j	0.140919-0.274285j
-3	0.24125-0.137549j	0.161498-0.226252j	0.127335-0.2472j
-4	0.218733-0.112052j	0.1453-0.198615j	0.11288-0.218795j
-5	0.197243-0.0936136j	0.130506-0.175468j	0.100399-0.194401j

Table 53 The tabulation for the errors in the magnitudes of the SDM results for varying n, the geometrically lit region of the double negative cylinder corresponding to the second term of the Debye series

n	161.2°	164.96°	168.72°
-1.5	0.000170643	4.39294E-05	3.33126E-05
-2	0.000236932	0.000235974	0.000241109
-3	0.000652129	0.000581594	0.00060455
-4	0.001190052	0.001187877	0.000902208
-5	0.001028306	0.001115079	0.00143711
n	172.48°	176.24°	180°
-1.5	0.000284875	0.000156852	0.000224341
-2	0.0003576	0.000152877	1.18282E-05
-3	0.000405367	0.000694855	0.000382958
-4	0.001089556	0.000859906	0.001046813
-5	0.001166983	0.000902219	0.000972343

Second, the series and the SDM results are calculated with respect to varying operating frequency. The following parameters are used in the calculations:

$$n = -3$$

$$\mu_r = -1$$

$$k_0\rho = 3\left(\beta + \beta^{\frac{1}{3}}\right)$$

Table 54 The tabulation of the SDM results for $\beta = 10\pi$, the geometrically lit region of the double negative cylinder corresponding to the second term of the Debye series

	162.368°	165.894°	169.421°
Series	0.165122-0.209349j	0.114245-0.241671j	0.0702861-0.25846j
SDM	0.16214-0.211609j	0.110872-0.243187j	0.0667245-0.259354j
Percentage error for the magnitude of the SDM result	0.017253857	0.016987171	0.01746085
	172.947°	176.474°	180°
Series	0.0373394-0.265608j	0.0172015-0.267895j	0.0104554-0.268321j
SDM	0.0337167-0.26605j	0.0135695-0.268062j	0.00682203-0.268394j
Percentage error for the magnitude of the SDM result	0.015584703	0.015442723	0.016362857

Table 55 The tabulation of the SDM results for $\beta = 20\pi$, the geometrically lit region of the double negative cylinder corresponding to the second term of the Debye series

	161.73°	165.384°	169.038°
Series	-0.178073+0.20517j	-0.0613425+0.265427j	0.0414769+0.269839j
SDM	-0.17662+0.206406j	-0.059501+0.265834j	0.0433217+0.269538j
Percentage error for the magnitude of the SDM result	0.004512681	0.00425134	0.003968782
	172.692°	176.346°	180°
Series	0.112455+0.24923j	0.151519+0.227904j	0.163715+0.219411j
SDM	0.11414+0.24845j	0.15305+0.226866j	0.165186+0.218293j
Percentage error for the magnitude of the SDM result	0.004265526	0.003842701	0.003695972

Table 56 The tabulation of the SDM results for $\beta = 30\pi$, the geometrically lit region of the double negative cylinder corresponding to the second term of the Debye series

	161.459°	165.167°	168.876°
Series	0.0114781-0.273549j	-0.179551-0.207732j	-0.265175-0.0735414j
SDM	0.0101969-0.273595j	-0.180504-0.206897j	-0.265503-0.0723296j
Percentage error for the magnitude of the SDM result	0.001735179	0.002044558	0.001785459
	172.584°	176.292°	180°
Series	-0.272549+0.0410217j	-0.253945+0.107802j	-0.244077+0.128778j
SDM	-0.272356+0.0422537j	-0.253453+0.108942j	-0.243491+0.129872j

Table 56 The tabulation of the SDM results for $\beta = 30\pi$, the geometrically lit region of the double negative cylinder corresponding to the second term of the Debye series (Cont'd)

	172.584°	176.292°	180°
Percentage error for the magnitude of the SDM result	0.00169247	0.001676324	0.001806636

Table 57 The tabulation of the SDM results for $\beta = 40\pi$, the geometrically lit region of the double negative cylinder corresponding to the second term of the Debye series

	161.303°	165.043°	168.782°
Series	0.227751+0.154134j	0.250777-0.11481j	0.0932457-0.26023j
SDM	0.228289+0.153331j	0.250375-0.115676j	0.0923542-0.260545j
Percentage error for the magnitude of the SDM result	0.001021372	0.001224023	0.000927961
	172.521°	176.261°	180°
Series	-0.062011-0.269843j	-0.14909-0.233625j	-0.174768-0.215206j
SDM	-0.0629251-0.269628j	-0.149876-0.233118j	-0.17549-0.214614j
Percentage error for the magnitude of the SDM result	0.001162387	0.001075034	0.001019531

Table 58 The tabulation of the SDM results for $\beta = 50\pi$, the geometrically lit region of the double negative cylinder corresponding to the second term of the Debye series

	161.2°	164.96°	168.72°
Series	-0.222489+0.163j	0.096654+0.259189j	0.271431+0.0565408j
SDM	-0.222029+0.163623j	0.0973704+0.258919j	0.271583+0.0557978j
Percentage error for the magnitude of the SDM result	0.000652129	0.000581594	0.00060455
	172.48°	176.24°	180°
Series	0.241623-0.136895j	0.162109-0.225817j	0.128001-0.246857j
SDM	0.24125-0.137549j	0.161498-0.226252j	0.127335-0.2472j
Percentage error for the magnitude of the SDM result	0.000405367	0.000694855	0.000382958

5.8 The Geometrical Shadow Region of the Double Negative Cylinder Corresponding to the Second Term of the Debye Series

The following series expression represents the contribution of the second term of the Debye series to the field in the geometrical shadow region corresponding to the second term of the Debye series for the DNG cylinder:

$$\sum_{l=-\infty}^{\infty} 0.5 j^{-l} T_{12}(l) T_{21}(l) \frac{H_l^{(2)}(\beta) H_l^{(1)}(\alpha)}{H_l^{(1)}(\beta) H_l^{(2)}(\alpha)} H_l^{(1)}(k_0 \rho) e^{-jl\phi} \quad (184)$$

The computation of the series is carried out using Mathematica at the field points. The residue series calculations are made by using only three terms of the series. These three terms correspond to first three poles of the integrand of the integral calculated by the residue series.

First, the series and the residue series results are calculated with respect to varying n . In these calculations, for the operating frequency corresponding to $\beta = 50\pi$, the range of n is small. This is due to the double negative property of the cylinder. The geometrical shadow of the second term of the Debye series for the DNG cylinder is very small compared to that of the double positive cylinder for $|n| > \sqrt{2}$. The calculations are carried out with the following parameters:

$$\begin{aligned} \beta &= 50\pi \\ \mu_r &= -1 \\ k_0 \rho &= 1.4 \left(\beta + \beta^{\frac{1}{3}} \right) \end{aligned}$$

Table 59 The tabulation of the residue series results for $\beta = 50\pi$ and $n = -4$, the geometrical shadow region of the double negative cylinder corresponding to the second term of the Debye series

	-14.7198°	-11.7759°	-8.8319°
Series	0.0142191-0.00801176j	0.00251608+0.0110614j	-0.011142-0.00121268j
Residue series without the Debye approximation	0.0105111-0.00156402j	0.00216606+0.00880508j	-0.0106298-0.000738343j
Percentage error in the magnitude of the residue series	34.88816713	20.06671016	4.928596897
	-5.88794°	-2.94397°	0°
Series	0.0058922-0.00463913j	0.00397166+0.00176787j	-0.00845512+0.00118164j
Residue series without the Debye approximation	0.00568141-0.00465546j	0.00402406+0.0017269j	-0.00846816+0.0012186j
Percentage error in the magnitude of the residue series	2.055113714	0.726995125	0.212021275

Table 60 The tabulation of the residue series results for $\beta = 50\pi$ and $n = -5$, the geometrical shadow region of the double negative cylinder corresponding to the second term of the Debye series

	-20.6009°	-16.4808°	-12.3606°
Series	-0.00946064-0.00792567j	-0.00823302+0.00339752j	-0.00143224+0.00634083j
Residue series without the Debye approximation	-0.0046831-0.00750296j	-0.00734266+0.00318733j	-0.00128335+0.00625093j
Percentage error in the magnitude of the residue series	28.33671668	10.12624735	1.834643857
	-8.24038°	-4.12019°	0°
Series	0.0022886+0.00279095j	0.00209926-0.00154353j	0.00139885-0.00326749j
Residue series without the Debye approximation	0.00231037+0.00276613j	0.00210171-0.00154947j	0.00139907-0.00326984j
Percentage error in the magnitude of the residue series	0.14521514	0.210877984	0.06321885

Second, the series and the residue series results are tabulated with respect to varying operating frequency. The following parameters are used in the calculations:

$$n = -5$$

$$\mu_r = -1$$

$$k_0\rho = 1.4 \left(\beta + \beta^{\frac{1}{3}} \right)$$

Table 61 The tabulation of the residue series results for $\beta = 10\pi$ and $n = -5$, the geometrical shadow region of the double negative cylinder corresponding to the second term of the Debye series

	-17.3993°	-13.9194°	-10.4396°
Series	-0.00375665+0.0267447j	-0.0182038-0.00507654j	0.0180689-0.017382j
Residue series without the Debye approximation	-0.0104678+0.0222908j	-0.0147299-0.00572843j	0.017169-0.0161282j
Percentage error in the magnitude of the residue series	8.815960154	16.3707928	6.046924326
	-6.9597°	-3.47985°	0°
Series	-0.00374242+0.014962j	-0.00953008+0.00542795j	0.0143159-0.0170097j
Residue series without the Debye approximation	-0.00384263+0.0143189j	-0.00926057+0.00556499j	0.0140608-0.0169826j
Percentage error in the magnitude of the residue series	3.873451156	1.490002154	0.8288958

Table 62 The tabulation of the residue series results for $\beta = 20\pi$ and $n = -5$, the geometrical shadow region of the double negative cylinder corresponding to the second term of the Debye series

	-19.1307°	-15.3046°	-11.4784°
Series	-0.0181909+0.00950311j	0.0111202+0.00850514j	0.00653427-0.0111614j
Residue series without the Debye approximation	-0.0164586+0.00356829j	0.00930751+0.0077121j	0.00620732-0.0106218j
Percentage error in the magnitude of the residue series	17.94338023	13.66031107	4.87765339

Table 62 The tabulation of the residue series results for $\beta = 20\pi$ and $n = -5$, the geometrical shadow region of the double negative cylinder corresponding to the second term of the Debye series (Cont'd)

	-7.65229°	-3.82615°	0°
Series	-0.0103386+0.00268409j	-0.00112924+0.00439972j	0.00883171-0.00638149j
Residue series without the Debye approximation	-0.0101823+0.00281285j	-0.00108813+0.0043593j	0.00880904-0.0064148j
Percentage error in the magnitude of the residue series	1.101521656	1.084741781	0.011087685

Table 63 The tabulation of the residue series results for $\beta = 30\pi$ and $n = -5$, the geometrical shadow region of the double negative cylinder corresponding to the second term of the Debye series

	-19.878°	-15.9024°	-11.9268°
Series	-0.0160284-0.00144962j	-0.0101795-0.00554665j	-0.00412213-0.00670557j
Residue series without the Debye approximation	-0.0114841-0.00451637j	-0.00889355-0.00495257j	-0.00408404-0.00634298j
Percentage error in the magnitude of the residue series	23.32295055	12.18899495	4.156863631
	-7.9512°	-3.9756°	0°
Series	0.00092592-0.00600555j	0.00419331-0.00482518j	0.00531506-0.00428845j
Residue series without the Debye approximation	0.000851099-0.00594995j	0.00417271-0.00483559j	0.00531376-0.0043005j
Percentage error in the magnitude of the residue series	1.086069208	0.087851228	0.096092447

Table 64 The tabulation of the residue series results for $\beta = 40\pi$ and $n = -5$, the geometrical shadow region of the double negative cylinder corresponding to the second term of the Debye series

	-20.3118°	-16.2494°	-12.1871°
Series	-0.0122376-0.00617496j	0.00996644+0.00119667j	-0.0072511+0.00162238j
Residue series without the Debye approximation	-0.00721932-0.00697374j	0.00887523+0.000977986j	-0.00704582+0.00175181j
Percentage error in the magnitude of the residue series	26.77230188	11.04872798	2.288571998
	-8.12472°	-4.06236°	0°
Series	0.00498052-0.00298828j	-0.00353835+0.00353602j	0.0030496-0.00367276j
Residue series without the Debye approximation	0.00494934-0.00303079j	-0.00353575+0.00354752j	0.00305026-0.00367764j
Percentage error in the magnitude of the residue series	0.079684537	0.125939054	0.087494006

CHAPTER 6

CONCLUSION

Some of the properties of the double negative metamaterials have been investigated. These properties affect the propagation of electromagnetic waves through double negative metamaterials. Double negative metamaterials have negative refractive indices. They must have double negative refractive indices due to the condition of causality. The causality principle is not violated by the backward wave properties of double negative metamaterials. The backward wave property implies that the power propagation direction is opposite to the direction of the phase velocity. A plane wave is negatively refracted both at a planar interface and a cylindrical interface between a double positive medium and a double negative medium. The negative refraction at a planar interface has been proven theoretically. The negative refraction at a cylindrical interface has been proven both theoretically and numerically for the high frequency operation.

The physical mechanism for the high frequency plane wave scattering from an infinitely long cylinder has been presented using the Watson transform and the Debye expansion. The first term and the second term of the Debye series expansion have been investigated. The corresponding geometrical shadow regions and the geometrically lit regions have been determined. The physical insight into the field formation in these regions has been exhibited. These investigations have been made for both a double positive cylinder and a double negative cylinder. The differences between the double negative one and the double positive one have been indicated. The theoretical results have been numerically verified by the computations made using Mathematica. The series expressions corresponding to the first term and the second term of the Debye expansion have been computed. The obtained results have been compared to

the computation results for the integrals corresponding to the series expressions. The agreement between the two groups of results has been found to be good.

As a future work, the analysis of the high frequency scattering from the infinitely long cylinder (including transition regions) can be developed. A generalization to the computation of the terms of the Debye series expansion can be made. The physical insight into the scattering from the infinitely long cylinder can be used to take advantage of the properties of the double negative metamaterials in the possible scattering applications.

REFERENCES

- [1] V. G. Veselago, "The electrodynamics of substances with simultaneously negative values of ϵ and μ ", *Soviet Physics Uspekhi*, Volume 10, Number 4, January-February 1968.
- [2] J. B. Pendry, A. J. Holden, D. J. Robbins, W. J. Stewart, "Magnetism from conductors and enhanced nonlinear phenomena", *IEEE Transactions on Microwave Theory and Techniques*, Volume 47, Pages: 2075-2084, Nov. 1999.
- [3] J. B. Pendry, A. J. Holden, W. J. Stewart, I. Youngs, "Extremely low frequency plasmons in metallic mesostructures", *Physical Review Letters*, Volume 76, 4773, June 17 1996.
- [4] D. R. Smith, Willie J. Padilla, D. C. Vier, S. C. Nemat-Nasser, and S. Schultz, "Composite Medium with Simultaneously Negative Permeability and Permittivity", *Physical Review Letters*, Volume 84, 4184, May 1 2000.
- [5] J. B. Pendry, "Negative refraction makes a perfect lens", *Physical Review Letters*, Volume 85, Number 18, October 2000.
- [6] R. A. Shelby, D. R. Smith, S. Schultz, "Experimental Verification of a Negative Index of Refraction", *Science*, Vol. 292, 6 April 2001.
- [7] N. Garcia, M. Nieto-Vesperinas, "Is there an experimental verification of a negative index of refraction yet?", *Optics Letters*, Vol. 27, No. 11, June 1 2002.
- [8] P. M. Valanju, R. M. Walser and A. P. Valanju, "Wave refraction in negative-index media: Always positive and very inhomogeneous", *Physical Review Letters*, Volume 88, 187401, May 2002.
- [9] N. Garcia and M. Nieto-Vesperinas, "Left-handed materials do not make a perfect lens", *Physical Review Letters*, Volume 88, 207403, May 2002.
- [10] R. W. Ziolkowski and E. Heyman, "Wave propagation in media having negative permittivity and permeability", *Physical Review E*, Volume 64, No 056625 (2001).
- [11] R. W. Ziolkowski and A. D. Kipple, "Causality and double-negative metamaterials", *Physical Review E*, Volume 68, 026615 Part 2 (2003).

- [12] C. Caloz, H. Okabe, T. Iwai, and T. Itoh, "Transmission line approach of left-handed (LH) materials," in *Proc. USNC/URSI National Radio Science Meeting*, San Antonio, TX, June 2002, vol. 1, p. 39.
- [13] A. Grbic and G. V. Eleftheriades, "A backward-wave antenna based on negative refractive index," in *Proc. IEEE AP-S Int. Symp.*, vol. 4, San Antonio, TX, June 2002, pp. 340–343.
- [14] A. K. Iyer and G. V. Eleftheriades, "Negative refractive index metamaterials supporting 2-D waves," in *Proc. IEEE MTT-S Int. Symp.*, vol. 2, San Antonio, TX, June 2002, pp. 1067–1070.
- [15] George V. Eleftheriades, Ashwin K. Iyer, Peter C. Kramer, "Planar Negative Refractive Index Media Using Periodically L-C Loaded Transmission Lines", *IEEE Transactions on Microwave Theory and Techniques*, Vol. 50, No. 12, December 2002.
- [16] R. A. Shelby, D. R. Smith, S. C. Nemat-Nasser, S. Schultz, "Microwave transmission through a two-dimensional, isotropic, left-handed metamaterial", *Applied Physics Letters* 78, pp. 489-491, 2001.
- [17] J. Pacheco Jr., T. M. Grzegorzczuk, B.-I. Wu, Y. Zhang, J. A. Kong, "Power propagation in homogeneous isotropic frequency-dispersive left-handed media", *Physical Review Letters*, Volume 89, 257401.
- [18] C. Caloz, C. Chang, T. Itoh, "Full-wave verification of the fundamental properties of left-handed materials in waveguide configurations", *Journal of Applied Physics*, 90, pp. 5483-5486, 2001.
- [19] R. Ruppin, "Extinction properties of a sphere with negative permittivity and permeability", *Solid State Communications*, 116, 411-415, 2000.
- [20] Vladimir Kuzmiak, Alexei A. Maradudin, "Scattering properties of a cylinder fabricated from a left-handed material", *Physical Review B*, 66, 045116, 2002.
- [21] R. Ruppin, "Intensity distribution inside scatterers with negative-real permittivity and permeability", *Microwave and Optical Technology Letters*, Vol. 36, No. 3, February 5 2003.
- [22] Richard W. Ziolkowski, Allison D. Kipple, "Application of Double Negative Materials to Increase the Power Radiated by Electrically Small Antennas", *IEEE Transactions on Antennas and Propagation*, Vol. 51, No. 10, October 2003.

- [23] Sanshui Xiao, Linfang Shen, Sailing He, "A Novel Directional Coupler Utilizing a Left-Handed Material", *IEEE Photonics Technology Letters*, Vol. 16, No. 1, January 2004.
- [24] P. Debye, *Physik. Z.*, 9, 775 (1908).
- [25] H. Inada, "Diffracted field computations by a series expansion", *Radio Science*, vol. 10, Feb. 1975, p. 205-220.
- [26] T. Sasamori, T. Uno, S. Adachi, "High-frequency Analysis of Electromagnetic Scattering due to a Dielectric Cylinder", *Electronics and Communications in Japan Part II-Electronics*, 78, 4, 41-55, 1995.
- [27] H. M. Nussenzweig, "High-Frequency Scattering by an Impenetrable Sphere," *Annals of Physics*, 34, 23-95 (1965).
- [28] H. M. Nussenzweig, "High-Frequency Scattering by a Transparent Sphere.1. Direct Reflection and Transmission," *Journal of Mathematical Physics*, Volume 10, Number 1, 82-124, January 1969.
- [29] Milton Abramowitz and Irene A. Stegun, *Handbook of Mathematical Functions with Formulas, Graphs, and Mathematical Tables*, Dover Publications Inc., New York, 1972.
- [30] Martin W. McCall, Akhlesh Lakhtakia, Werner S. Weiglhofer, "The negative index of refraction demystified", *Eur. J. Phys.*, 23 (2002), 353-359.

CURRICULUM VITAE

PERSONAL INFORMATION

Surname, Name: Şen, Saffet Gökçen
Nationality: Turkish (TC)
Date and Place of Birth: 7 May 1976, Erzurum
Marital Status: Married
Phone: +90 505 6758716
email: saffetgokcensen@hotmail.com

EDUCATION

Degree	Institution	Year of Graduation
MS	METU Electrical Engineering	2002
BS	Bilkent Electrical Engineering	1998
High School	Erzurum Anadolu High School	1994

WORK EXPERIENCE

Year	Place	Enrollment
2002-Present	METU Electrical Engineering	Teaching Assistant
1999-2000	Bilkent Uni. CEM Center	Project Engineer
1998-1999	Aselsan	Engineer

FOREIGN LANGUAGES

Advanced English

HOBBIES

Reading, playing chess, swimming